TECHNISCHE UNIVERSITÄT MÜNCHEN
Physik-Department E62 – Dense and Strange Hadronic Matter
Excellence Cluster – Origin of the Universe

Performance studies with a full-size GEM-based prototype for the ALICE TPC

— MASTER THESIS —

Andreas Michael Mathis

January 25, 2016

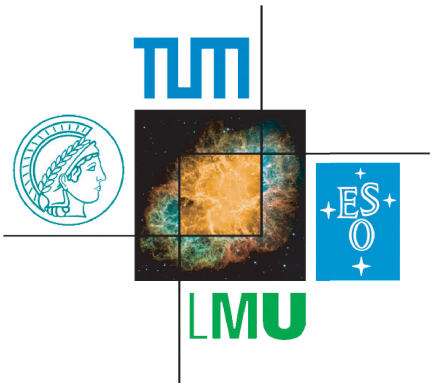

Abstract

The second generation of heavy-ions studies at the Large Hadron Collider beyond 2020 will be enabled by a significant increase of the collider's luminosity. In order to be able to run at an increased interaction rate of 50 kHz in Pb–Pb, the ALICE Collaboration is planning major upgrades of the spectrometer. In particular, the ALICE Time Projection Chamber (TPC), the main device for charged-particle tracking and particle identification (PID) in ALICE, is foreseen to be operated in an ungated mode with continuous readout. Therefore, the currently used gated Multi-Wire Proportional Chambers (MWPC) will be replaced by readout chambers based on the Gas Electron Multiplier (GEM), while retaining the present tracking and PID capabilities via measurement of the specific energy loss $\mathrm{d}E/\mathrm{d}x$.

In the course of this work, large-size prototypes for both the Inner and Outer Readout Chamber (IROC/OROC) have been built employing the configuration foreseen for the ALICE TPC upgrade: a stack of four GEM foils containing both Standard (S, 140 µm pitch) and Large Pitch (LP, 280 µm pitch) GEMs arranged in the order S-LP-LP-S.

In order to prove, that the excellent PID capabilities of the ALICE TPC are retained after the upgrade, the ALICE IROC prototype has been exposed to a beam of electrons and pions delivered by the CERN Proton Synchrotron. An extensive study of different high voltage configurations, characterized by the respective performance in terms of ion backflow and energy resolution at the ^{55}Fe peak, has been carried out. The corresponding $\mathrm{d}E/\mathrm{d}x$ resolution has been investigated using AliRoot, the framework for simulation, reconstruction and analysis in ALICE. The typical track geometry and the replacement of the MWPCs with GEM-based readout chambers imposed the necessity to adopt the track reconstruction scheme. Moreover, a parametrization of the uncertainty on the position measurement of ionization clusters taking into account track parameters has been extracted and applied. The charge contained in such clusters is corrected for local variations of the electron multiplication in the GEM-stack and angular effects introduced by the discrete, rectangular shape of the readout pads.

The presented analysis is complemented by comprehensive full-scale simulations of the detector response aiming at obtaining a prediction of the measured $\mathrm{d}E/\mathrm{d}x$ results. In order to reproduce the performance of different high voltage settings applied to the GEM stack, the electron efficiency of the readout system has been reduced, resulting in a degradation of the $\mathrm{d}E/\mathrm{d}x$ resolution. Dedicated simulations of a ^{55}Fe source have quantified the detector response to this degradation and allow for a comparison to measured data.

Finally, the $\mathrm{d}E/\mathrm{d}x$ resolution has been determined and is found to fully comply with the requirements of the ALICE upgrade physics programme.

Zusammenfassung
Eine signifikante Steigerung der Beschleunigerluminosität ermöglicht ab 2020 die zweite Generation von Schwerionenexperimenten am Large Hadron Collider. Um den Betrieb bei einer erhöhten Interaktionsrate von 50 kHz in Pb–Pb zu erlauben, plant die ALICE Kollaboration wesentliche Upgrades des Spektrometers. Insbesondere soll die ALICE *Time Projection Chamber* (TPC), der wichtigste Detektor zur Spurrekonstruktion geladener Teilchen und Teilchenidentifikation in ALICE, mit einer kontinuierlicher Auslese betrieben werden. Daher werden die aktuell benutzten sequentiell betriebenen *Multi-Wire Proportional Chambers* (MWPC) durch auf *Gas Electron Multiplier* (GEM) basierenden Auslesekammern ersetzt, wobei das derzeitige Spurrekonstruktions- und Teilchenidentifikationsvermögen durch Messung des spezifischen Energieverlustes $\mathrm{d}E/\mathrm{d}x$ erhalten bleiben soll.

Im Zuge der vorliegenden Arbeit wurden große Prototypen sowohl einer Inneren als auch einer Äußeren Auslesekammer (IROC/OROC) entwickelt und gebaut, unter Verwendung der für das ALICE TPC Upgrade vorgesehenen Konfiguration: eine Anordnung von vier GEM-Folien, die sowohl Standard-GEMs (S, 140 µm Lochabstand) als auch Large Pitch-GEMs (LP, 280 µm Lochabstand) in der Reihenfolge S-LP-LP-S enthält.

Um zu demonstrieren, dass das exzellente Teilchenidentifikationsvermögen der ALICE TPC nach dem Upgrade erhalten bleibt, wurde der ALICE IROC Prototyp einem vom CERN Proton Synchrotron stammenden Strahl von Elektronen und Pionen ausgesetzt. Eine umfangreiche Untersuchung verschiedener Hochspannungskonfigurationen wurde durchgeführt, die durch das jeweilge Verhalten in Bezug auf den Ionen-Rückfluss und die Energieauflösung am ^{55}Fe-Peak charakterisiert sind. Die entsprechende $\mathrm{d}E/\mathrm{d}x$-Auflösung wurde mit AliRoot, dem Framework zur Simulation, Rekonstruktion und Analyse in ALICE, eruiert. Die typische Geometrie der Teilchenspuren und der Austausch der MWPCs durch GEM-basierte Auslesekammern erforderten eine Anpassung des Rekonstruktionsverfahrens der Teilchenspuren. Darüber hinaus wurde eine Parametrisierung der Ortsunsicherheit von Ionisations-Clustern unter Berücksichtigung von Eigenschaften der Teilchenspur extrahiert und angewandt. Die Ladung, die in einem solchen Cluster enthalten ist, wurde auf lokale Variationen der Elektronenverstärkung in den GEM-Folien und Winkelabhängigkeiten, die von der diskreten, rechteckigen Form der Auslesepads herrühren, korrigiert.

Die vorgestellte Analyse wird ergänzt durch umfassende Simulationen des Ansprechverhaltens des Detektors mit dem Ziel, eine Prognose der gemessenen $\mathrm{d}E/\mathrm{d}x$-Resultate zu erhalten. Um das Verhalten bei verschiedenen Hochspannungskonfigurationen der GEM-Anordnung zu reproduzieren, wurde die Elektroneneffizienz des Auslesesystems reduziert, was zu einer Verschlechterung der $\mathrm{d}E/\mathrm{d}x$-Auflösung führte. Durch dedizierte Simulationen einer ^{55}Fe-Quelle wurde das Ansprechverhalten des Detektors auf diese Verminderung quantifiziert, um so einen Vergleich mit den Messdaten zu erhalten.

Die abschließende Bestimmung der $\mathrm{d}E/\mathrm{d}x$-Auflösung hat ergeben, dass die Anforderungen des ALICE Upgrade Physikprogrammes vollständig erfüllt werden.

Contents

1 Introduction

In the framework of the Standard Model of particle physics, the quantum field theory describing the strong interaction is *Quantum ChromoDynamics* (QCD), based on quarks and gluons as fundamental degrees of freedom. While the strongly interacting particles, hadrons, are composed out of six different quark flavours, the gluons are the corresponding gauge bosons. The colour is introduced as an additional quantum number and can take three values (red, green or blue) and the corresponding negative values. In contrast to quantum electrodynamics (QED), the quantum theory of the weak and electromagnetic force, not only quarks but also gluons carry colour charge. Therefore, the gluons can interact with one another. The strength of the interaction between two quarks is given by the running coupling constant of the strong force α_s,

$$\alpha_s(Q^2) = \frac{12\pi}{(33 - 2N_f)\ln(Q^2/\Lambda^2_{\mathrm{QCD}})};\ Q^2 \gg \Lambda^2_{\mathrm{QCD}}, \tag{1.1}$$

where N_f represents the number of quark flavours and $\Lambda^2_{\mathrm{QCD}} \approx 200\,\mathrm{MeV}$ the fundamental QCD scale parameter. The energy dependence of α_s can be observed in Fig. 1.1, where results obtained at discrete energy scales Q are shown. In the low-energy limit, the strength of the coupling increases and therefore, when pulling two quarks apart from each other, it may become energetically more favourable to produce new quark-antiquark pairs. Consequently, free quarks cannot exist and have indeed never been observed, which is why this effect is referred to as *colour confinement*, as the quarks are always confined in composite, colour-neutral objects. These objects exist either in the form of mesons ($q\bar{q}$) or hadrons (qqq or $\bar{q}\bar{q}\bar{q}$).

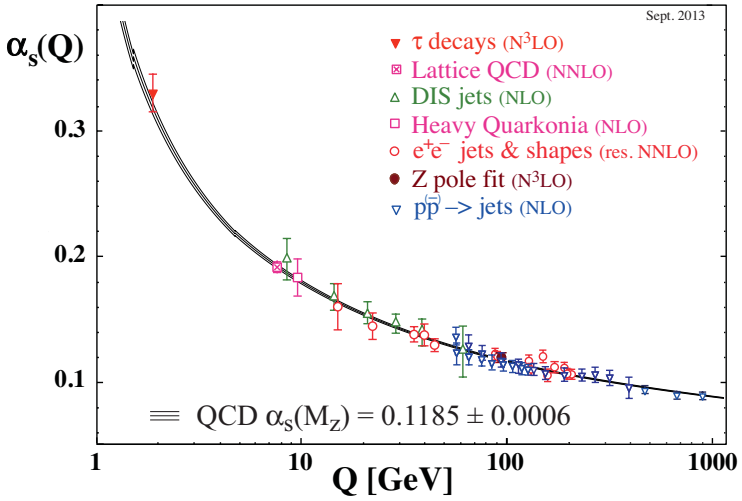

Figure 1.1: Summary of measurements of α_s as a function of the energy scale Q [1]. The respective degree of QCD perturbation theory used is indicated in brackets.

On the other hand, the coupling constant decreases with high energies and therefore, the quarks may behave like free particles (*asymptotic freedom*). Consequently, at very high temperatures and densities, a transition from ordinary nuclear matter to a de-confined phase of quarks and gluons - the so-called *Quark-Gluon Plasma* (QGP) - may be expected. The critical temperature for this phase transition can be inferred from lattice calculations and is assumed to be $\sim$155 MeV [2]. For a detailed review of the phase transition and its consequences, refer to e.g. [3].

The conditions necessary for the phase transition are thought to be found at ultra-relativistic heavy-ion colliders, where the matter is expected to be heated and brought to temperatures and densities sufficient for the creation of a QGP and thus allowing for studies of its properties.

1.1 ALICE – A Large Ion Collider Experiment

ALICE [4] is a heavy-ion experiment dedicated to the study of the physics of the high-density, high-temperature phase of strongly interacting matter and located at the CERN Large Hadron Collider (LHC), which delivers beams of protons or lead ions at unprecedented energies. In order to obtain a solid understanding of the underlying collision dynamics, the Pb–Pb studies are complemented by proton-proton (pp) and proton-lead (pPb) collision experiments.

The overall dimensions of the apparatus are $16 \times 16 \times 26$ m^3 at a weight of more than 10.000 t. The detector system was designed to cope with particle multiplicities of up to $\mathrm{d}N_{\mathrm{ch}}/\mathrm{d}\eta \approx 8000$, which were expected for Pb–Pb collisions at top LHC energy at the time of its construction. Figure 1.2 shows a schematic view of the spectrometer.

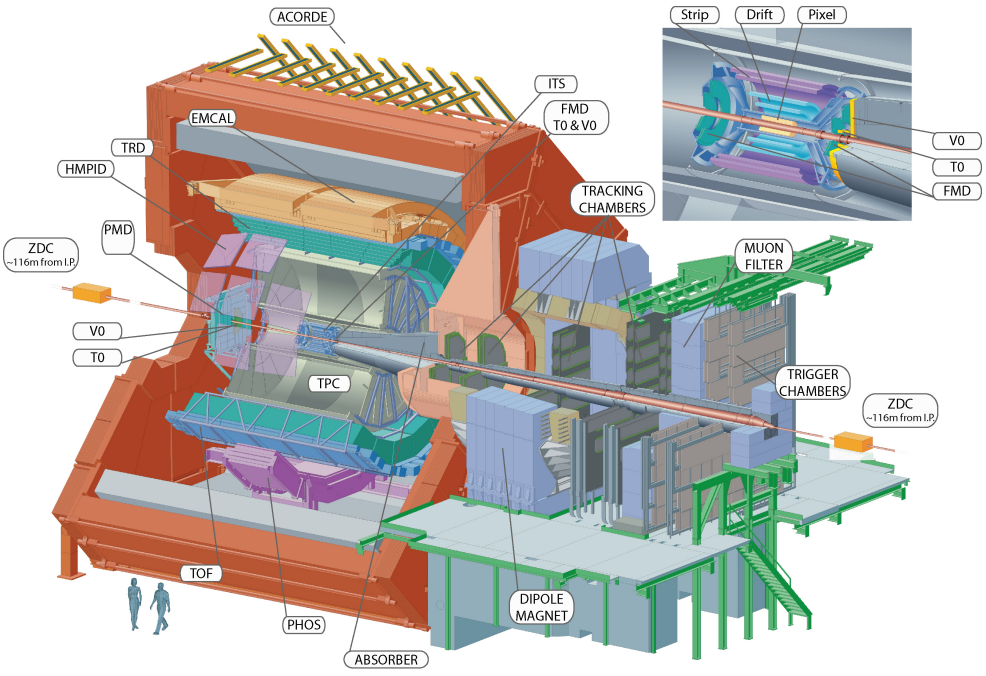

Figure 1.2: Schematic view of the ALICE experiment [5]. The insert shows the detectors close to the interaction point.

The sub-detectors in the central barrel, dedicated to the measurement of hadrons, electrons, and photons, are enclosed in the L3 magnet, a large solenoid magnet inherited from the LEP L3 experiment [6], which delivers a magnetic field of up to 0.5 T. The central barrel detectors (ITS, TPC, TRD and TOF) cover a pseudo rapidity range of $|\eta| < 0.9$ over the full azimuthal angle, while the three single-arm detectors (HMPID, EMCal and PHOS) provide a smaller azimuthal and polar acceptance. The ALICE forward detectors (PMD, FMD, V0, T0, and ZDC) are used for global event characterization and triggering. The muon spectrometer, with a hadron absorber of $\sim 10 \cdot \lambda_{\mathrm{int}}$ and a dipole magnet of 3 T m, is dedicated to the measurement of quarkonium and light vector meson production, as well as of high p_{T} muons stemming from the decay of charm and beauty in the region of $-4.0 < \eta < -2.5$.

The necessity for excellent particle identification (PID) arises from the physics programme of ALICE, as the measurement of many observables of the QGP strongly depends on the PID capabilities of the apparatus. The most natural example is the measurement of particle abundances, from which freeze-out parameters, such as the kinetic and chemical freeze-out temperature and the collective flow velocity, can be inferred [7]. Another example is the measurement of light vector mesons, as any modification of their mass and width is interpreted as a signature for partial chiral symmetry restoration [8]. As for example the ϕ resonance can be identified either by its hadronic ($\phi \rightarrow \mathrm{K}^{+}\mathrm{K}^{-}$) or its leptonic decay channel, a good hadron or lepton ID is obviously mandatory for such studies.

In general, PID is based on simultaneously measuring the charge ze and mass m of the particle. The charge sign can be inferred from the curvature of the particle's track in the magnetic field, while the mass has to be deduced from other variables by exploiting

$$m = \frac{p}{\beta\gamma c}, \tag{1.2}$$

where p is the momentum of the particle, β its velocity, c the speed of light and γ the relativistic Lorentz factor $\gamma = (1 - \beta^2)^{-1/2}$. Therefore, by measuring the momentum p and the velocity β of the particle, the mass of the particle can be inferred. The momentum of the particle is commonly obtained by measuring the bending radius of the particle's track in a magnetic field, while the velocity can be obtained by

1. measurement of the specific energy loss $\mathrm{d}E/\mathrm{d}x$,
2. measurements of the Time-Of-Flight (TOF) over a certain path length L,
3. detection of Cherenkov radiation emitted when $\beta\gamma > 1/n$, where n represents the refractive index of the medium, or
4. detection of transition radiation produced, when a relativistic charged particle traverses the interfaces of two media with different dielectric constants.

Each of these methods, however, is restricted to certain momentum ranges. While PID via the measurement of the specific energy loss will be discussed in Sec. 2.3, the other methods are treated thoroughly elsewhere, see e.g. [7].

1.1.1 Detectors for particle identification

By combining the PID information of different detector system, ALICE is able to identify particles with momenta ranging from about 0.1 GeV/c up to a few GeV/c [9]. The PID efficiency is mainly limited by particle decays and absorption in detector material. Integrated over momentum, it is about 50 % for pions and protons and about 40 % for kaons. Electrons with momenta above 1 GeV/c are identified by the TRD with an efficiency above 90 % [5]. In the following, the most important detectors for PID in the ALICE experiment are introduced.

Inner Tracking System (ITS)
The main task of the Inner Tracking System [10] is to localize the primary interaction vertex and to reconstruct secondary vertices of the decay of hyperons, D and B mesons. Furthermore, it provides tracking of low momentum particles that do not reach the acceptance of the TPC. It consists of six cylindrical layers of silicon detectors, located at radii between 4 and 43 cm around the interaction point. Due to considerations of the expected particle densities, the two innermost layers are instrumented with Silicon Pixel Detectors (SPD), the two middle layers with Silicon Drift Detectors (SDD) and the two outer layers with double-sided Silicon micro-Strip Detectors (SSD). The outer four layers can provide PID via a $\mathrm{d}E/\mathrm{d}x$ measurement in the non-relativistic ($1/\beta^2$) region. For a discussion of the $\mathrm{d}E/\mathrm{d}x$ measurement refer to Sec. 2.3.

In Pb–Pb, the precision of the determination of the primary vertex is about 5 µm, while the resolution in pp is degraded by about one order of magnitude due to the reduced number of tracks.

Time Projection Chamber (TPC)
The Time Projection Chamber [11] is the main device for charged-particle tracking and momentum measurement in the central barrel of the ALICE experiment. It provides PID via the measurement of the specific energy loss with a resolution of about 5.2 % in pp collisions and 6.5 % in the 0–5 % most central Pb–Pb collisions [5].

A detailed description of the TPC is given in Sec. 2.4.

Transition Radiation Detector (TRD)
The main task of the Transition Radiation Detector [12] is to provide electron identification in the central barrel, which is based on the measurement of the specific energy loss and transition radiation for particle momenta above 1 GeV/c. For these momenta, the pion rejection capabilities of the TPC are no longer sufficient. Moreover, it can also be used to trigger on electrons with high transverse momenta or jets. The TRD consists of six alternating layers of radiator and drift chamber respectively.

Time-Of-Flight Detector (TOF)
The Time-Of-Flight detector [13] consists of a large array of Multigap Resistive Plate Chambers (MRPC) and provides PID in the intermediate momentum range. The overall TOF resolution is 80 ps for pions with a momentum around 1 GeV/c in Pb–Pb collisions in the centrality range 0-70 %.

1.1.2 AliRoot

In order to process the data recorded by the detectors, a dedicated software framework, AliRoot [14], was developed. The role of a framework in high-energy physics is to handle the raw data, either measured by the detector or generated via simulation algorithms, and to run detector calibration, track reconstruction and physics analyses. The overall design of the AliRoot framework is based on *modularity* and *re-usability*, as a such designed system allows for the replacement or modification of single parts of the code without affecting the functionality of the overall framework. This is in particular important when it comes to upgrades of modifications of individual sub-detector systems.

A schematic overview of the AliRoot framework is given in Fig. 1.3, with the main modules AliEn, for distributed grid computing, and the ROOT framework [16] as base for e.g. handling data I/O. The central module of AliRoot is *STEER* as it provides run management, the base classes and interfaces to the detector, simulator and event generator modules.

Thus, the individual detector modules are independent of one another and can hence be added to or removed from the data processing. This is in particular important, as the data of all detectors is not always available. Moreover, the modular design allows for conducting studies with only one sub-detector as for example presented in this work.

The introduction of a Virtual Monte Carlo interface [17] allows for performing detector simulations with different transport codes like GEANT3 [18], GEANT4 [19] and FLUKA [20] without the necessity to change the user code. The same holds for the different event generators, accessed via the virtual interface EVGEN (AliGenerator).

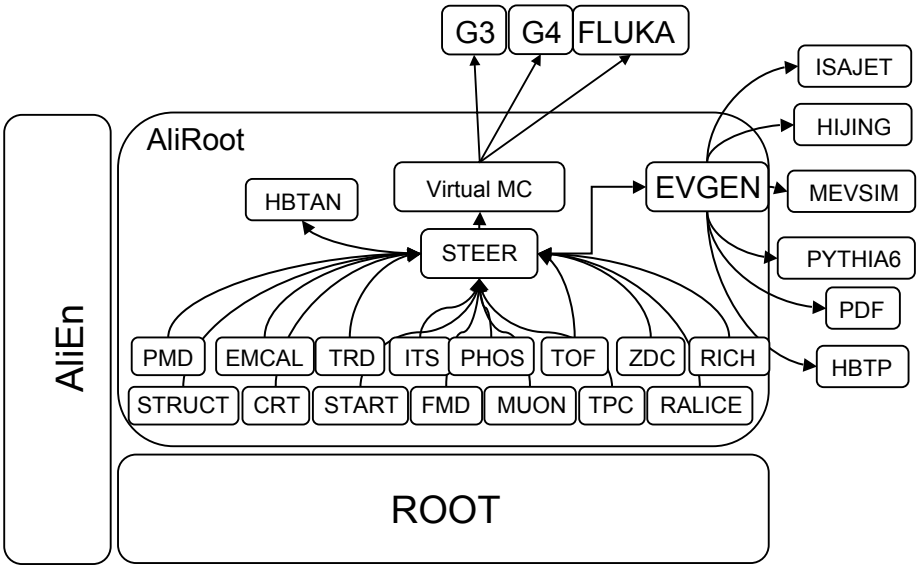

Figure 1.3: Schematic view of the AliRoot framework [15].

1.1.3 Coordinate systems

Global coordinate system

The global coordinate system of ALICE [21] is a right-handed cartesian system with the interaction point as its origin. The x-axis is pointing towards the centre of the LHC ring, while the y-axis is oriented upwards. The z-axis is coinciding with the beam direction and pointing towards the A-side (away from the muon arm).

The azimuthal angle ϕ increases counterclockwise, starting from the x-axis (ϕ=0°). The polar angle θ is increasing from the z-axis towards the xy-plane. A sketch of the ALICE detector with the global coordinate system is shown in Fig. 1.4a.

Local coordinate system in the ALICE TPC

As all central barrel detectors are segmented azimuthally, the reconstruction software makes use of a common convention regarding the local coordinate system [9] for a given sub-unit, e.g. a TPC sector. The local coordinate system is, as the global, a right-handed cartesian system. Both share the same origin and z-axis. The transformation between both coordinate systems is given by a rotation of the angle α around the z-axis. Therefore, the local x-axis is perpendicular to the sub-unit's *sensitive plane*, e.g. a pad row of the TPC, while the y-axis is parallel to it (compare Fig. 1.4b).

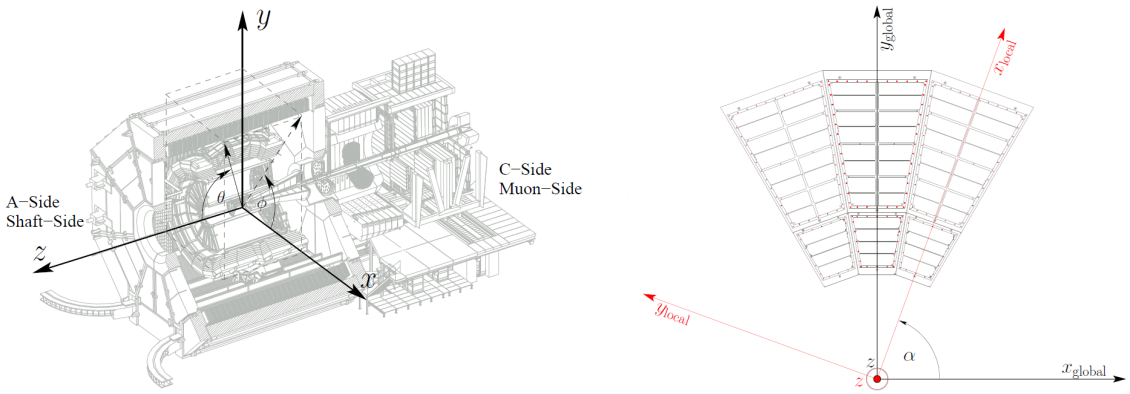

(a) **(b)**

Figure 1.4: Global (a) and local (b) coordinate system of the ALICE detector [22].

1.2 The ALICE upgrade for RUN3

The second generation of LHC heavy-ion studies beyond 2020 (after the so-called Long Shutdown 2) will be enabled by a significant increase of the LHC instant luminosity to $6 \times 10^{27}\,\mathrm{cm}^{-2}\mathrm{s}^{-1}$, thus allowing for the study of rare probes and their coupling to the medium [23]. In particular, the main physics topics addressed by ALICE in RUN3 will be measurements of heavy flavour hadrons, quarkonia, and low-mass dileptons at low p_{T}, which demands for large statistics.

These measurements will be possible by reading out all Pb–Pb events at an interaction rate of 50 kHz, which demands for a modification of the readout electronics of several sub-detectors, as well as of the online and offline systems. Moreover, the vertex determination and tracking capabilities of the apparatus will need to be enhanced. For the Inner Tracking System, this implies a replacement with a completely re-designed and newly built apparatus.

As the drift time of electrons in the TPC is on average longer than the typical event spacing at an interaction rate of 50 kHz, the current triggered operation will no longer be possible, as it would cause unacceptable losses of data. Hence, a continuous operation of the TPC is mandatory, which demands for a complete re-design of the readout chambers.

The main components of the TPC, including the field cage, the endplates and the gas system will be reused. An overview of the current TPC design can be found in Chap. 2. The newly built readout chambers will be based on GEM technology [24], a choice mainly motivated by the intrinsic ion blocking and high-rate capabilities of GEMs. The proposed solution, a stack of four GEMs, has been verified in a thorough R&D program. The outcome of these studies is briefly summarized in Chap. 3, where also the main features of the design of the GEM foils for the upgrade are introduced.

As the TPC is the main device for charged-particle tracking and for particle identification in ALICE, it is of particular importance to retain the present, excellent PID capabilities via measurement of the specific energy loss after the upgrade. The goal of the presented study of the $\mathrm{d}E/\mathrm{d}x$ resolution of a prototype chamber is to provide proof of this. To this end, a full-size prototype chamber has been built and exposed to a beam of pions and electrons at the CERN PS. The detector prototype is described in Chap. 4, while the setup and the data analysis chain are introduced in Chap. 5. In order to obtain a deeper understanding of the effect of a GEM-based amplification structure on the $\mathrm{d}E/\mathrm{d}x$ performance, detailed, microscopic simulations have been performed, which are described in Chap. 6. The results obtained with data from the testbeam and the microscopic simulation are compared and discussed in Chap. 7.

1.3 Summary of the prototype studies for the ALICE TPC upgrade

In the context of the R&D phase for the upgrade of the ALICE TPC, measurements with both small and full-size prototypes have been conducted in order to prove the feasibility of the upgrade. Moreover, the demanding requirements in terms of energy resolution at the ^{55}Fe peak, ion backflow (*IB*) and stability against electrical discharges impose the necessity to carefully optimize the high voltage (HV) configuration of the GEMs. A detailed overview of the results obtained in the course of these studies can be found in [24, 25].

A prototype of the ALICE Inner Readout Chamber (IROC) has been assembled at the Technische Universität München and equipped with a stack of three GEMs in order to prove the feasibility of GEM integration on large-size readout chambers and that the $\mathrm{d}E/\mathrm{d}x$ resolution of the ALICE TPC is retained after the upgrade [24]. In addition, the operational stability of the prototype has been studied under realistic running conditions at the LHC and with low-energy protons at the Maier-Leibnitz-Laboratorium in Garching.

In parallel to these activities, extensive scans of different HV configurations have been conducted with small detectors employing $10\times10\,\mathrm{cm}^2$ GEM foils with different hole pitches. In particular, triple and quadruple stacks assembled with various combinations of Standard (S, 140 µm pitch), Small Pitch (SP, 70 µm) and Large Pitch (LP, 280 µm) GEMs have been investigated. The performance of a standard triple GEM-stack has been found to be insufficient both in terms of the achieved *IB* performance and operational stability. However, a suitable working point fulfilling all requirements has been found with a stack of four GEM foils arranged in the order S-LP-LP-S under a specific voltage configuration [24].

In order to further quantify the performance of readout chambers equipped with such a stack, large-size prototypes have been built and assembled. In particular, the operational stability and the performance in terms of the $\mathrm{d}E/\mathrm{d}x$ resolution has been studied with a prototype of the ALICE IROC [25]. Moreover, a first prototype of the ALICE Outer Readout Chamber (OROC) has been assembled in order to provide proof of the feasibility of GEM integration on readout chambers of so far unprecedented size and the define the relevant assembly steps and quality criteria. A detailed description of both full-size prototypes will be given in Chap. 4.

2 The ALICE Time Projection Chamber

The Time Projection Chamber (TPC) [26] has proven to be an almost ideal tracking detector, especially when it comes to instrument large volumes at a low material budget, as it allows for a three-dimensional reconstruction of the trajectories of charged particles. In this chapter, the concept of the TPC will be introduced and the relevant physics processes for signal creation will be discussed. Furthermore, an overview of the ALICE TPC will be given, which is currently the largest detector of its kind in the world.

2.1 Working principle of a TPC

In general, a TPC is a gas-filled, cylindrically-shaped vessel with two electrodes on its sides, as depicted schematically in Fig. 2.1. A charged particle traversing the volume ionizes the gas and hence leaves a trail of electron-ion pairs along its path. By applying an electric field between the two electrodes, the so-called *drift field*, these pairs are separated and the charge carriers drift towards the respective electrode. As the drift velocity of electrons is enhanced by almost three orders of magnitude compared to ions, the electrons are the charge carriers of interest.

As the signal induced on the segmented anode (*pad plane*) by the ionization electrons would be imperceivable for modern readout electronics, a multiplication of the electrons is mandatory. This has been commonly achieved by employing *Multi-Wire Proportional Chambers* (MWPC) [28], yet due to intrinsic shortcomings of this technology, readout chambers based on *Micro Pattern Gas Detectors* (MPGD), as discussed in Chap. 3, are considered as a replacement.

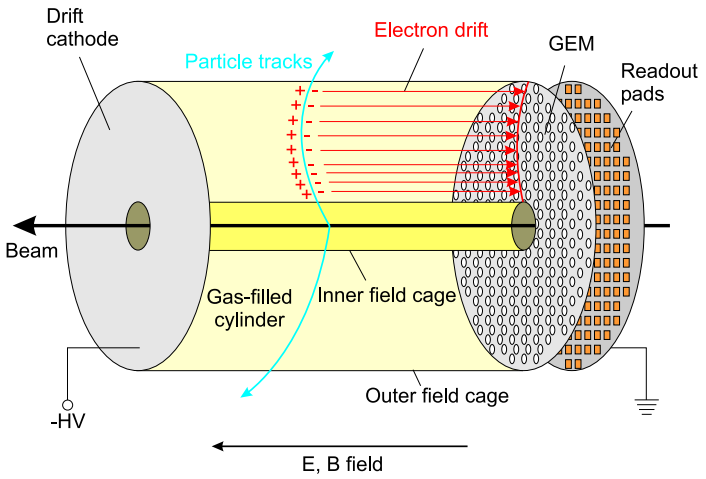

Figure 2.1: Schematic view of a GEM-based TPC [27].

The measurement of the impact position of the ionization electrons on the pad plane yields a measurement of the spatial coordinates of the projection of the trajectory onto this plane. As the drift time can be considered as a constant on a macroscopic scale, with proper knowledge of time of the initial interaction, the z-components of the trajectory can be measured. Consequently, the three-dimensional spatial information about the path of the particle is obtained. By enclosing the TPC in a magnetic bending field, the particle's momentum can be inferred as well. Furthermore, by measuring the specific energy loss along the trajectory, a TPC can also provide PID.

2.2 Physics processes in a TPC

2.2.1 Gas ionization and energy loss of charged particles

While passing through a gaseous medium, a charged particle is subject to random collisions with the gas atoms. The mean distance between two such interactions is characterized by the *mean free path* λ,

$$\lambda = \frac{1}{n_e \sigma}, \tag{2.1}$$

where n_e is the electron density of the traversed medium and σ the total collision cross section. The number of of ionizing collisions n_{coll} over the length x follows a Poisson distribution, which reflects the random nature of the process,

$$P(x/\lambda, n_{\mathrm{coll}}) = \frac{(x/\lambda)^{n_{\mathrm{coll}}}}{n_{\mathrm{coll}}!} \cdot e^{-x/\lambda}. \tag{2.2}$$

Such collision may, in case the energy transfer is sufficient, result in an ionization of the corresponding atom or molecule and the liberation of *primary* electrons. Further ionization of the gas by the primary electrons results in *secondary* electrons, which may stem either from ionizing collisions with the gas atoms or via intermediate excited states. The mean number of electron-ion pairs created along the trajectory of a charged particle with length x is then due to both primary and secondary ionization and given by

$$\langle n_{\mathrm{tot}} \rangle = \frac{x \cdot \langle \mathrm{d}E/\mathrm{d}x \rangle}{W_i}, \tag{2.3}$$

where $\langle \mathrm{d}E/\mathrm{d}x \rangle$ is the average energy loss per unit path length of the fast particle. Only a fraction of the total energy deposit of the charged particle is used to ionize the gas, as there are many competing mechanisms for energy loss. Therefore, the quantity W_i is introduced, the *effective ionization potential*, which is defined as the mean energy necessary for the liberation of one electron and hence accordingly larger than the first ionization potential.

2.2.1.1 Mean energy loss

The mean energy loss per unit path length of a charged particle is then typically given by the Bethe-Bloch formula [29],

$$\left\langle -\frac{\mathrm{d}E}{\mathrm{d}x} \right\rangle = \frac{4\pi n_e e^4}{m_e c^2} \frac{1}{\beta^2} z^2 \left(\ln \frac{2m_e c^2}{I} \beta^2 \gamma^2 - \beta^2 - \frac{\delta(\beta)}{2} \right), \tag{2.4}$$

where $m_e c^2$ is the rest energy of the electron, z the charge of the incident particle, e the elementary charge and I the mean excitation energy of the atom. Notable is, that the mean energy loss depends only on the velocity β of the incident particle, and not on its mass.

With increasing $\beta\gamma$, $\langle \mathrm{d}E/\mathrm{d}x \rangle$ follows at first $1/\beta^2$, then passes through a minimum at $\beta\gamma \sim 3-4$ and rises again with $\ln \beta^2\gamma^2$. The strength of this *relativistic rise* for large $\beta\gamma$, hence the name, is defined by the mean excitation energy I. The relativistic deformation of the electromagnetic field of the incident particle perpendicular to its passage causes screening effects due to the polarisation of the medium. These effects gain significant importance for higher $\beta\gamma$ and therefore partially compensate for the relativistic rise. Therefore, the correction term $\delta(\beta)$ is introduced to the equation, incorporating this *density effect*.

For higher projectile energies, radiative effects and higher order QED processes that are not incorporated in the Bethe-Bloch equation significant importance and correspondingly $\beta\gamma \gtrsim 1000$ represents an upper limit for the validity of the formula. On the other hand, for lower energies ($\beta\gamma \leq 0.1$), the assumption of stationary shell electrons incorporated in Eq. 2.4 is no longer valid. Moreover, at very low projectile energies, electron capture can occur and the stopping power of negatively charged particles is smaller compared to positively charged projectiles (*Barkas effect*) [30]. The overall behaviour of $\langle \mathrm{d}E/\mathrm{d}x \rangle$, also beyond the validity of the Bethe-Bloch formula, is shown in Fig. 2.2.

For practical purposes, the Bethe-Bloch formula can be approximated by a function initially proposed by the ALEPH collaboration [29],

$$f(\beta\gamma) = \frac{P_1}{\beta^{P_4}} \cdot \left\{ P_2 - \beta^{P_4} - \ln \left[P_3 + \frac{1}{(\beta\gamma)^{P_5}} \right] \right\}, \tag{2.5}$$

where P are parameters obtained from a fit to data, $P = \{0.0820, 9.948, 8.973 \times 10^{-5}, 2.059, 1.653\}$.

The Bethe-Bloch equation describes however only the *mean* energy loss of a particle, i.e. the statistical average over many collisions. By measuring the ionization electrons on a finely segmented readout anode, the incident particle undergoes only few interactions while passing through the segment of interest. Therefore, the total energy deposit is subject to fluctuations reflecting the random nature of the interaction, concerning both the varying distance between the individual collisions and the fluctuating, corresponding energy loss. While the distance between successive interactions follows Poissonian statistics, the energy deposit of the incident particle in single collisions is described by the differential collision cross section. It is therefore necessary to obtain a reliable calculation of the latter to describe the energy deposit in a gaseous detector. Several models are available and for detailed review, refer to e.g. [31]. In the following two models shall be motivated.

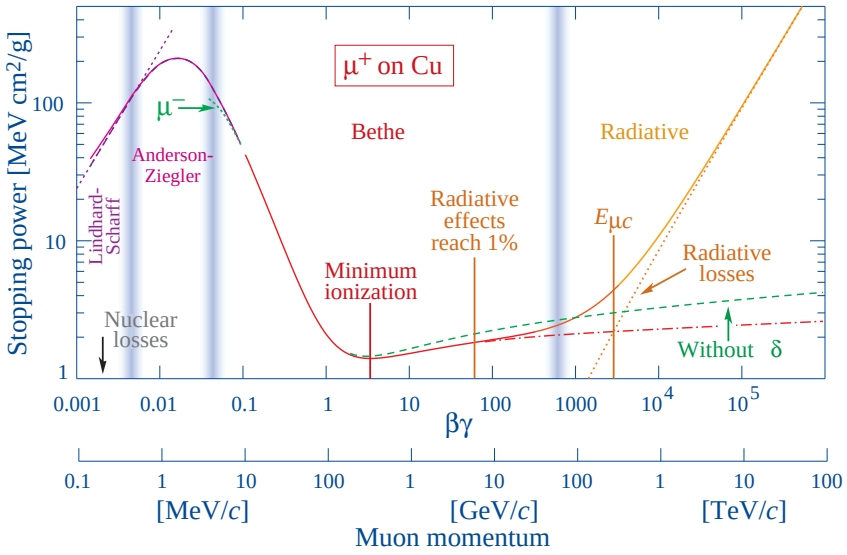

Figure 2.2: Stopping power $\langle -\mathrm{d}E/\mathrm{d}x \rangle$ for positive muons in copper as a function of $\beta\gamma$ over nine orders of magnitude in momentum [1]. Solid curves indicate the total stopping power, while vertical bands indicate boundaries between different approximations. The typical shape of the Bethe-Bloch curve may be observed for $\beta\gamma$ between about 0.1 to 1000.

2.2.1.2 Rutherford cross-section

Under the assumption, that the energy deposit of the charged particle is larger than the typical binding energies of the atomic electrons, the interaction can be considered as scattering off free electrons. The differential cross-section is then given by the Rutherford scattering on one electron,

$$\frac{\mathrm{d}\sigma}{\mathrm{d}E} = \frac{2\pi r_e^2}{\beta^2}\frac{mc^2}{E^2}, \tag{2.6}$$

where r_e is the classical electron radius.

2.2.1.3 The Photo-Absorption Ionization model

In the *Photo-Absorption Ionization* (PAI) model, developed by Allison and Cobb [32], the electromagnetic interaction of the projectile with the absorber is derived from the electric field at the position of the charged particle. The corresponding energy loss is treated as the emission and absorption of virtual photons by the incident particle and the material respectively.

By considering soft collisions with the shell electrons of the absorber only, a semi-classical treatment of the electric field can be conducted. The mean energy loss of the projectile is then solely due to the longitudinal component of E and determined by the complex dielectric constant $\varepsilon(k,\omega)$ as a function of the wave number k and the frequency ω [32],

$$\left\langle \frac{\mathrm{d}E}{\mathrm{d}x} \right\rangle = -\frac{2e^2}{\beta^2\pi}\int_0^\infty \mathrm{d}\omega \int_{\omega/\beta c}^\infty \mathrm{d}k \left[\omega k \left(\beta^2 - \frac{\omega^2}{k^2c^2}\right)\cdot \mathrm{Im}\frac{1}{-k^2c^2+\varepsilon\omega^2} - \frac{\omega}{kc^2}\cdot \mathrm{Im}\left(\frac{1}{\varepsilon}\right)\right]. \tag{2.7}$$

The dielectric constant of the medium may then be expressed in terms of the the generalized oscillator strength density $f(k,\omega)$, which gives a measure of the fraction of electrons with wave number k coupling to the electric field between ω and $\omega + \mathrm{d}\omega$. Under the assumption, that finer details of the atomic structure can be neglected in the context of the energy loss of relativistic particles, a simplified model of the generalized oscillator strength can be constructed. This model is based on the atomic photoabsorption cross section of free photons $\sigma_\gamma(\omega)$ using the dipole approximation in the resonance region for small k and point-like scattering in the quasi-free region [32]. This is very convenient as data for $\sigma_\gamma(\omega)$ are available from optical and electron energy loss measurements.

By re-interpreting the mean energy loss as a number of discrete collisions N with energy transfer $\hbar\omega$, it can be expressed in terms of the differential cross section per electron and energy loss,

$$\left\langle \frac{\mathrm{d}E}{\mathrm{d}x} \right\rangle = \int_0^\infty \mathrm{d}\omega E N \frac{\mathrm{d}\sigma}{\mathrm{d}E}\hbar. \tag{2.8}$$

With this, the differential energy transfer cross-section per electron can be computed as

$$\begin{aligned}\frac{\mathrm{d}\sigma}{\mathrm{d}E} =& \frac{\alpha}{\beta^2\pi}\left[\frac{\sigma_\gamma(E)}{EZ}\ln[(1-\beta^2\varepsilon_1)^2+\beta^4\varepsilon_2]^{-1/2} + \frac{Z}{N\hbar c}\left(\beta^2 - \frac{\varepsilon_1}{|\varepsilon|^2}\right)\theta + \right.\\ &\left. + \frac{\sigma_\gamma(E)}{EZ}\ln\frac{2mc^2\beta^2}{E} + \frac{1}{ZE^2}\int_0^E \mathrm{d}E'\sigma_\gamma(E')\right],\end{aligned} \tag{2.9}$$

where α is the fine structure constant and ε_1, ε_2 and θ can be derived from $\sigma_\gamma(\omega)$ [32]. The first and the third term represent the energy loss by ionization and it is in fact the first one, that is relevant for the relativistic increase of the cross section. The second term incorporates the energy loss by radiation and the emission of Cherenkov radiation in the limit $\varepsilon_2 \to 0$. The last term corresponds to the scattering off quasi-free electrons and dominates for energy transfers above the atomic binding energy. Therefore, for large energy transfers, Eq. 2.9 becomes the differential Rutherford cross-section.

Different models for cross sections normalized to the Rutherford cross section are compared in Fig. 2.3.

2.2.1.4 The straggling function

The spectrum of the energy transfer is determined by the differential cross section. The normalized differential probability per unit energy is given by

$$F(E) = \frac{n_e(\mathrm{d}\sigma/\mathrm{d}E)}{\int \mathrm{d}E n_e(\mathrm{d}\sigma/\mathrm{d}E)}. \tag{2.10}$$

In order to obtain the energy loss from this expression, the so-called *straggling function* $F(x,\Delta)$, which is the energy loss distribution, needs to be constructed. The two most prominent methods to obtain the straggling function are the convolution method [33] and the Laplace transformation method [34]. While these methods shall not be discussed here, a thorough review may be found in [33]. Instead, what will be of particular interest in the following, is the peculiar shape of the straggling function.

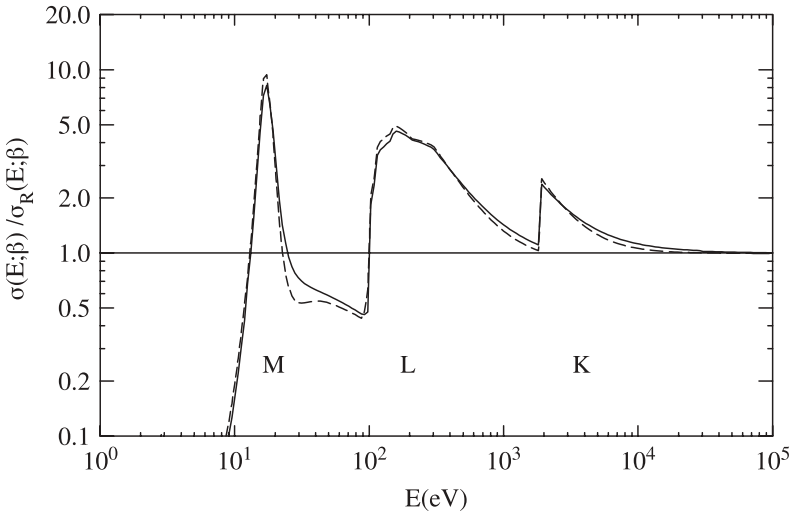

Figure 2.3: Collision cross sections for single collisions calculated with different theories in silicon for projectiles with $\beta\gamma = 4$. Figure modified from [31]. The inelastic Bethe-Fano cross section (solid line) and the PAI cross section (dashed line) are normalised to the Rutherford cross section.

In general, the energy loss distribution is characterized by an asymmetric shape with a long tail towards high energy transfers as visible in Fig. 2.4. These high-energetic electrons are due to the E^{-2} dependence of the energy loss. This is also the reason why the mean value of $F(x, \Delta)$ is significantly higher than the most probable value. The difference between the two function shown in Fig. 2.4 arises from the fact, that the Landau function (dotted line) relies only on the Rutherford cross section.

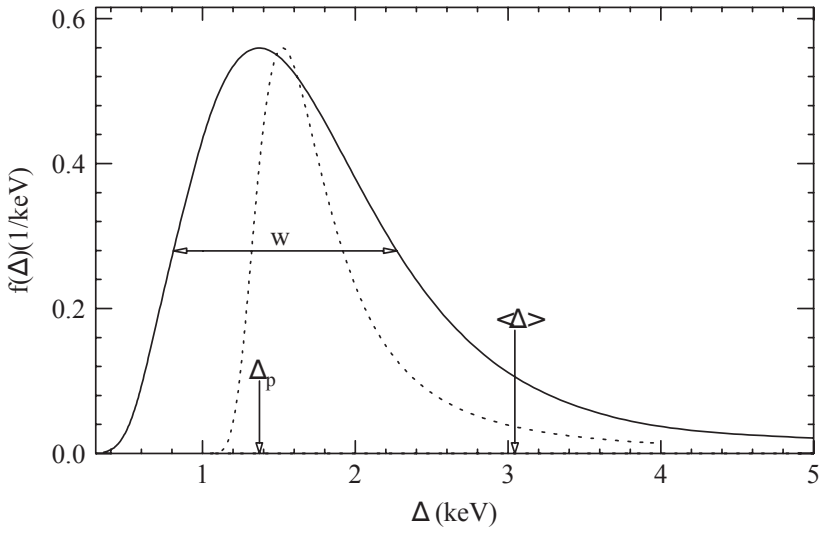

Figure 2.4: The straggling function $F(\Delta)$ for particles with $\beta\gamma = 3.6$ traversing 1.2 cm of Ar gas (solid line) together with the original Landau function (dotted line) [31]. The function is described by the the most probable value Δ_p, the FWHM (Full Width at Half Maximum) w and the mean energy loss $\langle\Delta\rangle$.

2.2.2 Drift and diffusion

The applied drift field hinders the electron-ion pairs from recombining and hence allows to access the information they carry. The force exerted by the electric field upon the electrons results in an acceleration along the field lines, towards the readout anode. However, on their path, they encounter frequent collisions with molecules and atoms of the detector gas, resulting in an effective randomization of the movement. The movement of the electrons can therefore be regarded microscopically as a *stop and go* process, while the drift macroscopically is a constant movement along the field lines. In the additional presence of a magnetic field B, the equation of motion is given by the *Langevin equation*,

$$m\frac{\mathrm{d}v_{\mathrm{drift}}}{\mathrm{d}t} = eE_{\mathrm{drift}} + e[v_{\mathrm{drift}} \times B] - Kv_{\mathrm{drift}}, \tag{2.11}$$

where m and e are the mass and charge of the electron. The frequent collisions with gas molecules are described by a friction parameter K and v_{drift} is the resulting drift velocity. A steady state for which $\mathrm{d}v_{\mathrm{drift}}/\mathrm{d}t = 0$ is then given for $t \gg \tau$, where τ defines the characteristic time between two successive collisions and is the ratio of m and K. In the absence of a magnetic field, the drift velocity is directly related the mobility μ of the respective charge carriers in a gas,

$$\mathbf{v}_{\mathrm{drift}} = \frac{eE_{\mathrm{drift}}}{m}\tau = \mu E_{\mathrm{drift}}. \tag{2.12}$$

Another effect introduced by the random collisions of charge carriers with gas molecules is the diffusion. Assuming a point-like electron cloud in the absence of both a magnetic and electric field, these collisions will result in a thermalization of the electrons. Due to this effect, the charge cloud will spread isotropically and follow a Gaussian distribution of width $\sigma = \sqrt{2Dt}$ after a certain time t, where the diffusion coefficient D is a property of the employed detector gas. The introduction of an electric field results in a preferred direction of the movement of the electrons and yields different diffusion constants in parallel (D_{L}) and perpendicular (D_{T}) to the drift field. In general, the charge spread introduced by the diffusion represents a limiting factor for the spatial resolution and scales according to the square root of the drift length,

$$\sigma = \sqrt{\frac{2DL}{\mu E_{\mathrm{drift}}}}. \tag{2.13}$$

Along their drift path, the electrons can be captured by atoms with large electron affinities, resulting in the formation of negative ions. In TPCs typically the main contribution to the *attachment* arises from impurities such as O_2 or H_2O, which contribute significantly even in very small abundances of $\mathcal{O}(10\,\mathrm{ppm})$. As this process reduces the amount of electrons reaching the readout, the quality of the detector gas is a crucial parameter and thoroughly to be monitored.

2.2.3 Amplification

As a signal induced only by the ionization electrons reaching the segmented readout anode would be imperceivable for modern readout electronics, electron multiplication is necessary. In general, the concept of electron amplification is based on the acceleration of the ionization electrons in strong electric fields of $\mathcal{O}(10\,\mathrm{kV})$, where they gain sufficient energy to ionize further gas atoms and

hence an *avalanche* of electrons is created. This results in a chain reaction in which the number of electrons n contained in such an avalanche grows exponentially along the distance x,

$$n = n_0 e^{\alpha x}, \tag{2.14}$$

where α is the first Townsend coefficient, which depends on the applied electric field and the gas density. The *effective gain* is then defined by the ratio of the electrons collected at the readout anode I_{anode} and the number of primary electrons I_{primary},

$$G_{\text{eff}} = \frac{I_{\text{anode}}}{I_{\text{primary}}}. \tag{2.15}$$

The multiplication of electrons, in turn, results in the creation of a significant amount of positively charged ions. In general, the largest fraction of these ions is not neutralized in the amplification region, but instead drifts towards the cathode; a process which can be quantified by the *Ion Backflow* (*IB*) defined as the ratio of cathode and the anode current,

$$IB = \frac{I_{\text{cathode}}}{I_{\text{anode}}} = \frac{1+\varepsilon}{G_{\text{eff}}}, \tag{2.16}$$

where ε denotes the number of ions drifting back into the active volume per incoming primary electron. Due to the large mass, the ion mobility is by almost three orders smaller compared to electrons, hence resulting in long drift times of up to 100 ms, depending on the geometry of the detector. Therefore, at interaction rates larger than the ion drift time, a sizeable amount of positive charge will accumulate in the drift volume and cause distortions of the drift field. This *space-charge effect* results in deviations of the drift lines of the ionization electrons and thus degrades the spatial resolution of the detector accordingly.

2.2.4 Signal formation

The moving charges extracted from the amplification stage induce electrical signals on the segmented readout anode. In general, the current induced on a grounded electrode by a point charge q moving along $x(t)$ is given by Ramo's theorem [35],

$$I_{\text{Ind}}(t) = -\frac{\mathrm{d}Q(t)}{\mathrm{d}t} = -\frac{Q}{V_w} E[x(t)]v(t), \tag{2.17}$$

where $E(x)$ is the electric field assuming the charge q is removed, the readout electrode of interest is set to voltage V_w, while all surrounding electrodes are grounded. In practice, the situation is not so straight forward as the charge cloud may be broadened by further effects, such as capacitive coupling of neighbouring pads on the segmented readout plane, the infinite range of the Coulomb potential and the diffusive spread of the charge cloud. This results in a potential spread of the charge over several pads. All these effects are incorporated in the pad response function (PRF), which determines the fraction of the total charge in the avalanche induced on a given pad as a function of the distance between the center of the pad and the avalanche position.

The front-end electronics then amplify and shape the induced signal of each individual pad. The signal is first integrated by the pre-amplifier and then differentiated by the shaper.

2.3 Particle identification via the measurement of the specific energy loss

Under the assumption that all ionization electrons reach the amplification stage and are registered by the front-end cards, the measured signal height is proportional to the energy deposit of the incident particle. Due to the fact, that the typical mean free path λ is much smaller than the size of the readout pads, the charge freed by several collisions is integrated by the readout and combined to a so-called *cluster*. For a sufficiently large number of clusters along a particle's trajectory, the distribution of the cluster charges Q approaches the straggling function $F(x, \Delta)$. Due to the structure of this distribution, its mean value $\langle \mathrm{d}E/\mathrm{d}x \rangle$ is not a good estimator of the energy deposit, as it is very sensitive to entries in the high energy tail. Instead, usually the peak of the distribution, its *Most Probable Value* (MPV), is considered. In order to facilitate its extraction, the distribution of the cluster charges Q is symmetrized. Therefore, the technique of the truncated mean $\langle \mathrm{d}E/\mathrm{d}x \rangle_{\mathrm{tr}}$ is used, which is defined as the average over a subset of the cluster charges Q_i and can be computed by discarding a fraction of the lowest and/or highest charges Q contained in the distribution,

$$\langle \mathrm{d}E/\mathrm{d}x \rangle_{\mathrm{tr}} = \frac{1}{(b-a)\cdot N} \sum_{i=a\cdot N}^{b\cdot N} Q_i, \tag{2.18}$$

where $Q_i \leq Q_{i+1}$, a ranges typically between 0 and 0.15 and b between 0.5 and 0.85. With properly chosen values of a and b, $\langle \mathrm{d}E/\mathrm{d}x \rangle_{\mathrm{tr}}$ approaches a Gaussian distribution. The absolute resolution of the ionization measurement is the given by its variance $\sigma_{\langle \mathrm{d}E/\mathrm{d}x \rangle_{\mathrm{tr}}}$, while the relative resolution, in the following referred to as $\mathrm{d}E/\mathrm{d}x$ resolution, is defined as

$$\mathrm{d}E/\mathrm{d}x \text{ resolution} = \frac{\sigma_{\langle \mathrm{d}E/\mathrm{d}x \rangle_{\mathrm{tr}}}}{\mu_{\langle \mathrm{d}E/\mathrm{d}x \rangle_{\mathrm{tr}}}}. \tag{2.19}$$

Figure 2.5 shows the energy deposit as a function of momentum measured with the ALICE TPC using the approach of the truncated mean. In pp collisions, this apparatus, which will be described in the next section, provides a $\mathrm{d}E/\mathrm{d}x$ resolution of about 5.2 %. Owed to the high occupancy in the 0–5 % most central Pb–Pb collisions, the resolution in this case is slightly degraded to about 6.5 % [5].

The separation power of particles with the same momentum but of different species is given by

$$\text{Separation power} = \frac{2 \cdot |\mu_{\langle \mathrm{d}E/\mathrm{d}x \rangle_{\mathrm{tr},e^-}} - \mu_{\langle \mathrm{d}E/\mathrm{d}x \rangle_{\mathrm{tr},\pi^-}}|}{\sigma_{\langle \mathrm{d}E/\mathrm{d}x \rangle_{\mathrm{tr},e^-}} + \sigma_{\langle \mathrm{d}E/\mathrm{d}x \rangle_{\mathrm{tr},\pi^-}}}, \tag{2.20}$$

for the exemplary case of electrons and pions.

An empirical formula has been obtained by fits to measured data to estimate the dependence of the $\mathrm{d}E/\mathrm{d}x$ resolution on the number of samples N, the thickness of the corresponding layers x and the ambient pressure P [36, 37],

$$\mathrm{d}E/\mathrm{d}x \text{ resolution} = 0.41 \cdot N^{-0.43} \cdot (x \cdot P)^{-0.32}. \tag{2.21}$$

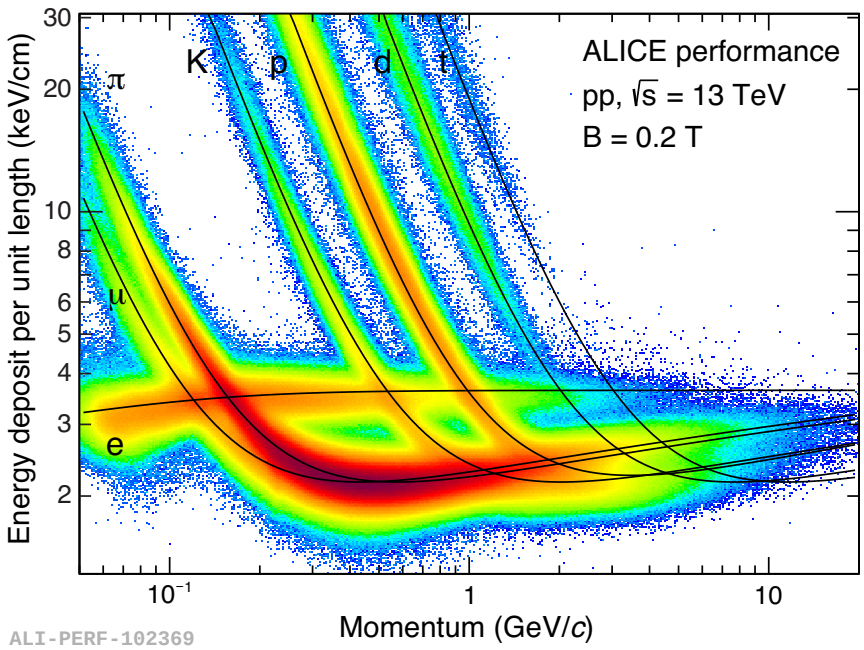

Figure 2.5: Energy deposit as a function of momentum measured with the ALICE TPC at magnetic field of 0.2 T and $\sqrt{s}$ =13 TeV. The black lines represent a parametrized Bethe-Bloch function introduced in Eq. 2.5.

2.4 Technical design of the ALICE TPC

The ALICE Time Projection Chamber is the main device for charged-particle tracking, momentum measurement and particle identification (PID) in the central barrel of the ALICE experiment. At the time of its design, multiplicities of up to $\mathrm{d}N_{\mathrm{ch}}/\mathrm{d}\eta = 8000$ were anticipated for central Pb–Pb collisions at a center of mass energy of $\sqrt{s} = 5.5$ TeV. For this reason, the TPC has been optimized in particular for rate capability in a high track density environment [11]. The TPC covers a transverse momentum range $0.1 < p_{\mathrm{T}} < 100$ GeV/c within the pseudo rapidity range $|\eta| \leq 0.9$ and full azimuth.

The TPC consists of a hollow cylindrical barrel with an overall volume of about 90 m^3, the cathode in its center and two readout planes on its sides. The drift field of 400 V/cm is precisely defined by the central electrode at the center of the TPC and a cylindrical field cage degrading the potential from 100 kV at the cathode to nearly ground potential close to the readout chambers. The active volume has an inner radius of 84.8 cm, an outer radius of 246.6 cm and an overall length along the beam axis of 499.4 cm.

A schematic layout of the TPC is shown in Fig. 2.6 with its most important components depicted.

During the LHC RUN1 (2010-2013), the detector was filled with a counting gas consisting of a mixture of Ne-CO_2 (90-10) at atmospheric pressure. For the RUN2 (2015-2018), the gas was exchanged to Ar-CO_2 (90-10) in order to enhance the stability against electric discharges.

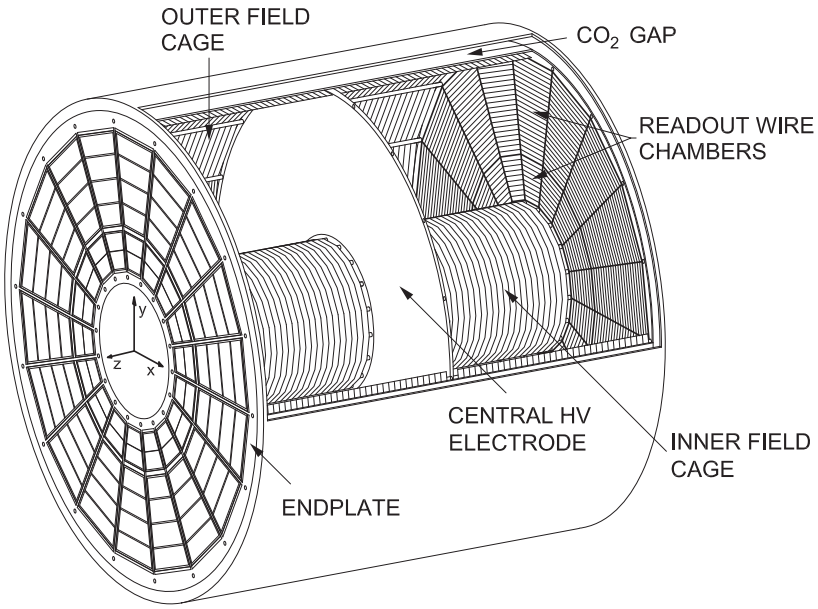

Figure 2.6: Schematic drawing of the ALICE TPC [38].

2.4.1 Readout chambers

The two endplates are azimuthally segmented into 18 sectors, each covering 20°. A further division of each sector into *Inner* (IROC) and *Outer Readout Chamber* (OROC) is motivated by the different requirements for the readout chambers as a function of the radius due to the radial dependence of the track density. The design of the readout chambers is based on a gated MWPC with cathode pad readout operated at a gain of 7000-8000. The total amount of readout pads is 557,568 covering in total an area of 32.5 m^2.

The mechanical structure of the Readout Chambers is given by four main components: the wire planes, the pad plane, an additional insulation plate (*strong back*) and a trapezoidal aluminium frame (*alubody*).

2.4.1.1 Wire planes

A commonly used scheme of wire planes is employed - a grid of anode wires above the segmented readout plane, a cathode wire-grid and a gating grid with the wire orientation in azimuth. As the requirements for Inner and Outer Readout Chambers differ, the geometries of the respective wire planes have been adopted accordingly, as summarized in Tab. 2.1. Figure 2.7 shows a schematic cross section of a readout chamber with the individual wire planes depicted. A cover electrode on top of the wire planes serves to maximize the homogeneity of the drift field.

In order to minimize the charge accumulated per unit length of the anode wire and thus rate-induced gain variations, a small anode wire pitch was chosen. The cathode wire grid separates the drift volume from the amplification region. Hence, a large number of ions produced in the gas amplification process around the anode wires are collected at the cathode wire plane.

Table 2.1: Summary of the wire parameters.

Plane	Diameter [µm]	Material	Pitch [mm]	Distance [mm]
Gating grid	75	copper-beryllium	1.25	
				3
Cathode wire grid	75	copper-beryllium	2.5	
				2/3[1]
Anode wire grid	20	gold-plated tungsten	2.5	
				2/3[1]
Pad plane				

The active gating grid (GG) is located above the cathode wire plane. Upon a trigger, it switches to transparent mode and all gating wires are supplied with the same potential V_{G}, allowing for the ionization electrons stemming from the active drift volume to reach the amplification region. After the maximum drift time for electrons (100 µs), the GG wires are biased with an alternating voltage $V = V_{\mathrm{G}} \pm \Delta V$ rendering it opaque to electrons and ions. In particular, ions produced in the amplification process are hindered from drifting back into the active drift volume, where they would otherwise cause significant space-charge accumulations and hence distort the drift field. The resulting requirement is to keep the ion backflow from the amplification region below 10^{-4}.

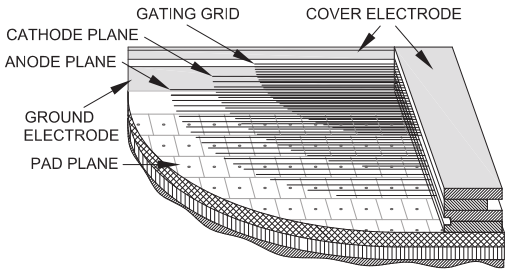

Figure 2.7: Cross section through a readout chamber showing the pad plane, the wire planes and the cover electrode [38].

The maximal drift time of the ionization electrons (100 µs) and the minimal necessary closure time of the GG imply a rate limitation to a few kHz for the TPC.

2.4.1.2 Pad plane

The pad plane is a multilayer printed circuit board (PCB) with a thickness of 3 mm. The size of the pads has been optimized in terms of momentum and $\mathrm{d}E/\mathrm{d}x$ resolution [11] and increases with increasing radius and accordingly decreasing track density. The corresponding pad parameters are summarized in Tab. 2.2.

The pad geometry varies from rectangular pads in the center of the short axis of the trapezoid to parallelograms close to the borders, as shown in the layout of the pad plane of the IROC in Fig. 2.8. The pads are routed to connectors on the back side of the pad plane, where the front-end electronics can be connected via short and flexible flat cables.

1 IROC/OROC

Table 2.2: Dimensions and parameters of readout planes and pads.

		Pad size [mm^2]	Rows	Pads
IROC	$(841 < r < 1321\,\text{mm})$	4×7.5	63	5,504
OROC	$(1346 < r < 1986\,\text{mm})$	6×10	64	5,952
OROC	$(1986 < r < 2466\,\text{mm})$	6×15	32	4,032
TPC total			159	557,568

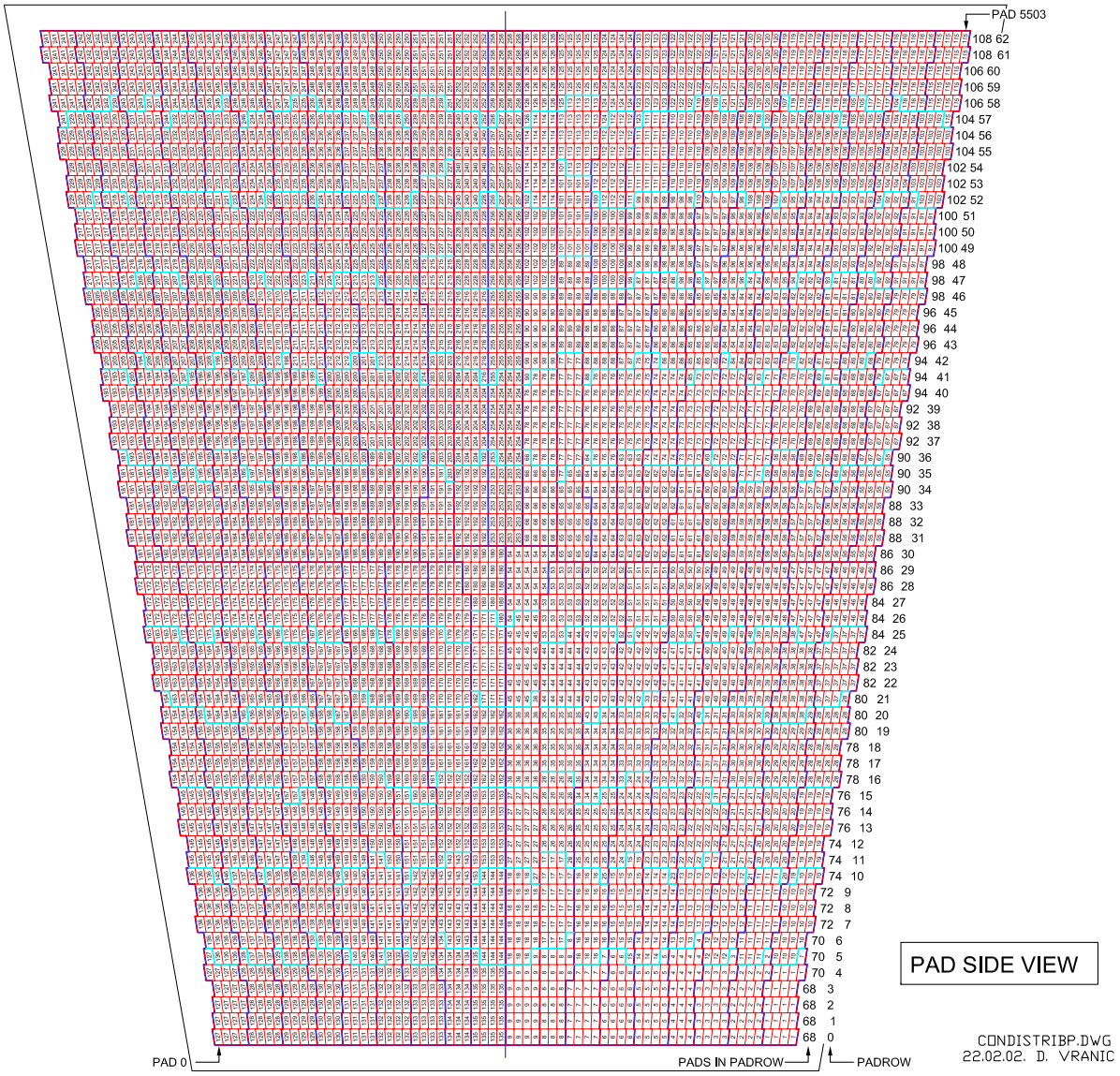

Figure 2.8: Pad plane of the IROC.

2.4.1.3 Alubody and strong back

In order to enhance the mechanical stiffness and gas tightness, the *strong back*, a plate made from fibreglass-epoxy (Stesalit®) with a thickness of 3 mm, is glued to the back side of the pad plane.

The mechanical stability of the chamber is provided by the alubody, thus preventing deformations due to both gravitational forces and wire tension. A cooling pipe introduced to the alubody removes residual heat not taken away by the cooling of the front-end cards.

2.4.2 Limitations

The necessity to operate the TPC in a gated mode sets severe constraints on the maximally achievable readout rate. The time necessary to read out all ionization electrons stemming from the active volume and to clear the amplification region from ions created during the amplification process allows for no more than 3.5 kHz in pp. The currently used readout electronics impose a further constraint to ∼300 Hz in Pb–Pb. Due to the limited bandwidth, the readout time can reach up to 4 ms for central Pb–Pb events, depending on the number of tracks. Moreover, the electronics suffer from radiation effects, which can cause the readout to be stuck and runs to be prematurely stopped. With a newly designed readout component, the RCU2 [39], the present readout rate is supposed to be enhanced by a factor of up to 2.6.

Nevertheless, the present rate constraints matched well the typical Pb–Pb collision rates during RUN1. With the introduction of the RCU2, the TPC readout will be enabled to conform to the running scenario envisaged for RUN2.

In RUN3 however, the interaction rate will be increased to 50 kHz, implying an average event pileup of 5 given by the maximum drift time of electrons (100 µs) together with the average event spacing (20 µs) [23]. A triggered operation of the TPC with a gating grid will then be no longer possible, as is would cause unacceptable losses of data. Hence, a continuous operation of the TPC is mandatory, as is the minimization of the ion backflow with other means than a gating grid.

3 GEM – Gas Electron Multiplier

The introduction of the MWPC in 1968 constituted a revolution in the instrumentation of particle physics experiments, as it for the first time allowed for the construction of large-size detectors for ionizing particles that could be read out by electronics means. Ever since, the MWPC has been a widely used tool and continuously been improved. However, its intrinsic limitations have been reached in particular concerning high-rate capability [40] and granularity due to the discrete wire spacing.

With the introduction of the the Micro Strip Gas Chamber (MSGC) in 1988 by A. Oed [41], some of the limitations of the MWPC seemed to be overcome. However, this kind of detector has proven to be vulnerable to destructive discharges [42], but its introduction nevertheless triggered the development of a new generation of different devices: micro-gap, micro-wire, micro-dot, field gradient lattice and others collectively named *Micro Pattern Gas Detectors* (MPGD) - for a review see e.g. [43]. Enabled by the progress in photo-lithographic technology, all these devices rely on the substitution of the MWPC's wires by finer micro-structures (<100 µm). This however imposes some difficulties concerning the achievable size and quantity and moreover most of the observed problems derive from the fragility of the micro-structures. Nowadays, mainly the *Gas Electron Multiplier* (GEM) [44] and the *MICRO-MEsh GAseous Structure* (MICROMEGAS) [45] play a prominent role in the instrumentation modern high-energy physics experiments.

Introduced in 1996 by F. Sauli, the large-scale application of GEMs was pioneered by the triple-GEM tracking detectors for the COMPASS experiment [46]. Presently, GEM-based detectors are employed in a vast number of experiments, such as LHCb [47], PHENIX [48] and TOTEM [49]. Moreover, this technology is foreseen for future detector upgrades, e.g. for the CMS muon system [50] or the ALICE TPC [24].

3.1 Working principle

The Gas Electron Multiplier is a 50 µm thin polyimide foil with a copper coating of about 5 µm thickness on both sides. This structure is perforated via photo-lithographic processing with a regular, hexagonal pattern of usually double-conical holes with an inner/outer diameter of about 50/70 µm and a typical hole pitch of 140 µm. Figure 3.1 shows electron microscope image of a GEM foil.

Upon application of a moderate potential difference of the order of 300-400 V, the electric field inside a GEM hole can reach up to several tens of kV/cm, in which drifting electrons can acquire sufficient energy to undergo ionizing collisions with the gas molecules - hence avalanche multiplication of the electrons occurs. The such produced electrons are extracted from the bottom electrode of the GEM to either the readout anode or to a further GEM foil.

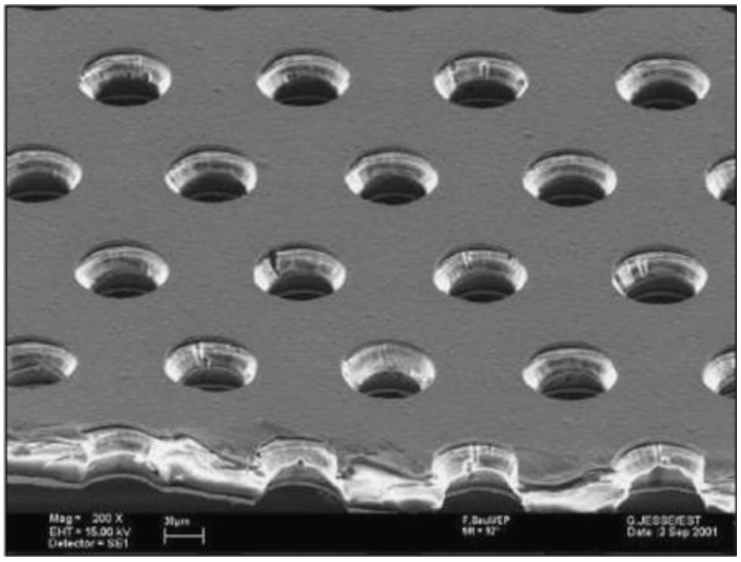

Figure 3.1: Electron microscope picture of a section of typical GEM electrode [46].

With single foils, gains of the order of 10^4 can be reached, however at the price of enhanced discharge rates [51]. To this end, the overall gain is usually divided between several consecutive foils mounted in a stack on top of each other.

The ions created in the avalanche, due to their much smaller diffusion, follow closely the field lines. This is depicted in Fig. 3.2, which shows a Garfield/Magboltz [53] simulation, where two primary electrons enter a GEM hole and avalanche amplification occurs. Operating the GEM

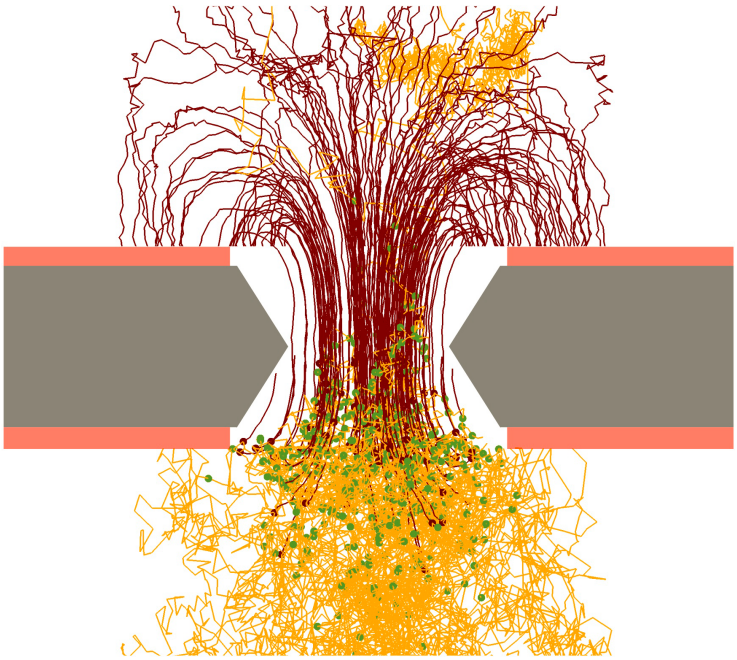

Figure 3.2: Garfield/Magboltz simulation of charge dynamics for two electrons entering into a GEM hole [52]. Electron drift paths are shown as light lines, ion drift paths as dark lines. Dots mark places where ionization processes have occurred. The paths have been projected onto the cross section plane.

in an asymmetric voltage configuration, in which the electric field below the GEM foil is higher than above, most of the ions are collected on the top electrode and thus, only a small fraction of the ions can escape into the drift volume. This mechanism is known as intrinsic suppression of the ion backflow. For stacks containing three and four GEM foils in a specific configuration introduced in the next section, an *IB* of $\sim 2.5\,\%$ [24] and $0.4\,\%$ [25] respectively has been reached. These values have been achieved within the scope of the upgrade program of the ALICE TPC in the envisaged detector gas Ne-CO_2-N_2 without the presence of a magnetic field.

A crucial issue regarding the operation of GEM-based detectors in harsh environments is the stability against electrical discharges (sparks). Due to the short distance between the two electrodes of a GEM, the ionization channel formed by a streamer can connect the two electrodes and hence cause electrical breakdown. The occurrence of sparks is supposed to be related to high charge densities inside single holes; a situation somewhat similar to the *Raether limit* [54] in parallel plate chambers. The energy released by such a spark may damage the front-end electronics or the GEM foil itself and therefore, the occurrence of such events has to be minimized.

The signal on the readout anode is solely formed by electrons, which translates into a very short pulse width of around 15 ns [55]. The long signal tail caused by the ions is cut off as their charge is screened by the GEM electrodes. Consequently, GEMs provide an excellent time resolution.

3.2 GEM upgrade of the ALICE TPC

The application of a GEM-based readout in combination with a TPC is in particular attractive due the excellent time resolution, which is crucial for the determination of the z-coordinate, and the intrinsic ion-blocking capabilities. In fact, the latter allows for a continuous operation without an active gating grid under the prerequisite of a carefully optimized HV configuration.

The application of a GEM-based readout chamber with a TPC has been pioneered by [56], a TPC prototype developed for the $\bar{\text{P}}$ANDA experiment and equipped with a stack of three GEM foils. The TPC prototype is a cylindrical volume with an inner/outer diameter of 10.4/30.8 cm and a drift length of 72.78 cm, operated in Ar-CO_2 (90-10). The high granularity (more than 10,000 hexagonal pads) yields an excellent spatial resolution of 182 µm in $r\varphi$ measured in the first 12 cm of the drift length [57]. The $\mathrm{d}E/\mathrm{d}x$ resolution has been determined to 14-18 % with around 20 samples per track [58], where the tracks stem from a 1.7 GeV/c π^- beam impinging on a carbon target. The prototype hence demonstrated the excellent performance of a GEM-based TPC.

The adoption of this concept to the ALICE TPC, however, imposes the necessity for further optimization, in particular of the HV configuration. In fact, the intrinsic ion backflow capabilities of a typical stack of GEMs are by almost three orders of magnitude worse compared to an active gating grid.

Therefore, a careful optimization of the HV configuration is mandatory, yet not sufficient. Due to the slow ion drift velocity, the ions of on average 8,000 events accumulate in the active volume of the ALICE TPC at a mean interaction rate of 50 kHz. The resulting field distortions modify the electron drift paths and hence lead to distortions reaching up to 19 cm in r and 7 cm in $r\varphi$ close to the central electrode at an *IB* of 1 % [24], which is shown in Fig. 3.3. For the largest part of the active volume, however, the space-charge distortions remain well below 10 cm. These space-charge distortions are corrected using a multi-step approach: an average distortion map, scaled according to the instantaneous TPC occupancy, is applied at first. The remaining distortions are corrected

by comparing the TPC cluster positions to interpolated tracks measured with external detectors, namely the ITS and the TRD. By applying these corrections, the intrinsic detector resolution can be restored [25]. The calibration strategy has been tested up to twice the expected interaction rate and an *IB* of 2 % without finding any deterioration [25]. Leaving an additional factor of two as a safety margin, the resulting requirement is to keep the *IB* below 1 %.

A typical optimization of the *IB* is conducted by subsequently increasing the gain of each GEM towards the readout anode, as such ions created in the inner two layers are blocked more efficiently. Then, the largest contribution to the remaining *IB* arises from the uppermost foil. Therefore, a further suppression of the *IB* can only be achieved by reducing the gain in this foil. Due to the resulting field configuration, more ions are then collected on the top electrode and correspondingly the contribution of the uppermost foil in the stack to the overall *IB* is reduced. However, by reducing the gain, the electron efficiency degrades and accordingly an improved *IB* affects the energy resolution. Consequently, in parallel to an optimization of the HV configuration with respect to the *IB*, the resulting energy resolution has to be thoroughly monitored. The corresponding requirement arises from simulations, as it has been shown that a local energy resolution equivalent to 14 % at the ^{55}Fe peak is sufficient to retain the present $\mathrm{d}E/\mathrm{d}x$ resolution of the TPC [25].

Further requirements arise from the required signal-to-noise ratio of 20, which demands for an overall gain of 2000, and the necessity to assure maximal stability of the chambers against electrical discharges in the harsh LHC environment.

These challenging requirements could not be met by a stack of three standard GEMs [24]. A natural solution is to add one further foil to the stack, which in fact is the baseline solution for the upgrade of the ALICE TPC. The cross-section of such a stack of four foils, in a configuration containing both Standard (S, pitch 140 µm) and Large Pitch foils (LP, pitch 240 µm) in the order S-LP-LP-S, is shown in Fig. 3.4. This choice is in particular motivated by the reduced optical transparency of the two intermediate foils, which efficiently block the ions stemming from the last amplification stage, where the charge density and accordingly the amount of produced ions is supposed to be highest. On the contrary, a random alignment of the GEM holes in adjacent foils

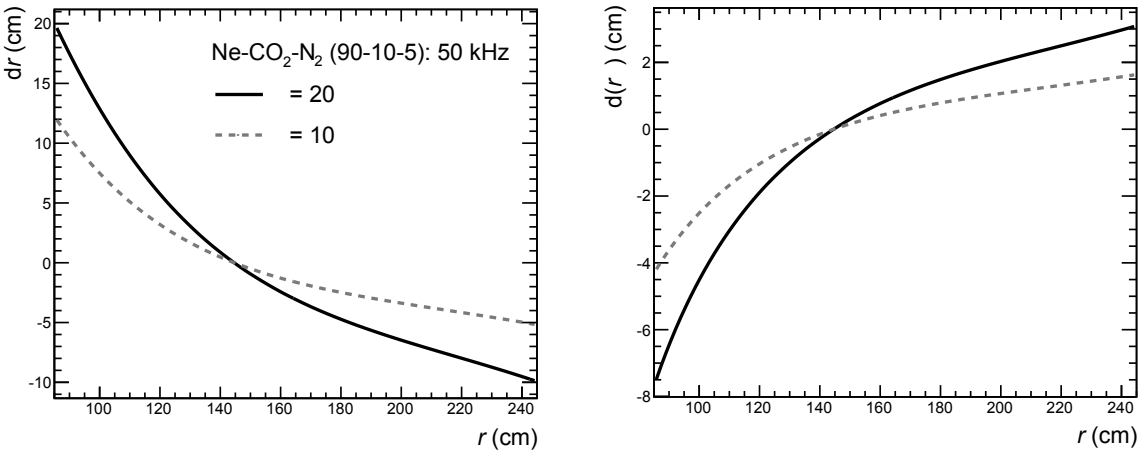

(a) **(b)**

Figure 3.3: Space-point distortions in r (a) and $r\varphi$ (b) as a function of the radius at $z \approx 0$ cm for $\varepsilon = 10$ and 20 [24].

in a stack obviously decreases the local detector performance in terms of *IB*, as it results in a very advantageous path for the ions to pass through the stack. Therefore, the masks used for perforating the foils with the hole pattern are rotated by 90° for consecutive foils. This prevents the occurrence local performance variations, as the hexagonal GEM hole pattern obeys a 60° rotational symmetry.

The outcome of the optimization of the HV configuration with respect to both *IB* and energy resolution measured at the ^{55}Fe peak is shown in Fig. 3.5, which illustrates the competing mechanisms of electron transmission and suppression of the *IB*. The results are obtained for different combinations of ΔU_{GEM1} and ΔU_{GEM2} and at different ratios $\Delta U_{\mathrm{GEM3}}/\Delta U_{\mathrm{GEM4}}$. The numbering scheme for the GEM foils is depicted in Fig. 3.4. As expected, the *IB* improves for reduced gains in GEM1 and GEM2, while the energy resolution deteriorates accordingly [24].

The correspondingly applied potentials [24], defined by a very low E_{T3}, are summarized in the lower part of Tab. 3.1, while the first row corresponds to a configuration yielding a similar performance at a much larger E_{T3} [25]. Also included are extreme values in order to identify possible performance limits of the detector.

The stability against electrical discharges of all *IB* optimized settings close to the nominal working point has been verified with measurements in the lab. Moreover, a large-size prototype of an Inner Readout Chamber (see Sec. 4.2) has been tested with a secondary pion beam with a momentum of 150 GeV/c hitting an iron absorber, yielding a discharge probability of $(6.4 \pm 3.7) \times 10^{-12}$ per incoming hadron. This translates into about 650 discharges for the whole TPC in a typical yearly heavy-ion run at 50 kHz and does not pose any risk to the GEM detectors [25].

Hence, a suitable working point fulfilling all requirements has been found.

3.2.1 GEM design

Conventional GEM fabrication is based on photo-lithographic processing of the copper-polyimide-copper structure with two masks having an identical hole pattern. In order to obtain the required precision with respect to hole size and diameter, the two masks have to be aligned with a precision

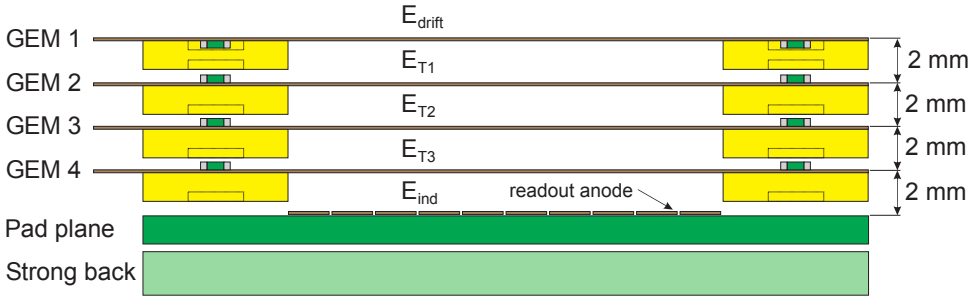

Figure 3.4: Schematic exploded cross section of the GEM stack [24]. The gap between adjacent GEM foils is defined by a 2 mm thick frame. The commonly used designations of the GEM foils and electric fields are also given. E_{drift} corresponds to the drift field, $E_{\mathrm{T}i}$ denote the respective transfer fields between GEM foils and E_{ind} the induction field between the last GEM and the pad plane. The readout anode is indicated as well. The drift electrode defining the corresponding field is not shown in this schematic.

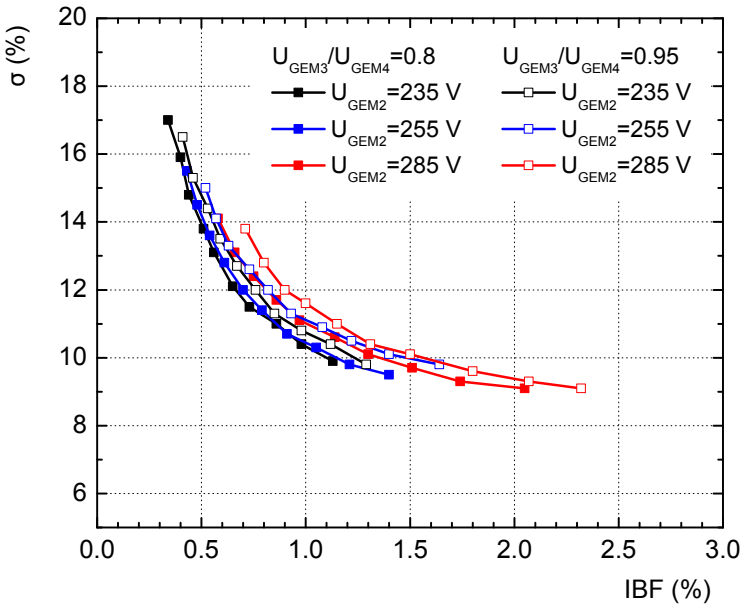

Figure 3.5: Correlation between ion backflow and $\sigma(^{55}\mathrm{Fe})$ in a quadruple S-LP-LP-S GEM-stack for various settings of the potential across GEM2 [24]. The voltage on GEM1 increases for a given setting between 225 and 315 V from left to right. The voltages on GEM3 and GEM4 are adjusted to achieve a total effective gain of 2000, while keeping their ratio fixed. The transfer and induction fields are 4, 2, 0.1 and 4 kV/cm respectively.

Table 3.1: Voltage settings for different values of *IB* and $\sigma(^{55}\mathrm{Fe})$ [24, 25].

IB [%]	$\sigma(^{55}\mathrm{Fe})$ [%]	ΔU_{GEM4} [V]	ΔU_{GEM3} [V]	ΔU_{GEM2} [V]	ΔU_{GEM1} [V]	E_{T1} [kV/ cm]	E_{T2} [kV/ cm]	E_{T3} [kV/ cm]	E_{ind} [kV/ cm]
0.63	11.3	275	240	254	317	2	3	1	4
0.34	17.0	225	235	304	382	4	2	0.1	4
0.51	13.8	255	235	292	364	4	2	0.1	4
0.65	12.1	275	235	284	345	4	2	0.1	4
0.98	10.4	305	235	271	339	4	2	0.1	4
2.05	9.1	315	285	240	300	4	2	0.1	4
0.76	12.0	275	235	308	323	4	2	0.1	4

of a few µm. As this is an increasingly difficult requirement for larger foil sizes, the overall size for GEMs is limited by this technique. In order to circumvent this restriction, a manufacturing process based only on a single-mask has been developed [59] and yields comparable results. Nevertheless, the maximal achievable size is constraint by the raw material dimensions, which allow for a width of no more than ∼60 cm. Hence, the fabrication of one foil covering the whole OROC is beyond the technological limits so far.

The natural solution is a radial segmentation of the detector modules. While the maximal available foil size is sufficient for the IROC, which will be equipped with one stack of four GEMs, the OROC will be divided into three independent stacks, thus introducing two insensitive zones of 2 cm width in radial direction in each OROC.

One side of each GEM foil is divided into segments with an area of ∼100 cm^2, as this limits the charge available in case of a spark and thus protects the detector against destructive discharges.

The distances between two neighbouring sectors are 200 µm, while the sector boundaries overlap with the edges of the pad rows in order to minimize the such introduced dead area. The foil parameters summarized in Tab. 3.2, while Fig. 3.6 depicts the most prominent features of the GEM design.

The individual sectors are powered via large (10 MΩ for GEM 1-3 and 1 MΩ for GEM 4 respectively) SMD[1] resistors, as hence the total current flowing during a discharge is minimized [51]. The resistors are soldered onto the foil and connected to a HV distribution circuit on the foil edge, that can be connected via the flap to an external power source. The unsegmented side of the foil is powered directly via the flap on the opposite side of the foil. The flaps are positioned anti-symmetrically in order to maximize the clearance between the flaps of neighbouring chambers. The flap position of each respective GEM foil in the stack is fixed, such that two adjacent foils do not use the same flap position.

In order to assure the homogeneity of the drift field, the area covered by insulator facing the central electrode has to be minimized. Therefore, the uppermost GEM is mounted with the unsegmented side facing the drift volume with its copper area extended by 5 mm towards the chamber boundaries.

In order to define stable and uniform conditions throughout the whole detector, it is of particular importance to assure the distance between two adjacent foils in a stack constantly being 2 mm. To this end, the foils are glued onto frames, which not only provide a constant distance, but also enhance the overall mechanical stability of the system as well as facilitate handling and mounting. The frames are glued together from four Vetronite® ledges with a width of 10 mm, which represent the four corresponding sides of the trapezoid. In order to compensate for the electrostatic attraction of adjacent foils, a 1.5 mm thin cross is introduced to the frame.

The frames for the prototypes as described in Chap. 4 are milled from G10 fibreglass, have a width of 10 mm and feature a 400 µm thin spacer grid at each inter-sector boundary.

Between the frame area and the active GEM area with holes, a 1 mm clearance is introduced in order to account for imprecise alignment while gluing.

Table 3.2: GEM foil parameters.

Segment	**Size (outer foil)** [$\mathbf{cm^2}$]	**Active area** [$\mathbf{cm^2}$]	**Sectors**	**Mean sector area** [$\mathbf{cm^2}$]	**RMS sector area** [$\mathbf{cm^2}$]
IROC	53.54×53.54	1665	18	92.5	3.8
OROC 1	68.74×53.54	1738	20	86.9	8.3
OROC 2	84.04×53.54	2299	22	104.5	10.8
OROC 3	104.34×53.54	2932.8	24	122.2	13.2

1 Surface Mount Device

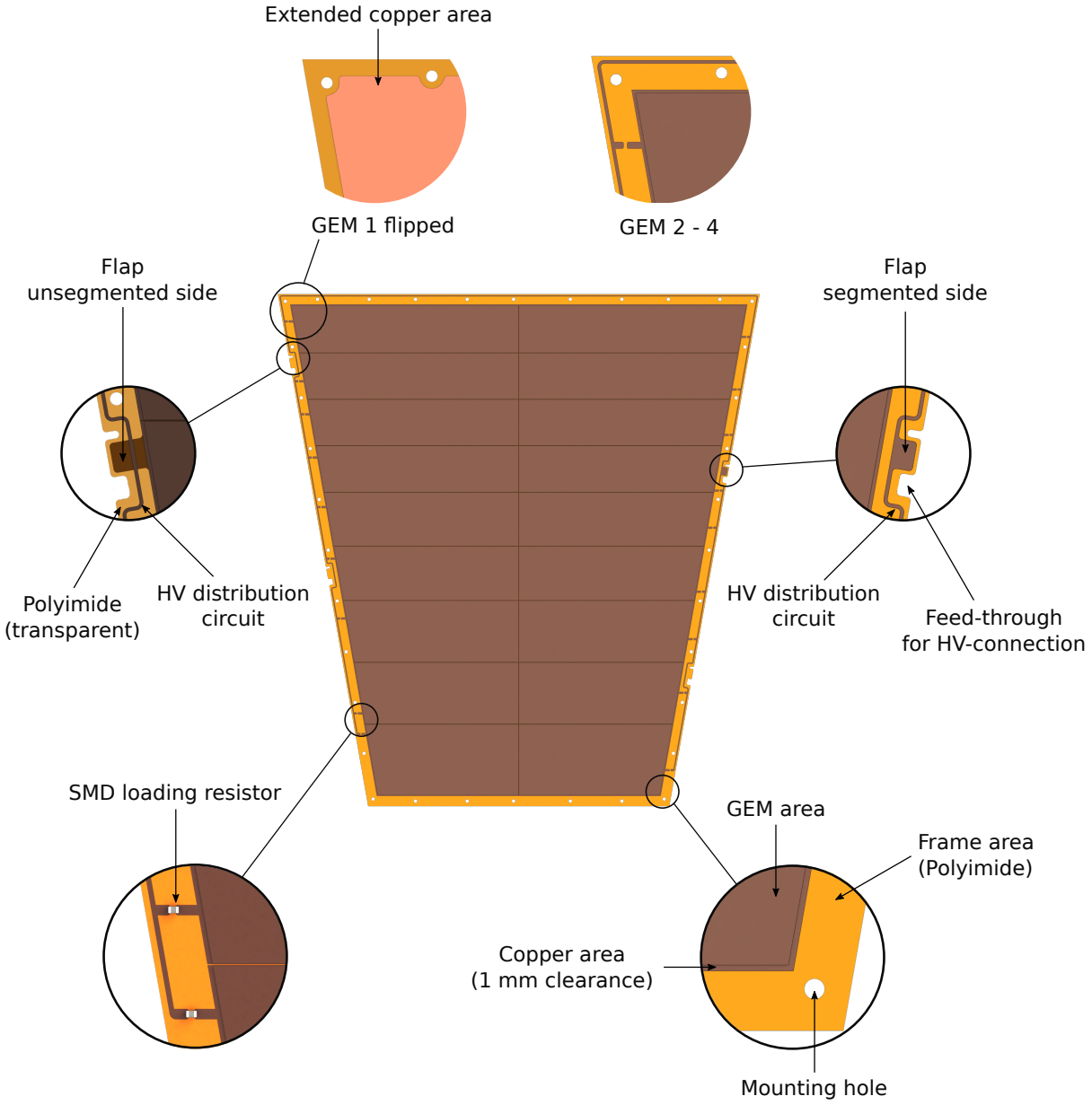

Figure 3.6: Most prominent features of the GEM design. For details see text.

4 Full-size prototypes for the ALICE TPC upgrade

In order to demonstrate the feasibility of GEM integration on large-size detectors and to validate the system performance in terms of $\mathrm{d}E/\mathrm{d}x$ resolution and operational stability, prototypes of both the IROC and OROC are built, commissioned and tested. The quality of individual GEM foils is monitored throughout the whole process. A protocol for the gluing procedure and the final integration is established and the detectors are prepared accordingly.

4.1 Production methods

As the mass production of readout chambers for the upgrade of the TPC is starting in the beginning of 2016, it is mandatory to define in advance clear assembly steps in order to assure a homogeneous quality of the readout chambers and accordingly an optimal performance of the TPC. Moreover, weak points of the procedure endangering the integrity of the detector are to be identified. The quality of the GEM foils is monitored both by means of optical and electrical characterization. The foils are glued to frames in order to define the distance between adjacent foils in a stack and to assure a constant mechanical tension on the GEM foil. Four foils in the configuration S-LP-LP-S are combined to a stack and assembled on the alubody.

4.1.1 Quality assurance

The quality of the GEM foils obviously severely impacts the performance and stability of the detector. Hence, a thorough monitoring during the process of production by means of clearly defined quality criteria is mandatory to properly select GEM foils for assembly into the readout chambers. The procedure described in the following is based on the experience of the COMPASS collaboration [46] and has been adjusted accordingly for the specific needs for the upgrade of the ALICE TPC.

4.1.1.1 HV test

The HV test, performed at every stage of assembly, serves to identify damaged foils, as an enhanced discharge rate and an increased leakage current are clear indications of poor foil quality. Moreover, this step is also supposed to enhance the stability of the detector, as residual dust or remnants from the production may be burnt by sparks.

The GEM sectors are sequentially supplied with a high voltage of 600 V at a current limit of 4 µA, while the surrounding sectors, as well as the bottom side of the foil are kept at ground potential. The leakage current of the foil is monitored with a Picoamperemeter and the spark rate

is supervised by eye. In case the leakage current has settled to $I_{\text{leak}} < 0.5\,\text{nA}$, the sparking has ceased and no cumulatively sparking spots have been observed, the test is considered as passed. This procedure is repeated sequentially for each sector. If all sectors passed the test, the foil can proceed for preparation for the prototype. If not, it is sent back to the producer for cleaning, which is the only possibility to restore a potentially damaged foil, but not to 100 % effective.

4.1.1.2 Optical inspection

The next step is an optical check of the foil under microscope. The inner and outer diameter of a defined set of GEM holes is measured in order to monitor the conformity of the GEM foil, which serves obviously as an additional indication of the foil quality. Moreover, severe defects that passed the HV test can thus be identified.

Figure 4.1 shows the variation of the inner hole diameter of a standard $10\times10\,\text{cm}^2$ GEM foil measured with an optical scanning system. This procedure is also foreseen as a QA step for each foil for the upgrade of the ALICE TPC [24]. These maps can then be used to choose foils for assembly into a GEM stack, as in this way an accumulation of unwanted features in similar positions can be avoided. The optical scanning system is also capable of identifying defects.

These defects may occur in the form of under- or over-etched holes that hint to problems in the manufacturing process, as well as chemical residues from the production. Moreover, droplets of glue or dust attached to the foil, very large holes, missing holes or mechanical defects such as cuts have to be identified. Whereas Fig. 4.2a shows a typical *fatal* defect, that prohibits the usage of this foil, the defect in Fig. 4.2b may only introduce local gain variations. Problematic however are especially small holes, as due to the thus altered electric field, the gain is locally increased and so is the discharge probability. As defects in general may alter the stability and/or the performance of the detector while operation, affected foils are not to be used. Depending on whether the problem of the foil is caused by defects or dirt, it may be resolved by cleaning the foil by the producer, while physical defects obviously cannot be cured.

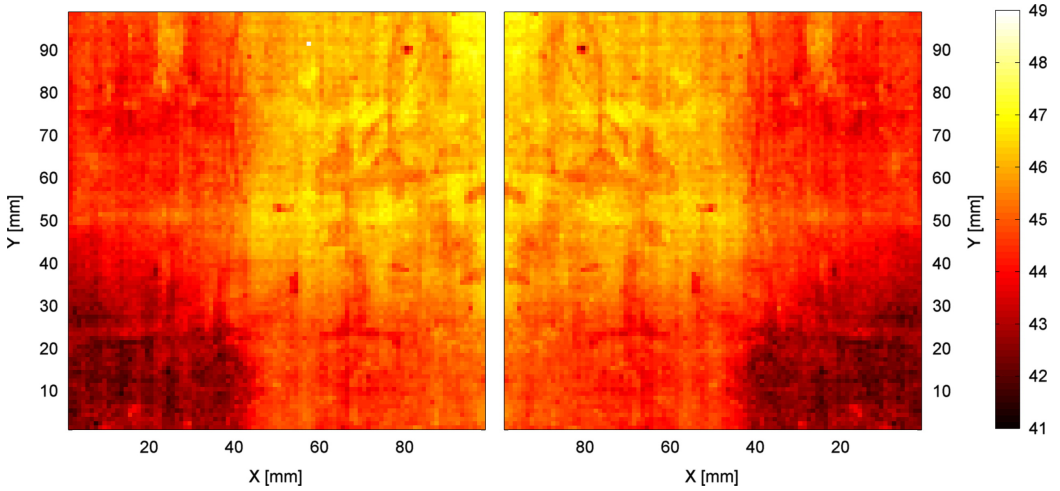

Figure 4.1: Inner hole diameter histograms measured on the top (left) and bottom (right) sides of a GEM foil [60]. Diameters are in µm.

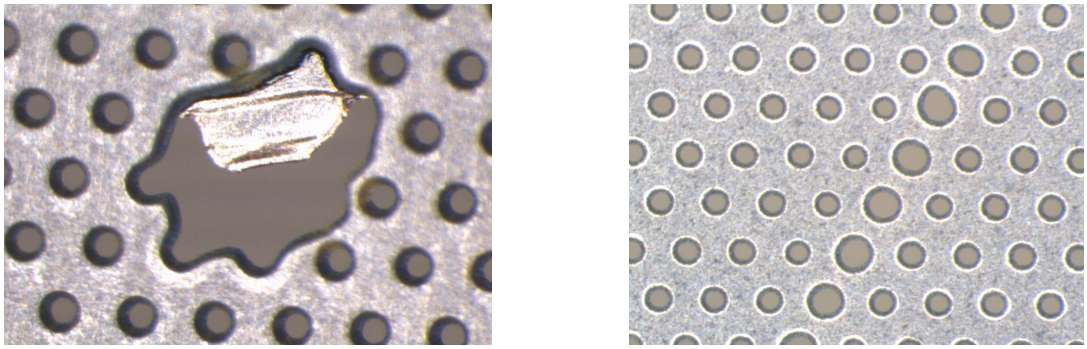

(a) (b)

Figure 4.2: Two typical foil defects. Panel (a) shows an over-etched foil and (b) a row of holes with increased diameter.

4.1.2 GEM preparation

In order to prepare the G10 frames for gluing, a thorough polishing and cleaning in an ultrasonic bath is necessary to remove remaining pieces of fibre and dust. This is of particular importance, as remnants of the frame might reach the GEM area of the foil and thus alter the electric stability.

A constant flatness is assured by stretching the GEM foil with a tension of 10 N/cm by a pneumatic stretching tool (Fig. 4.3a). The epoxy ARALDITE 2011 [61] is dispensed onto the frame on a defined path by a gluing robot (IROC, see Fig. 4.3b) or with a manual dispenser (OROC). It has been found that the quality achieved with a manual dispenser is compatible to the gluing robot.

Alignment of the GEM foil with respect to the frame is provided by an aluminium jig with cut-outs for the frame and additionally by four Teflon alignment pins which are mounted at the four corners of the trapezoid, as shown in Fig. 4.3c. The stretched foil is positioned above the frame, aligned with respect to it and then carefully lowered. An aluminium plate and additional lead bricks mounted on top of the GEM foil serve as a counterweight to properly press the foil onto the frame (see Fig. 4.3d).

After gluing, the remaining polyimide material of the foil is cut off, such that the outlines of the GEM foil match those of the frame and the foil is tested under HV to verify its integrity after gluing. Then, the foil can be equipped with loading resistors.

4.1.3 Detector assembly

The prototypes are assembled on spare readout chambers of the ALICE TPC. The wires planes of the respective chambers are removed and replaced by a stack of four GEMs in the baseline configuration S-LP-LP-S. The procedure described below holds for both the IROC and OROC prototype, if not stated otherwise.

In order to supply all individual GEM foils in the stack with high voltage, a gas-tight connection to the power supply on the outside has to be established. Therefore, nine (twelve) holes are drilled into the alubody of the IROC (OROC). For the connection to the GEM foils, multi-stranded, Kapton-coated wires are chosen, as they provide the required flexibility. Two such wires are soldered together and the junction is covered in epoxy, as this prevents gas leaking through the

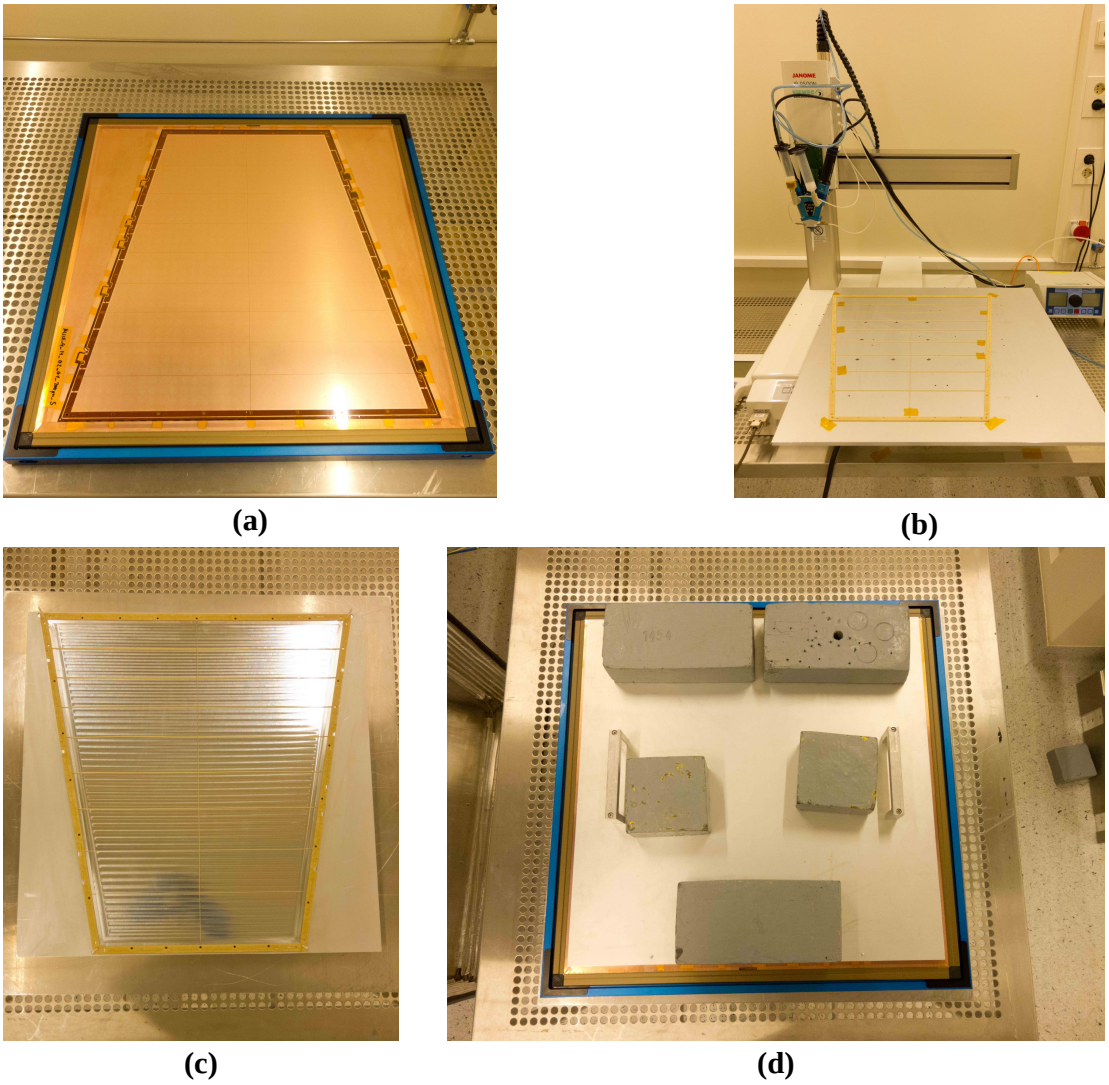

Figure 4.3: GEM gluing procedure. The different steps are described in the text.

interspace between individual wires and thus assures gas tightness. The such prepared connection is glued into the additional feedthroughs of the alubody. Connection from the outside is established via three (nine) dedicated boxes each housing three SHV-connectors for the IROC (OROC), while on the inside, the bare wire is soldered to the respective HV-flap of the GEM foil in the next assembly step.

The assembly of the prototype chamber starts by mounting the lowest GEM. Alignment with respect to the alubody is provided by four alignment pins, that will later on be used to fix the stack. The relevant parts are depicted by the schematic overview shown in Fig. 4.4. A protective polyimide layer is used to cover the active area of the GEM while soldering the HV flap for the top and bottom side respectively to a HV wire from the feed-through. The remaining, non-used flaps are removed. A HV test is conducted to assure the integrity of the foil and the functionality of all electric connections. Then, the remaining foils are sequentially mounted onto the alubody according to this procedure.

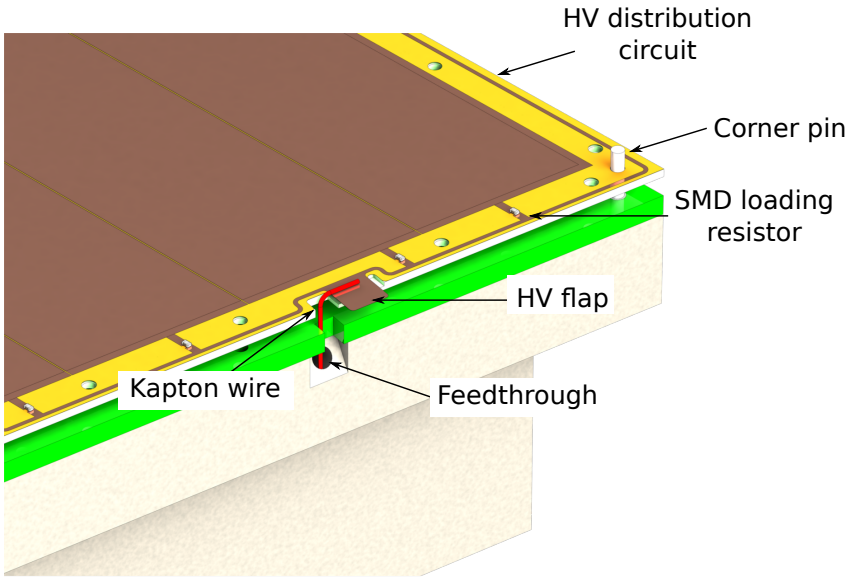

Figure 4.4: Detailed view of the HV distribution on the segmented side of an IROC GEM foil.

The stack is then fixed with glass-fibre reinforced polyimide screws and supplied with operational voltage to assure its functionality and stability.

4.2 Prototype of an Inner Readout Chamber for dE/dx studies

In order to prove the dE/dx performance of a GEM-based detector prototype for the ALICE TPC, a prototype detector of an Inner Read Out Chamber is built and equipped with a stack of four GEM foils in the baseline configuration (S-LP-LP-S).

Figure 4.5 shows an exploded view of the prototype depicting the single parts of the assembly. Additionally, a cover electrode is employed for this prototype in order to prevent distortion of the drift field caused by the inhomogeneous copper clad of the borders of the uppermost GEM (flaps, HV distribution circuit, etc.). The cover electrode is a 1 mm thick PCB covering the whole width of the frame (10 mm) and thus surrounds the active area of the GEM foils. In order to match the nominal drift field of $E_{\mathrm{drift}} = 400\,\mathrm{V}\,/\mathrm{cm}$, the potential applied to the cover electrode is increased by 40 V with respect to the top side of GEM1.

The such prepared chamber is mounted to a test box, displayed in Fig. 4.6, which allows for the application of a drift field. The field is defined by the drift cathode and a rectangular field cage with a size of 57×61 cm^2. The cathode is made of a 50 µm thin aluminized Kapton foil, while the field cage employs 8 field-defining strips with a pitch of 15 mm each, which are interconnected with 1 MΩ resistors. The drift field at the cover electrode is matched by adjusting the potential of the last strip. In order to allow for measurements with beam and radioactive sources, Mylar windows are installed on the walls closest to the parallel sides of the chamber.

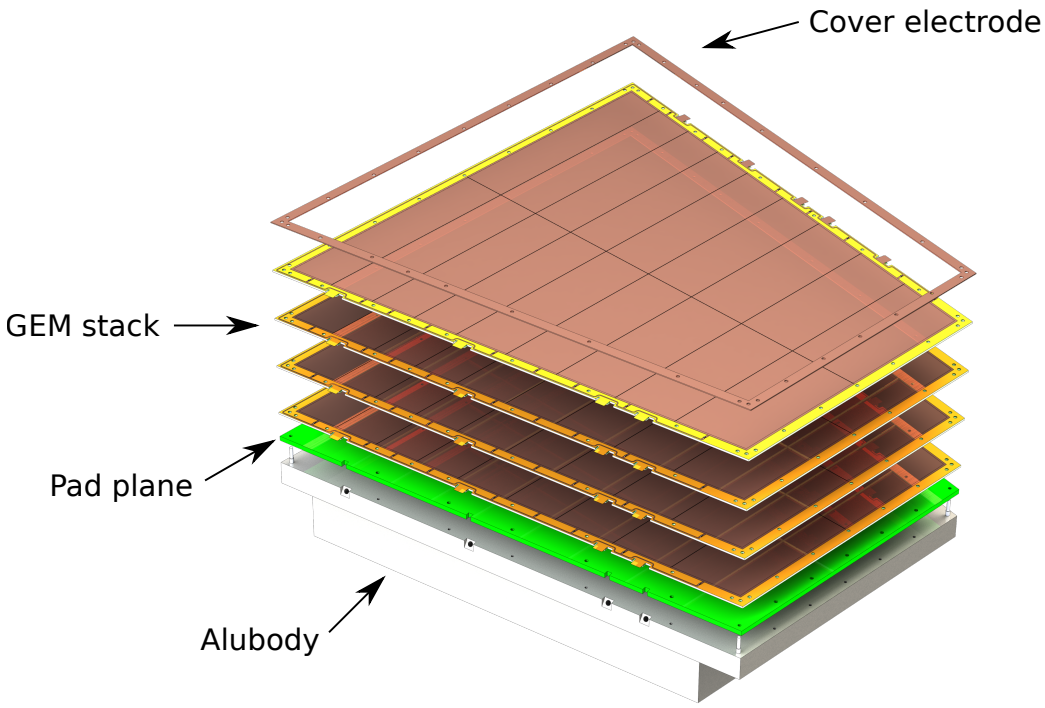

Figure 4.5: Exploded view of the GEM-based ALICE IROC prototype.

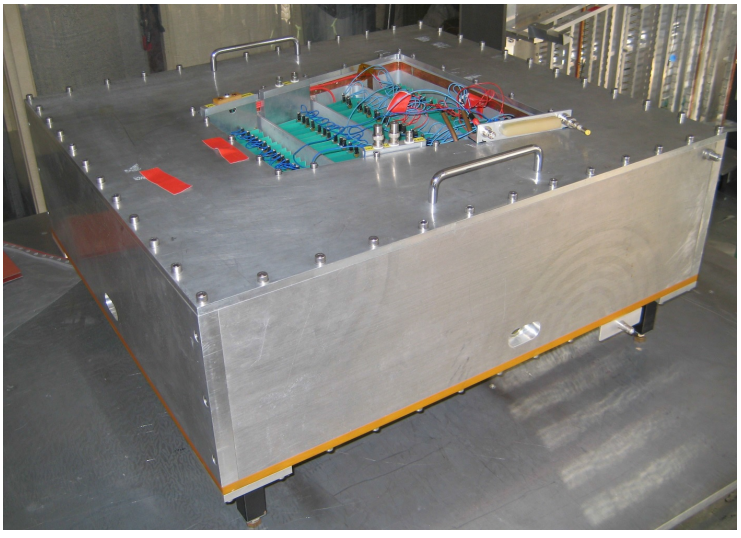

Figure 4.6: Photography of the chamber mounted in the test box.

4.3 Validation of the production methods with a prototype of an Outer Readout Chamber

In order to validate the production methods with an Outer Read Out Chamber, a dedicated hands-on workshop took place at Technische Universität München in March 2015. The goal of this workshop was to gather all eleven institutes involved in the production cycle for the ALICE TPC upgrade to revise and discuss the production protocols established during the prototyping phase, improve them and define the relevant steps for the mass production.

In the course of this workshop, three stacks of four GEMs each corresponding to OROC 1, 2 and 3 are prepared according to the procedure described in Sec. 4.1. Figure 4.7 shows a photography of all three sizes of OROC foils with an IROC foil for comparison.

The assembly of the detector takes place at CERN. The GEMs are mounted on a spare OROC alubody, which is then transferred to a test box similar to that mentioned in the previous section, however with larger overall dimensions. Tests with an ^{55}Fe source are conducted in a Ar-CO_2 (82-18) gas mixture to prove the functionality of the GEM stacks. Figure 4.8 shows a spectrum of a ^{55}Fe source measured with the prototype, which is in fact the largest GEM-based detector built up to date.

The introduction of a spacer grid to the frames is justified by considerations of the electrostatic forces between adjacent foils. As it however drastically increases the overall price of the frames, the spacer grid of all OROC 3 frames was removed in order to prove its necessity. In fact, during commissioning, frequent discharges are observed in this stack above ∼80 % of the nominal high voltage. As this is a clear hint for discharges due to the sag between adjacent foils, the detector is opened, all but the lowest GEMs are removed and sagging tests are conducted with only one GEM above the pad plane.

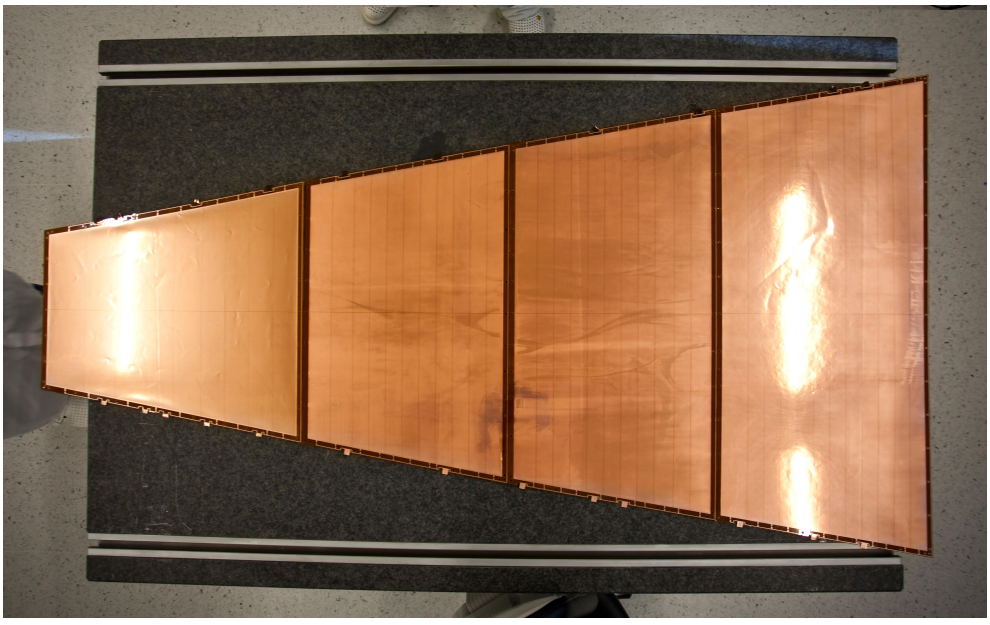

Figure 4.7: Photography of all three sizes of OROC foils with an IROC foil for comparison.

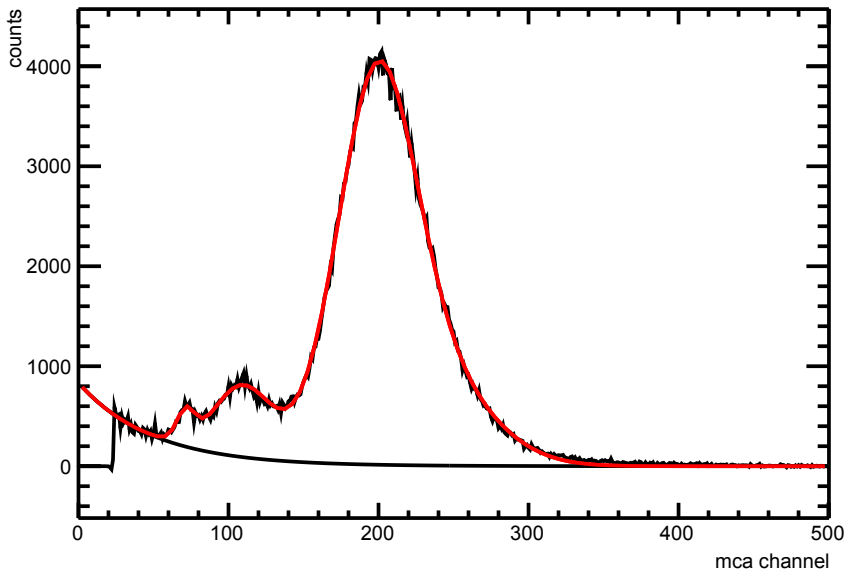

Figure 4.8: Spectrum of a ^{55}Fe source measured with the OROC 2 [62].

The induction field is successively increased, while keeping the potential across the GEM at zero. Above an electric field of ∼3 kV/cm, the foil sag towards the grounded pad plane is visible by eye and frequent discharges can be observed. Quantitative measurements based on the observation of the movement of the reflection of a laser pointed to the middle of the GEM foil are conducted, but yield inconclusive results. A simple approximation of the amplitude of the foil sag can be made by considering the Paschen limit [63], which defines the breakdown limit in a gas as a function of pressure and the distance between the two respective electrodes. With this, considering the applied potential, the distance between the foil and the pad plane is a few tens of µm, which is a clear indication that the spacer grid is a necessary feature of the frames.

In order to define the number of supporting structures introduced, at first only one Teflon bar is placed in parallel to the parallel sides of the trapezoid onto the pad plane. While the foil sag can still be observed, discharges towards the pad plane are already prevented at nominal voltage. With a simple cross placed onto the pad plane, the sag is imperceivable and it is possible to operate the detector stable up to the nominal voltage with a vast safety margin.

It can hence be concluded, that a cross is sufficient to account for the electrostatic attraction of adjacent foils, which constitutes a major input for the design of the frames for the pre-production. A final proof of the functionality with a full stack is yet to be provided.

5 dE/dx resolution studies

The GEM-based IROC prototype is transferred to CERN for commissioning with readout electronics and conducting a study of the dE/dx performance at the CERN Proton Synchrotron (PS). The data is reconstructed and analysed with the AliRoot framework. The readout of a GEM-based detector prototype instead of a MWPC-based readout chamber imposes the necessity to slightly adopt the clustering algorithm employed and to extract a parametrization of the uncertainty on the position measurement of the clusters. As the typical track geometry differs from the typical usage scenario of the ALICE TPC tracking algorithms, a modified approach for finding track seeds as an input for the Kalman filter is employed.

5.1 Setup at CERN PS

5.1.1 The T10 beam line at the Proton Synchrotron

The beam at the PS East Area is a secondary particle beam derived from the initial 24 GeV/c proton beam of the CERN PS. A detailed description of the PS East Area beam lines can be found in [64]. The primary proton beam delivered by PS is impinging on a production target for the secondary beam. The T10 beam line, at which the presented study is conducted, allows for the adjustment of the momentum of the extracted secondary beam ranging from 1 to 7 GeV/c. The beam content strongly depends on the used target and the momentum of the secondary beam. In the case of a negative beam, the electron admixture ranges from about 50 % at 1 GeV/c down to about 10 % at 7 GeV/c compared to the pion portion [64]. For the purpose of this study, a beam containing electrons and negative pions with a momentum of 1 GeV/c is chosen.

The beam line is equipped with several in-beam detectors which provide beam characterization and monitoring. At the end of the beam line, a threshold Cherenkov Counter is mounted, which serves as a reference detector for particle identification in the course of this work. It is a cylindrical vessel filled with nitrogen at atmospheric pressure and equipped with a UV-sensitive photomultiplier tube, which detects the Cherenkov photons produced by traversing particles. Two Multi-Wire Proportional Chambers provide a measurement of the beam profile, size and position. For triggering and beam definition, a set of two scintillators is mounted at the exit window of the beamline. The trigger requires a coincidence of both modules.

Figure 5.1 shows a photography of the experimental setup.

5.1.2 HV scheme

The GEM stack is powered via a passive resistor chain, which sequentially degrades the potential for the respective GEM electrodes. The resistor chain is schematically depicted in Fig. 5.2 for the specific case of one of the HV settings summarized in Tab. 3.1. This powering scheme is motivated

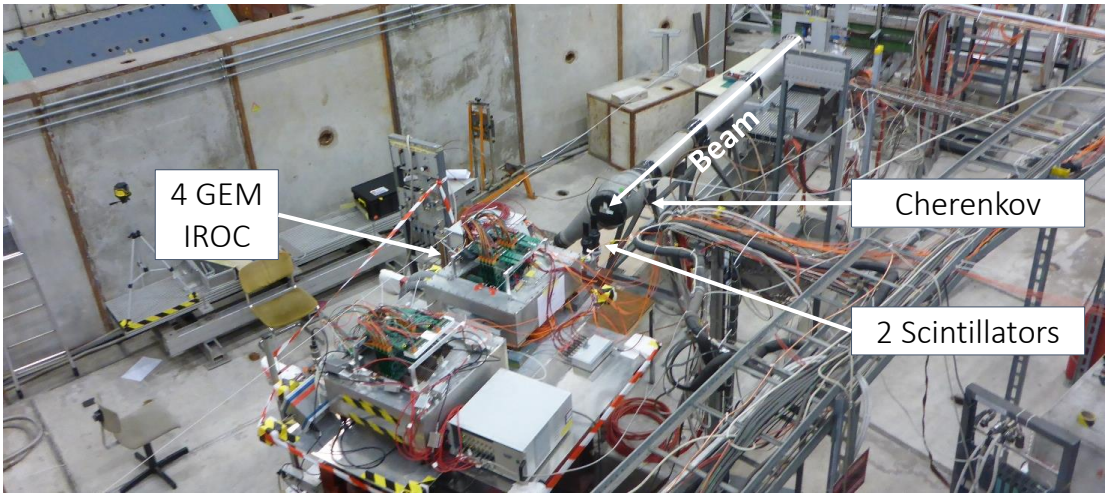

Figure 5.1: IROC prototype and additional detectors installed in the PS East Area experimental hall (T10 beam line).

by its transient behaviour, as a potential discharge in one of the GEM electrodes immediately affects all potentials applied to the stack. Therefore, in case of a *trip* of the power supply, where the current drawn by a discharge exceeds the current limit set by the user, a constant potential difference between all electrodes is assured. In contrast to this, in case of a trip with an individual powering of each electrodes, the potential of the top electrode may decrease slower in comparison to the bottom. This would result in an increase of the potential difference between the electrodes, which might possibly lead to breakdown and in severe cases even cause damage of the foil [65].

The resistor chain, the cover electrode and the last strip of the field cage is powered by a ISEG EHS 8060n 8-channel 6 kV power supply, while the cathode voltage is applied independently by an ISEG HPn300 30 kV module. Due to a malfunctioning of the power supply, the potential applied to the cover electrode does not match exactly the drift field. Therefore, the latter is distorted in the first and last few pad rows.

A set of different HV settings is tested throughout the beam campaign at PS. All runs with the corresponding HV settings are summarized in Appendix A.

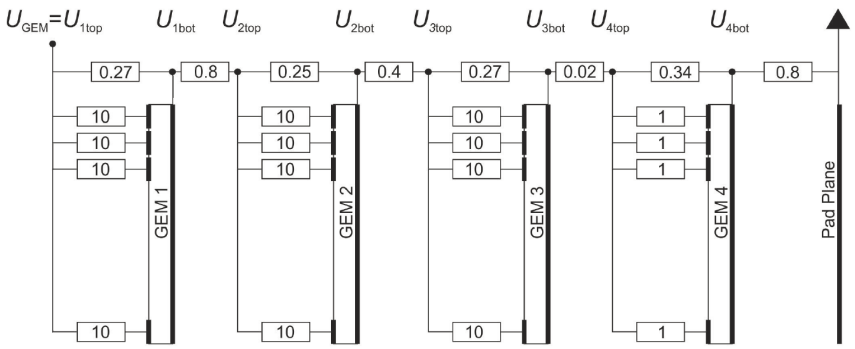

Figure 5.2: Schematics of the HV distribution scheme for a GEM detector module. The resistor values are given in MΩ. Figure modified from [24].

5.1.3 Readout

The IROC GEM prototype is equipped with 10 EUDET front-end cards (FEC), which were borrowed from the LCTPC (Linear Collider TPC) collaboration. This allows for the readout of about 1200 channels, covering a 6-7 cm wide corridor over the whole length of the chamber. The FECs are based on the PCA16 [66]/ ALTRO chips [67]. The ALTRO chip was originally designed for the ALICE experiment. However, as GEMs provide, in contrast to MWPCs, a negative input polarity to the FEC, a different preamplifier needs to be employed - the PCA16, specifically designed for Micro-Pattern Gas Detectors. The sampling frequency is set to 20 MHz at a peaking time of 120 ns and a conversion gain of 12 mV/fC.

Due to the very large volume of the raw data, the TPC requires a zero suppression of the data already on the level of the front-end electronics. Therefore, the exact value of the electronic baseline (*pedestal*) has to be known for each individual electronic channel. The zero suppression threshold can then be determined as the pedestal value with a multiple of the width of the baseline distribution to account for fluctuations caused by electronic noise.

In order to measure both values, so-called *pedestal* runs are taken, where the baseline of the electronics is recorded without any zero suppression and without presence of the beam, while the GEM stack is fully powered. As the shape of the pedestal distribution is well described by a Gaussian, its mean and RMS can be extracted for each pad individually by fitting a Gaussian function. The resulting two-dimensional distributions are shown in Fig. 5.3a for the mean of the pedestal and in Fig. 5.3b for its width σ. The pedestal value is typically around 100 ADC channels, while only very few outliers can be observed. The noise is in the largest part of the readout area well below 1 ADC channel, while some pads with about twice the noise level can be found towards the upper boundary. With approximately 1000 electrons per ADC channel, the noise can hence be determined to about 600 electrons. Accordingly, a zero suppression threshold of 2 ADC counts is chosen, which corresponds to around 2000 electrons.

The similarity of the FECs to the ALICE FECs allows for the usage of the current TPC readout system [38]: The data are read out via the backplane with two Readout Control Units (RCU) and transferred via optical links to a Local Data Concentrator PC, which runs the ALICE data acquisition system DATE [38]. The data from the two scintillators, the Cherenkov counter and a

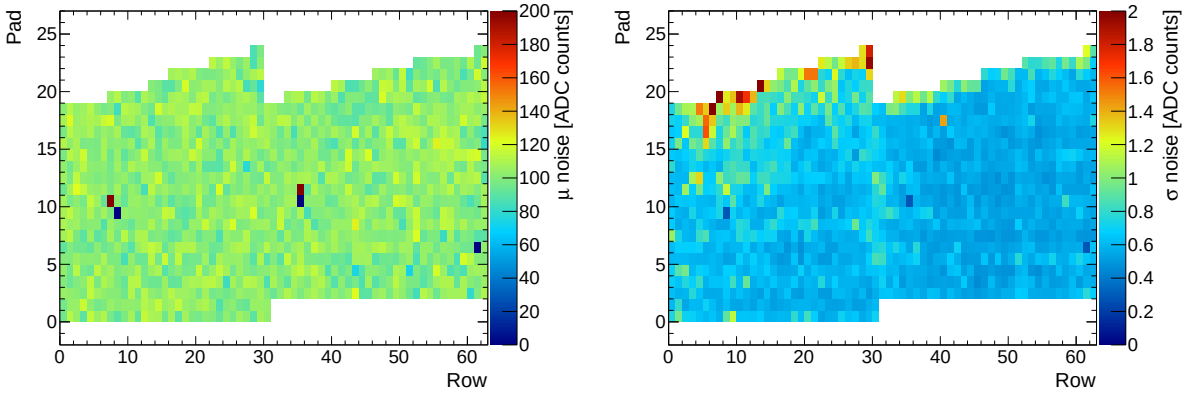

Figure 5.3: Mean (a) and σ (b) of the pedestal distribution as a function of the pad position.

sensor monitoring the ambient conditions are read out via the CAMAC system. The two data streams are synchronized based on an event tag.

The average DAQ rate is ∼300 events/spill with a spill length of 0.5 s, whereas the beam rate is of the order of 2000 particles/spill.

5.2 Reconstruction

The front-end cards on the detector provide a digitized measurement of the amplitude on each pad at a certain time - a so-called *digit*. In order to reconstruct the track of a particle which traversed the detector from a set of digits, several reconstruction steps have to be performed. The work flow used for the reconstruction, depicted in Fig. 5.4, is described in this section.

In parallel to this analysis, the dE/dx resolution of the prototype was extracted employing a simple clustering and tracking algorithm. This analysis will be referred to as *TDR analysis* in the following, as these results were published in the scope of the Technical Design Report of the ALICE TPC upgrade [25].

5.2.1 Cluster finding

The first step consists of merging consecutive digits into a so-called *cluster*. Figure 5.5a shows the digits belonging to a typical event as recorded during the testbeam.

The cluster finder starts by filling the digits sequentially into a pad-time matrix for each consecutive pad row and looking for amplitude maxima. A cluster is then created by investigating the amplitudes $A_{i,j}$ stored in a 5×5 matrix with the maximum at its center, where the pad hits are denoted by i, whereas time bin hits are denoted by j. The region covered by the pad-time matrix is larger than the typical size of a cluster with a width of $\sigma \sim 0.75$ bins in both directions for a MWPC [9]. For a GEM-based readout, due to the very narrow pad response function, the cluster is supposed to spread over fewer pads. Due to the enhanced sampling rate during the testbeam with respect to ALICE, the charge of such a cluster is distributed into more time bins, which is clearly visible in Fig. 5.6, where a typical 5×5 matrix for a GEM-based readout is shown.

The maximal charge of the cluster $Q_{\mathrm{max}} = A_{0,0}$ is given by the amplitude measured in the center of the matrix. For the computation of the total charge Q_{tot}, at first the bins adjacent to the central bin are investigated and the corresponding charge $A_{i,j}$ is summed up, i.e.

$$Q_{\mathrm{tot}} = \sum_{i=-1}^{1} \sum_{j=-1}^{1} A_{i,j}. \tag{5.1}$$

The charge of the outer bins, where $|i| = 2$ or $|j| = 2$, is only added to Q_{tot}, if the neighbouring inner bin contains charge above threshold in order to reduce the contribution of electronic noise to the signal. As the expected shape of a cluster differs for different amplification systems, the corresponding cuts applied during this procedure have to be modified in order to match the expected signal created by an electron cloud amplified in a stack of four GEMs and also for the sake of consistency with the TDR analysis.

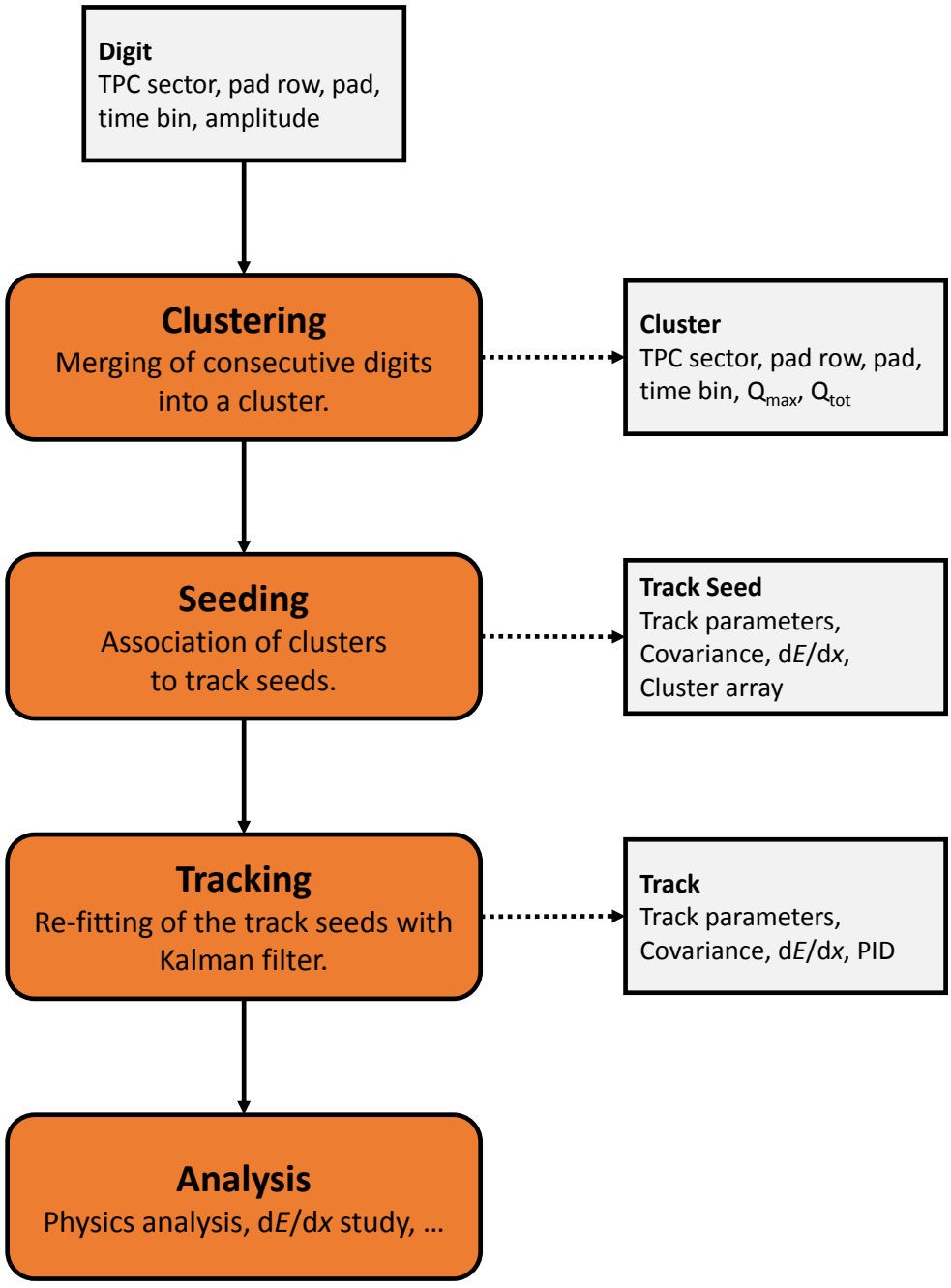

Figure 5.4: Schematic overview of the work flow of the reconstruction algorithm. The orange boxes represent the respective reconstruction steps as described in this Section, while the grey boxes correspond to the resulting objects and the most important information they contain.

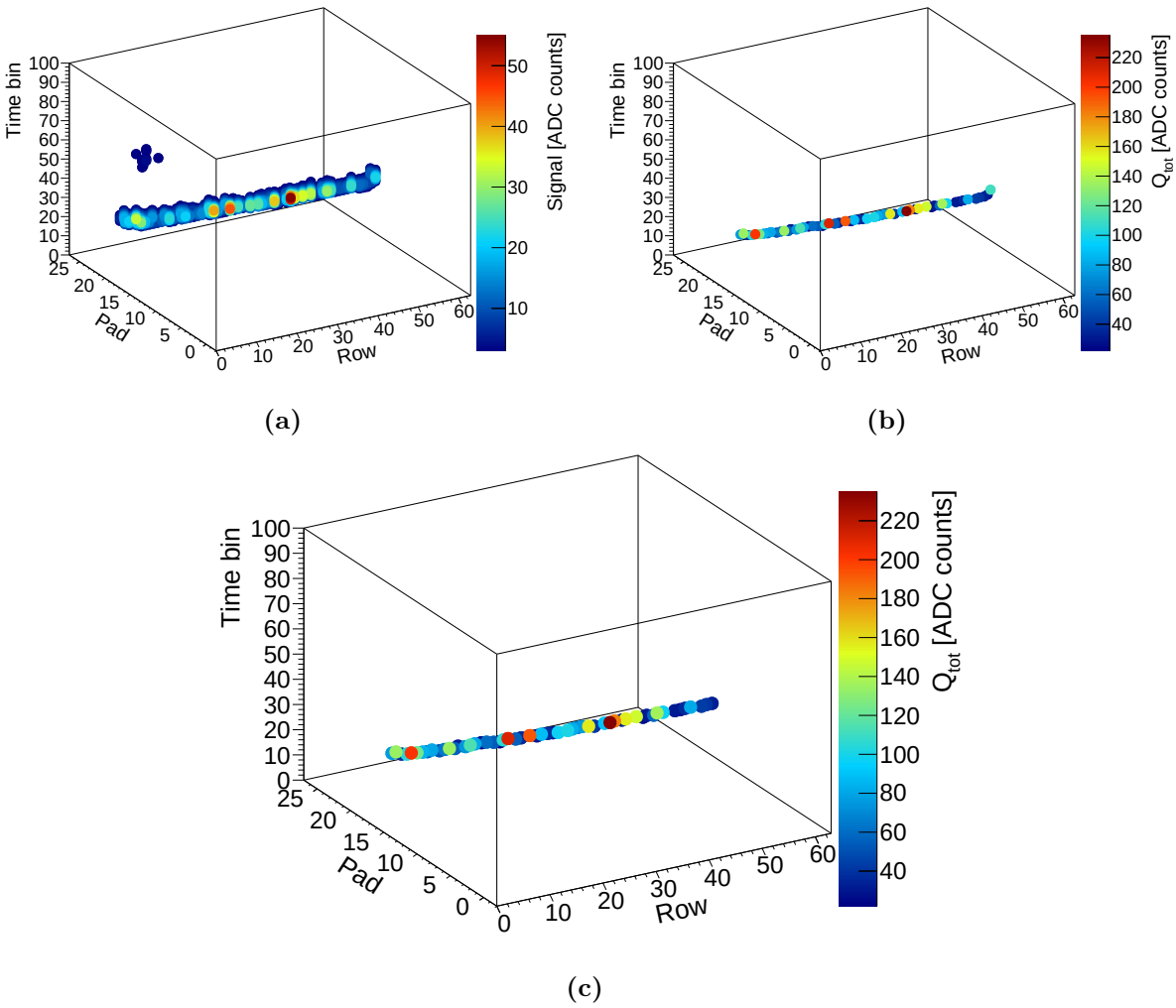

Figure 5.5: The digits recorded by the front-end electronics are shown in panel (a). The resulting clusters are displayed in panel (b), while (c) depicts the clusters assigned to the reconstructed track.

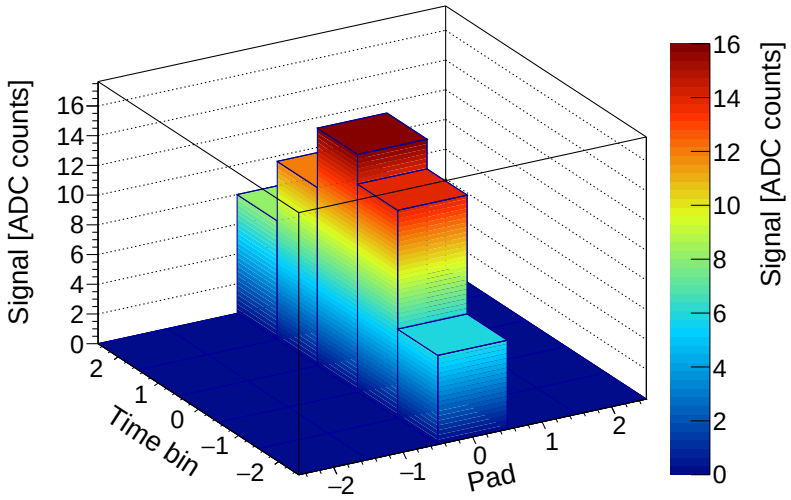

Figure 5.6: Exemplary 5×5 matrix investigated during cluster finding.

The cluster position is defined by the *centre of gravity* (COG), in case the cluster spreads over several pad or time bins, and calculated as follows,

$$y_{\text{pad, COG}} = \frac{\sum_{i=-2}^{2}\sum_{j=-2}^{2} i \cdot A_{i,j}}{Q_{\text{tot}}}, \qquad z_{\text{pad, COG}} = \frac{\sum_{i=-2}^{2}\sum_{j=-2}^{2} j \cdot A_{i,j}}{Q_{\text{tot}}}. \tag{5.2}$$

In case the charge of the cluster is contained in one pad or time bin, the position is interpreted as the center of the respective bin. The x-position of the cluster is considered as the crossing point of the track with the center of the corresponding pad row.

However, threshold effects can distort the COG, as charge below threshold will obviously not be taken into account in the calculation. In order to circumvent this, signals below threshold are replaced by the expected value according to a parametrized interpolation. This procedure yields results comparable with a Gaussian fit, but is much faster [9]. As the parametrization is very sensitive to the PRF and has furthermore been optimized for the readout of a MWPC, this procedure is not used in the course of this study. The result of the clustering algorithm applied to the digits shown in Fig. 5.5a is depicted in Fig. 5.5b.

5.2.1.1 Cluster position uncertainty

In order to fit a track to a set of points, the consideration of the respective uncertainties obviously improves the quality of the fit. The position uncertainty of the cluster position is dominated by the charge spread due to diffusion of the ionization electrons and the projection of a three-dimensional object (a cluster) onto a two-dimensional pad plane.

Due to the very narrow pad response function in a GEM-based readout structure, the signal is almost exclusively induced on pads directly below the ionization electrons. For very short drift distances, the impact of diffusion is negligible and thus it is very probable, that the signal is induced only on one pad. In such cases, the uncertainty on the position of the cluster is given by statistical considerations and can be calculated as $d_{\text{pad}}/\sqrt{12}$, where d_{pad} denotes the width of the pad.

For larger drift distances, the size of the cluster increases due to the impact of diffusion and hence, the charge is collected on several pads and the COG gives a reliable estimate of the position. This is reflected in a decrease of the uncertainty on the position measurement. With increasing drift length however, this effect is reversed, as the charge is spread by diffusion such, that the charge distribution measured on the pad plane becomes flat over several pads. Consequently, the mean position is no longer well defined. Additionally, charge in the tails of the cluster may fall below the threshold of the readout electronics and is thus no longer considered for the computation of the COG. Therefore, the uncertainty on the position measurement of the cluster increases.

Analogous considerations can be made for the uncertainty of the cluster position along the drift direction, apart from the fact that the typical cluster size is larger in z. Accordingly, the uncertainty on the corresponding position measurement is expected to be smaller. Moreover, as clusters contained in only one time bin have not been found, the initial decrease of the uncertainty is not anticipated.

As the charge is measured by projecting the track onto the pad plane, the length of the projected track segment depends on the respective inclination angle α and β, where α is defined as the

angle between the projection of the track onto the pad plane and the pad row and β as the angle between the track and the global z-axis. In combination with the discrete, rectangular size of the respective bins, a larger inclination angle increases the number of measurement points and thus alters, analogous to the considerations above, the uncertainty on the position measurement.

As any information about the track itself is not available during clustering, the uncertainties on the position measurement are approximated by a simple estimation of the cluster width,

$$\sigma^2_{y_{\mathrm{COG}}} = \frac{\sum_{i=-2}^{2}\sum_{j=-2}^{2} i^2 \cdot A_{i,j}}{Q_{\mathrm{tot}}} - y^2_{\mathrm{pad,\ COG}}, \tag{5.3}$$

$$\sigma^2_{z_{\mathrm{COG}}} = \frac{\sum_{i=-2}^{2}\sum_{j=-2}^{2} j^2 \cdot A_{i,j}}{Q_{\mathrm{tot}}} - z^2_{\mathrm{pad,\ COG}}. \tag{5.4}$$

The proper cluster position uncertainties are then assigned during the tracking procedure. To this end, the cluster uncertainty is parametrized according to the following formulae

$$\sigma^2_{y_{\mathrm{COG}}} = \frac{D^2_{\mathrm{T}} \cdot L_{\mathrm{drift}}}{A} \cdot \frac{G_g(A)}{k_{\mathrm{ch}}} + \frac{\tan^2(\beta) \cdot L^2_{\mathrm{pad}}}{12A} \cdot \frac{G_{\mathrm{secondary}}(A)}{k_{\mathrm{prim}}} + \sigma^2_{\mathrm{noise}}, \tag{5.5}$$

$$\sigma^2_{z_{\mathrm{COG}}} = \frac{D^2_{\mathrm{L}} \cdot L_{\mathrm{drift}}}{A} \cdot \frac{G_g(A)}{k_{\mathrm{ch}}} + \frac{\tan^2(\alpha) \cdot L^2_{\mathrm{pad}}}{12A} \cdot \frac{G_{\mathrm{secondary}}(A)}{k_{\mathrm{prim}}} + \sigma^2_{\mathrm{noise}}. \tag{5.6}$$

The first term describes the impact of diffusion. D_{L} and D_{T} are the longitudinal and transverse diffusion coefficients, L_{drift} is the drift length, A the charge of the cluster and $G_g(A)$ a factor representing fluctuations of the gas gain. The second term stems from the projection, where L_{pad} is the pad length, α and β the respective track inclination angles and $G_{\mathrm{secondary}}$ describes fluctuations of the secondary ionization. The last term reflects the noise of the read-out electronics. The k_{ch} and k_{prim} are free parameters [68].

The standard cluster uncertainties provided by AliRoot have been measured for a MWPC-based readout. It is therefore mandatory to extract a proper parametrization of the uncertainties for a GEM-based readout not to introduce any bias due to the different pad response functions. In order to do so, a dedicated task is set up.

Measurement of the position uncertainties of the clusters

The uncertainties on the cluster position in y and z is considered in the following as the width σ of the respective residual distributions. The track residuals are defined as the distance between each cluster and the crossing point of the track fit with the corresponding pad row. For incorporating the angular and z dependencies, the residuals are investigated as a function of the these variables. One bin clusters are excluded, as their uncertainty is given by $d/\sqrt{12}$, where d denotes the width of the pad or time bin, respectively. During tracking, the uncertainty of such clusters is manually set to the appropriate value. Moreover, pad rows which are known to be affected by gain variations (see Sec. 5.2.5) or distortions of the drift field are excluded from the procedure.

The respective track residuals are fitted with a Gaussian function and the width σ of the distribution is extracted for each slice in z and the respective angle. The resulting cluster uncertainty for y shown in Fig. 5.7a and for z in Fig. 5.7b as a function of the drift length z and the corresponding inclination angle. In general, there is only little dependence in the drift length and the respective inclination angles.

The cluster uncertainty in y decreases with increasing drift length z, as the charge in the cluster is spread by diffusion and hence the COG method returns a more reliable estimate of the position. Also a slight increase with the inclination angle α can be observed, which is caused by the flattening of the charge distribution over several pads. The ridge with larger uncertainties around $\tan\alpha \sim 0.075$ is solely due to reduced statistics and the correspondingly reduced quality of the Gaussian fits.

As expected, due to the enhanced cluster size in drift direction, the corresponding uncertainty is in general smaller than that along the pad row. Moreover, the uncertainty on the position measurement increases with increasing drift length, as anticipated above. The same holds for the dependence on the inclination angle β.

In order to extract a parametrization of the uncertainty, the corresponding distributions are fitted with a surface,

$$\sigma^2_{y_{\mathrm{COG}}} = k_{0,y} + k_{1,y} \cdot \tan^2(\alpha) + k_{2,y} \cdot L^2_{\mathrm{drift}} + k_{3,y} \cdot \tan^4(\alpha) + k_{4,y} \cdot L_{\mathrm{drift}} \cdot \tan^2(\alpha), \tag{5.7}$$

$$\sigma^2_{z_{\mathrm{COG}}} = k_{0,z} + k_{1,z} \cdot \tan^2(\beta) + k_{2,z} \cdot L^2_{\mathrm{drift}} + k_{3,z} \cdot \tan^4(\beta) + k_{4,z} \cdot L_{\mathrm{drift}} \cdot \tan^2(\beta). \tag{5.8}$$

The parameters k are then the representation of the respective uncertainties on the position of the cluster, where k_0 reflects the electronic noise in Eqs. 5.5 and 5.6, k_1 incorporates the effect

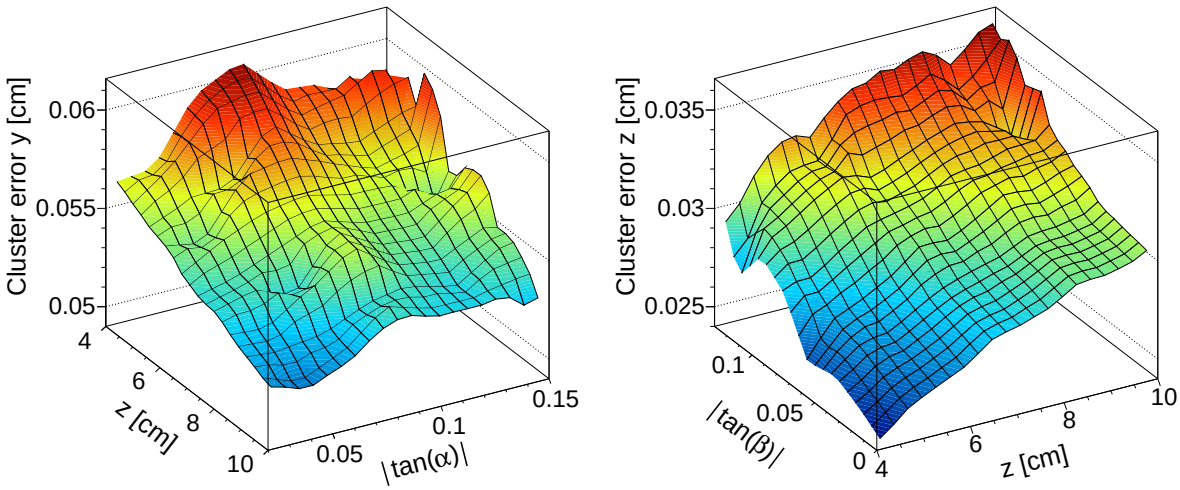

(a) **(b)**

Figure 5.7: Cluster uncertainty in y (a) and z (a) as a function of drift length and corresponding inclination angle. Note that b) has been turned by 90° with respect to a) for a better visibility.

of diffusion and k_2 the angular effect. The terms containing k_3 and k_4 represent higher order corrections [68].

These parameters are extracted for each HV-setting and gain separately. It should be noted though, that the track residuals are initially biased, as the track fit takes into account the wrong parametrization of the uncertainty of the MWPC. However, already one iteration of the above mentioned procedure is sufficient for the parametrization of the uncertainty to converge.

5.2.2 Track finding

The precise knowledge of a track is crucial in order to determine e.g. the particle's momentum. Therefore, it is of particular importance to precisely reconstruct the trajectory of the particle passing through the detector. However, so far only a set of clusters has been reconstructed and it is initially not clear, which cluster belongs to which track. Moreover, noise-afflicted or displaced clusters as well as the precision of the space points itself and the corresponding uncertainties affect the measurement. In high energy physics, the *Kalman filter* [69, 70] has proven to fulfil the specific requirements and is nowadays a commonly used tool for tracking purposes, as effects such as multiple scattering and energy loss of the incident particle can be handled much easier than by global fit methods.

The Kalman filter can be applied to a set of noise affected measurements and is able to estimate iteratively the trajectory of e.g. a charged particle passing through the detector. With each iteration, more and more clusters are added to the track according to the prediction of the previous iteration and hence the overall description of the trajectory improves. One of the shortcomings is, however, that a good approximation, a so-called *seed*, has to be at hand before the iterative process can be started.

A track is then defined as a set of five parameters of the particle's trajectory with the corresponding covariance matrix. The y and z coordinates of the intersection point of a track at a given pad row are defined as

$$y(x) = y_0 - \frac{1}{C} \cdot \sqrt{1 - (Cx - \eta)^2}, \qquad z(x) = z_0 - \frac{\tan\lambda}{C} \arcsin(Cx - \eta), \tag{5.9}$$

where $\eta \equiv Cx_0$, C represents the curvature of the projection of the track onto the pad plane and λ is the dip angle between track and pad plane. The coordinates of the centre of the curvature of the track projection onto the pad plane are given by (y_0, z_0). The track state vector x^T is then chosen as

$$x^T = (y, z, C, \tan\lambda, \eta), \tag{5.10}$$

such that only two of the five components (the local track position y and z) change as the track is propagated from one pad row to the next one.

5.2.2.1 Track seeding

As the TPC provides the largest number of space point measurements along a track in the ALICE detector, maximally 159, it is a natural choice to start the global track seeding there. In order to assure a maximal track finding efficiency with respect to both primary and secondary tracks, two

different approaches are employed: seeding with and without vertex constraint. The position of the primary vertex is reconstructed independently with the ITS.

Both seeding approaches start in the outermost pad row of the OROC, where the track density is supposed to be lowest. The algorithm looks for a pair of clusters in pad row i and j, with j being closer to the interaction point (typical values for $i - j$ range between 7 and 20, depending on the approach).

Seeding with vertex constraint
A helix is fitted to this pair of clusters and a first estimate of the primary vertex is computed. The occurrence of a further cluster in the middle pad row $k = (i - j)/2 + j$ is checked and, if found, the parameters of the helix are used as an input for the Kalman filter. The filtering starts then from the outer pad row i towards the inner pad row j. The seed is saved, if in more than half of the crossed pad rows a cluster can be assigned to the track. The procedure is illustrated in Fig. 5.8a.

With the vertex constraint however, it is impossible to find tracks stemming from secondary vertices. Therefore, two different algorithms have been implemented.

Seeding without vertex constraint
A first algorithm is scanning all clusters in the middle pad row k and looks for neighbouring clusters in the adjacent pad rows $k + 1$ and $k - 1$. A straight line is fitted to these three points and elongated to pad rows $k + 2$ and $k - 2$, where again the two closest clusters are looked for and, if found, assigned to the seed. The algorithm continues until pad rows i and j are reached, however the linear fit is replaced by a polynomial after seven clusters have been assigned to the track candidate. If more than half of the pad rows crossed by the algorithm contain a cluster that can be assigned to the track, the seed is saved. The procedure is schematically depicted in Fig. 5.8b.

As the efficiency of this algorithm obviously decreases for low-p_{T} tracks [9], a second algorithm is employed. Again a cluster is found in the middle pad row k, which is closest to a straight line between the pair of clusters in pad rows i and j. The triplet of clusters is then fitted with a helix and a Kalman filter is employed. If at least half of the possible clusters are successfully associated with the track candidate, it is saved as a seed. The procedure is summarized in Fig. 5.8c.

Overall seeding procedure
The overall seeding procedure is then a combination of the above mentioned procedures. At first, several passes of the seeding with vertex constraint with different cuts respectively are carried out at different radii of the TPC. In order to find secondaries, several seeding attempts without vertex constraint are performed. The combination of these two approaches has proven to be most efficient in terms of computing resources and finding track seeds for both primary and secondary tracks. The quality of the seeds is judged according to the reduced χ^2 and the ratio of the number of assigned clusters and the number of crossed pad rows. Clusters belonging to a seed, which is classified as good according to these criteria, cannot be used for further seeding attempts, can however still be assigned to other tracks in the next step.

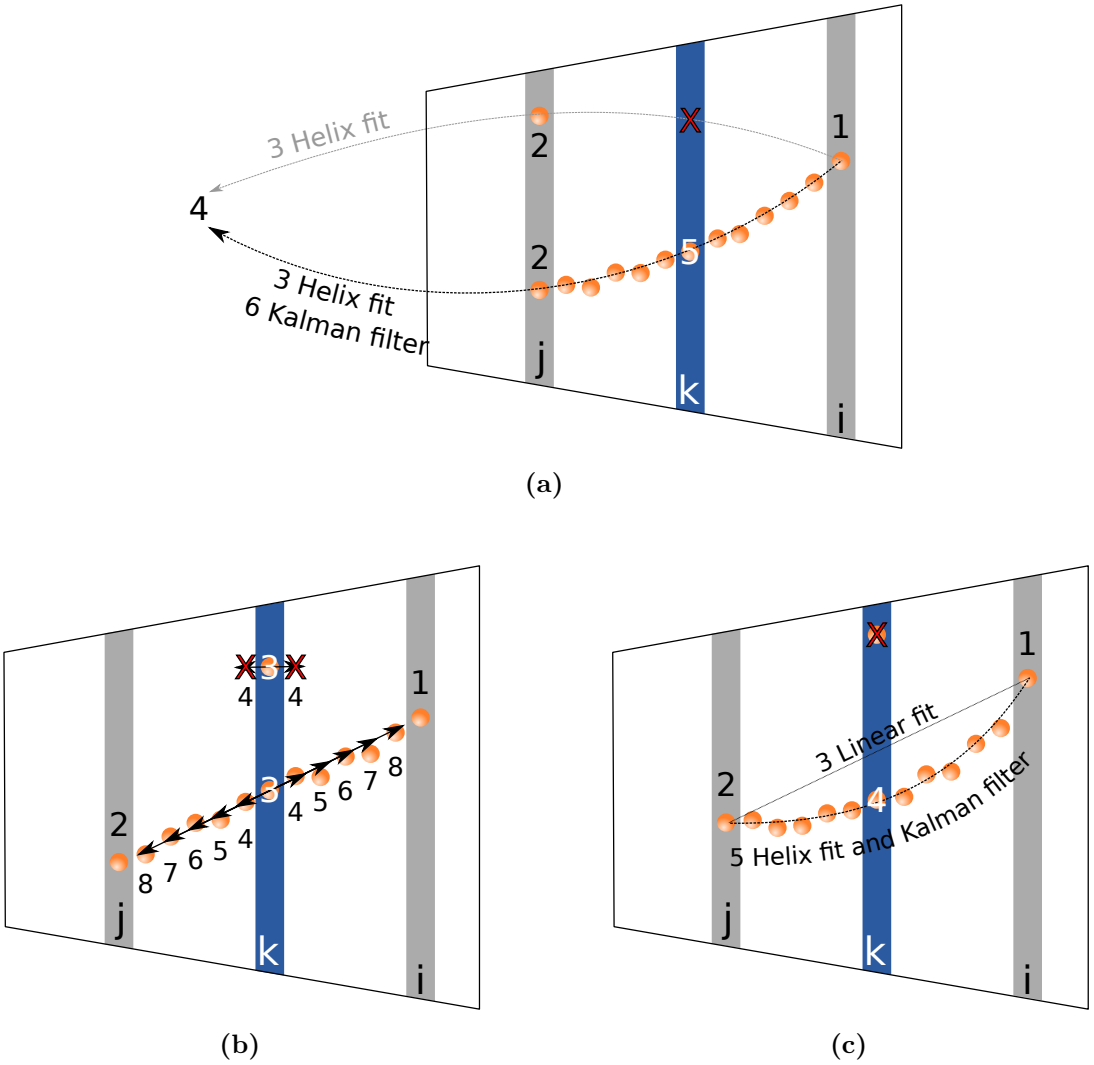

Figure 5.8: Seeding procedure with (a) and without (b) and (c) vertex constraint. For further details see text.

5.2.2.2 Track following

With the track seeds at hand, the Kalman filtering can be applied. As the seeding procedure, also the Kalman filter starts from the outermost pad row of the TPC, where the track density is lowest. Each seed is followed to the innermost pad row or until no further prolongation is possible. At each step, the track parameters are updated by considering the information provided by the nearest cluster. If more than 20 clusters are assigned to the track candidate and more than half of the pad rows crossed by the track contain a cluster that can be assigned to the track candidate, the track is accepted.

Due to the random nature of the seeding procedure, it is possible that a track can be seeded many times at different radii of the TPC. In order to avoid double-counting, the ratio of clusters shared between two track candidates and the total number of clusters is monitored. If the ratio is above a certain threshold, the track candidate with worse quality criteria is removed.

The efficiency of the overall tracking procedure in the TPC, obtained with simulation, is shown in Fig. 5.9. The tracking efficiency is defined as the ratio of the reconstructed tracks and the primary particles in the simulation. Energy loss in the detector material causes the efficiency to drop for $p_{\mathrm{T}} \lesssim 0.5\,\mathrm{GeV}/c$, while the overall efficiency is almost independent of the occupancy in the detector [5].

The clusters belonging to a track fitted to the clusters depicted in Fig. 5.5b are shown in Fig. 5.5c.

5.2.3 Overall ALICE tracking

For the sake of completeness, also the overall tracking approach of ALICE shall be mentioned. A more detailed description can be found in [71]. In parallel to the TPC clustering, a cluster finding is employed in all central detectors of ALICE. A preliminary interaction vertex is found with the ITS, which further-on constrains the seeding in the TPC. The global tracking then starts with the local TPC tracking in the outermost TPC pad row and proceeds towards smaller radii as described above. Once the innermost row of the TPC is reached, the tracks are continued by the ITS tracking to the primary vertex. By assigning additional ITS clusters to the track, the precision of the track parameters is further improved. For so far unused ITS clusters, a dedicated stand-alone tracking procedure is applied, which recovers tracks that were either not within the acceptance of the TPC or simply not found by the algorithm.

The tracking is then restarted from the primary vertex back to the outer layer of the ITS and then further towards the outermost pad row in the TPC. Now, the track parameters are precise enough to allow for an extrapolation to the outer detectors. In a last step, all tracks are refitted backwards to the primary vertex (for secondary tracks to the corresponding secondary vertex). The overall procedure is schematically summarized in Fig. 5.10.

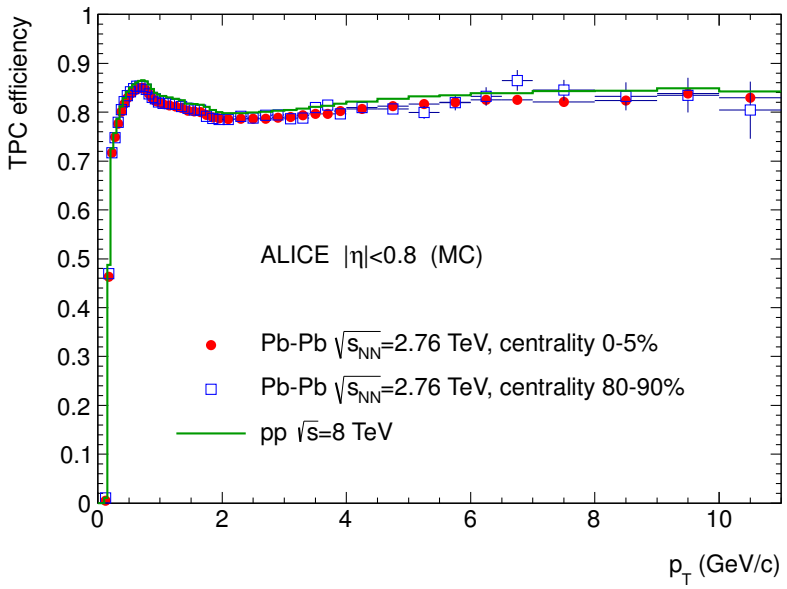

Figure 5.9: TPC track finding efficiency for primary particles in pp and Pb–Pb collisions (simulation) [5].

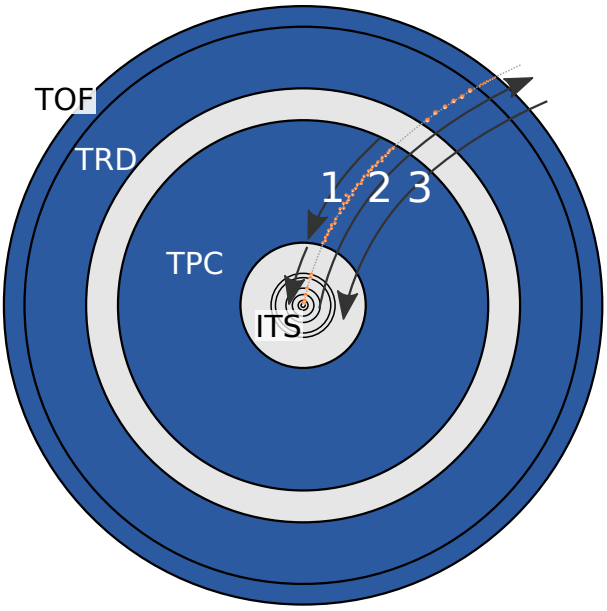

Figure 5.10: Schematic illustration of the global tracking procedure in ALICE. The global tracking starts in the TPC and is continued in the ITS (1). The tracking procedure is then re-started from the primary vertex towards the TPC and the outer detectors (2). In a last step, all tracks are refitted backwards (3).

5.2.4 Adoption of the reconstruction procedure for usage with tracks from the testbeam

The usage scenario of the tracking algorithms for the ALICE TPC is quite different than the requirements imposed by the specific geometry of the typical events recorded during the testbeam. A typical event recorded at PS is characterized by only a few straight tracks that traverse the chamber almost parallel to the pad plane with a drift length of maximally 11.5 cm. Such tracks are discarded by the ALICE tracking algorithms, as they by far do not correspond to the anticipated track geometry. The corresponding angular cuts are hence modified. Moreover, the lack of information about the primary vertex imposes the necessity to change the seeding strategy. The natural solution is to rely only on seed finding procedures without any vertex constraint. For increasing the computing efficiency, the seeding procedure is started at the outermost pad row of the IROC.

The number of clusters assigned to a track is used as a quality criteria throughout the whole tracking procedure. As only an IROC prototype is employed, the number of available pad rows is decreased from 159 to 63. Accordingly, the number of clusters per track is reduced and therefore, the corresponding quality criteria have to be adopted.

Due to the short drift length and the correspondingly negligible diffusion, the charge deposit is mainly limited to one pad per pad row. As such cluster sizes are not expected for a MWPC-based readout, the corresponding cuts have to be adopted. As all calibration and alignment procedures only hold for the fully equipped TPC, none of these algorithms are used.

5.2.5 Corrections

5.2.5.1 Gain correction

Geometric imperfections of the GEM system as well as channel-by-channel variations of the front-end electronics may cause local variations of the gain. In order to minimize the impact of such variations, the normalized pad gain is extracted for each pad individually. The extraction of the gain map is done by computing for each track the truncated energy loss $\langle \mathrm{d}E/\mathrm{d}x \rangle_{\mathrm{tr}}$ and monitoring on each pad the normalized cluster charge $Q_{\mathrm{tot}}/\langle \mathrm{d}E/\mathrm{d}x \rangle_{\mathrm{tr}}$. This procedure assures that the determination of the normalized gain is independent of the absolute gain and the particle species respectively. The normalized gain per pad is then determined by the most probable value (MPV) of a Landau distribution fitted to the normalized charge distribution on each pad separately.

Figure 5.11a shows the resulting gain map. Clearly visible are pad rows with lower gain, which correspond to the spacer grid overlapping the the respective pad rows. Also visible is a low-gain region for pad rows >57 due to a malfunctioning HV segment in one of the foils. For rows that are not affected by the mentioned effects, the observed gain spread is ∼10 % (compare Fig. 5.11b). In order not to bias the $\mathrm{d}E/\mathrm{d}x$ measurement, the charge of individual clusters is corrected by the normalized gain factor on a pad-by-pad basis.

5.2.5.2 Inclination angle correction

The rectangular pad shape introduces a dependence of both the maximal (Q_{max}) and total charge (Q_{tot}) collected in a cluster on the inclination angle of the track. The effect is removed by corrections based on simple geometric considerations.

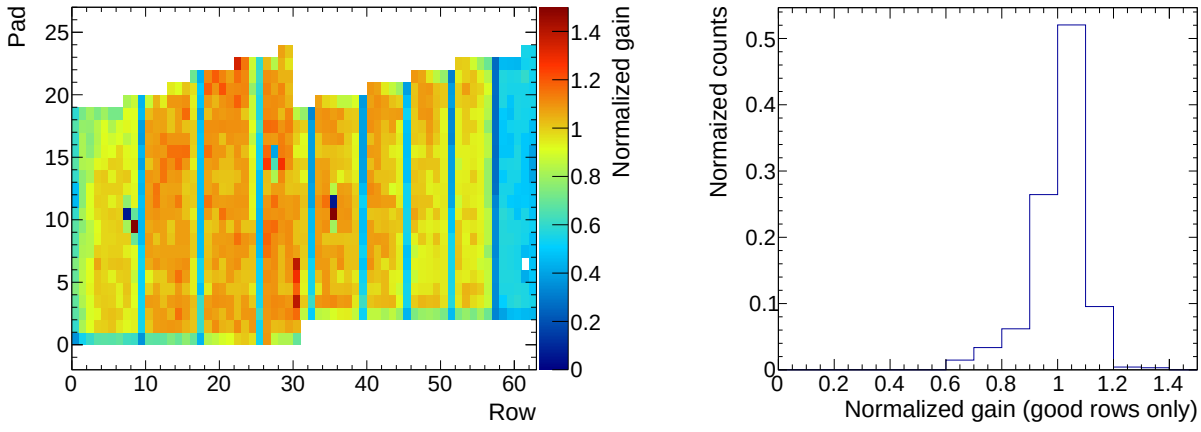

(a) (b)

Figure 5.11: Normalized gain map (a) and the normalized gain of rows not affected by the discussed effects only (b). For further details see text.

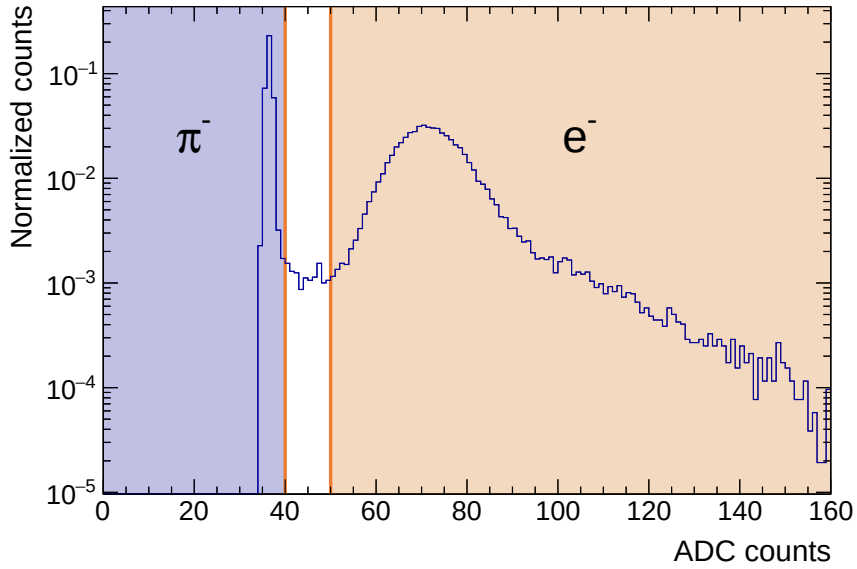

Figure 5.12: Signal of the Cherenkov counter. The cuts are depicted as orange lines, the selected regions used for particle identification as shaded areas.

5.2.6 Event selection

In order to be able to rely on the particle identification provided by the Cherenkov counter, only events containing one track are used for the analysis. Figure 5.12 shows the corresponding signal and depicts the cuts used to differentiate between electrons (*orange*) and pions (*blue*).

Concerning the quality criteria of the tracks, the number of associated clusters is required to be larger than 32. Additional cuts are applied on the cluster drift time, as the cluster charge is corrupted in very low (<25) and high (>90) time bins by wrong triggers (compare Fig. 5.13a). Moreover, as the information taken into account for the computation of the total cluster charge Q_{tot} is incomplete for clusters at the acceptance edge, tracks with more than 30 % clusters in this region are rejected. Figure 5.13b shows a schematic representation. The direction of the beam is depicted by the arrow, while the overall shape of the IROC is shown in light grey. The readout area is the given by the orange and the blue shape, while the region considered as close to the acceptance edge is depicted in blue.

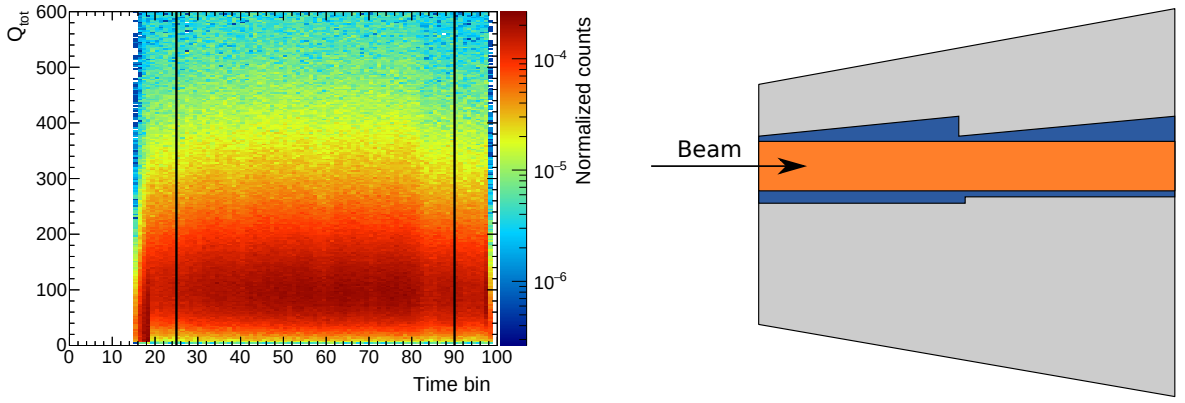

(a) (b)

Figure 5.13: The total cluster charge Q_{tot} as a function of the time bin of the respective cluster with the selection cuts depicted as black lines (a) and a schematic representation of the acceptance cut (b).

6 ALICE TPC simulation

The large number of particles in the final state of heavy-ion collisions imposes a challenge for the detector design, but also for the reconstruction algorithms. Therefore, a predictive and precise simulation of the detector response is mandatory. For this purpose, *Monte Carlo* (MC) simulations are a widely used tool. For the application to the ALICE TPC, in a first step, the energy loss of the incident particle is simulated, followed by a simulation of the drift and the amplification of the ionization electrons in the GEM stack and finally the response of the readout electronics.

Three different configurations of the TPC are available in the AliRoot simulation package [15]. Version 0 provides a coarse geometry without any sensitive element and can thus be used for material budget studies relevant for outer detectors. In Version 1, sensitive volumes are placed at the center of each pad row and hits are created once a track crosses such a sensitive volume, however without taking into account the energy loss of the incident particle. Relevant for this study is Version 2, the so-called *Slow Simulator*. All sectors are sensitive volumes and MC hits are created in every ionizing collision, hence considering the energy loss of the incident particle.

The simulation is based on a modified version of GEANT3 [18] and thoroughly described in [11]. The distance between two successive ionizing collisions of the incident particle with the detector medium is described by an exponential distribution randomly fluctuating around a mean distance D between primary ionization events,

$$D = \frac{1}{N_{\text{prim}} \cdot f(\beta\gamma)}, \tag{6.1}$$

where N_{prim} is the number of primary electrons liberated per cm by a minimally ionizing particle (MIP) and $f(\beta\gamma)$ is the Bethe-Bloch formula, which scales this step length according to the momentum dependence of the specific energy loss corresponding to the particle species. For the Bethe-Bloch formula, the parametrization introduced in Eq. 2.5 is used. At each step, a random energy loss according to $E^{-2.2}$ is assigned to the incident particle, as a slightly steeper dependence of the Rutherford cross-section has been found for light gases [29]. A primary electron with this energy is generated, while for energy transfers higher than 10 keV δ-electrons are produced. The distribution of the number of primary electrons per cm is shown in Fig. 6.1a.

In case the primary electron has sufficient kinetic energy, it can further ionize the detector gas and create a cluster of secondary electrons. The total number of electrons in such a cluster is given by

$$N_{\text{electrons}} = \frac{E_{\text{prim}} - I_0}{W_i} + 1, \tag{6.2}$$

where E_{prim} is the energy of the primary electron, W_i is the effective ionization potential and I_0 is the first ionization potential. The distribution of the total number of electrons liberated in the detector gas by a MIP is shown in Fig. 6.1b.

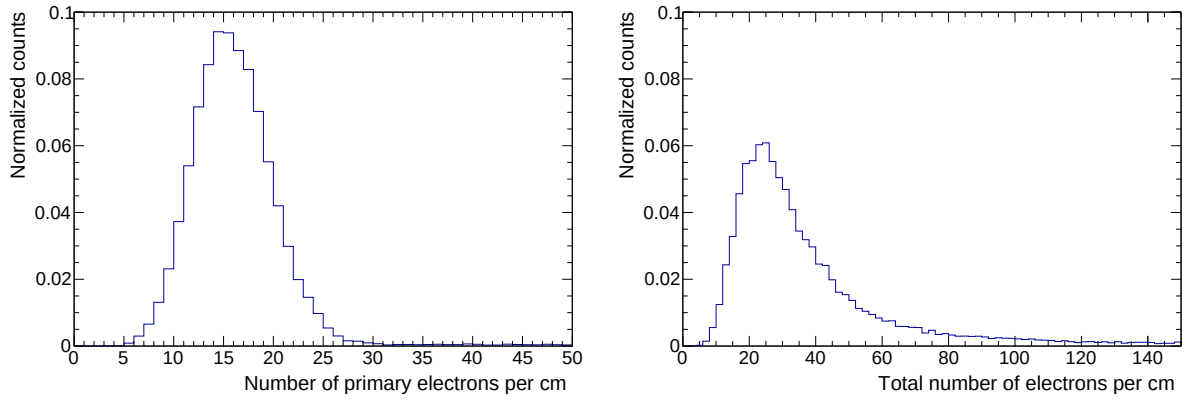

(a) **(b)**

Figure 6.1: Number of primary electrons (a) and total number of electrons (b) liberated per cm by a MIP traversing a chamber filled with Ne-CO_2-N_2 (90-10-5).

While drifting towards the readout anode, the charge spread due to the diffusion is simulated by smearing the point-like cluster randomly with a 3-D Gaussian distribution with a width given by

$$\sigma_{\mathrm{T,\,L}} = D_{\mathrm{T,\,L}} \cdot \sqrt{L_{\mathrm{drift}}}, \tag{6.3}$$

where D_{T} and D_{L} are the the respective diffusion coefficients and L_{drift} the drift length. The absorption of electrons by electronegative molecules such as oxygen is taken into account by randomly removing electrons based on the corresponding drift time and absorption probabilities.

At the amplification stage, each electron is multiplied by the applied gain, which is scaled according to the normalized gain map extracted in Sec. 5.2.5. The resulting avalanche is then a convolution of single-electron avalanches, where random exponential gain fluctuations are taken into account. The pad response function for a GEM-based readout simply projects the electrons onto the pad plane, i.e. the signal is created only on the pad directly below the arrival point of the electron at the amplification stage. The time signal is obtained by folding the electron avalanche with a semi-Gaussian shaping function. The noise distribution is described by a Gaussian with an RMS of about 600 e^- scaled for local variations according to the noise map extracted in Sec. 5.1.3. The same holds for the mean of this distribution, the pedestal value. Finally, the signal is digitized by applying the given dynamic range of the electronics and zero suppression to the integrated signals created by the individual electrons.

The parameters used to steer the simulation are summarized in Tab. 6.1. The reconstruction of simulated events includes all mentioned modifications as described in Sec. 5.2.

Scaling of the electron efficiency

As already discussed in Sec. 3.2, the largest fraction of ions drifting back into the active detector volume stems from the two uppermost GEMs (GEM 1 & 2). A suppression of the *IB* can hence only be achieved by a reduction of the gain in GEM 1. At this stage however, the number of electrons contained in the avalanche is lowest and therefore, the loss of one electron out of a few drastically affects the overall charge collected on the readout anode. Consequently, also the charge collected in the cluster, both Q_{max} and Q_{tot}, is altered and so is the $\mathrm{d}E/\mathrm{d}x$ resolution.

Table 6.1: Gas properties, readout and electronics parameters used in the simulation.

Item		**Value**
Mean number of primary electrons per cm for MIP (N_{prim})		14.0
Total number of electrons per cm for MIP		36.1
First Ionization potential I_0	[eV]	20.77
Effective ionization potential W_i	[eV]	37.3
Drift velocity at 400 V/cm	[cm/µs]	2.58
Longitudinal diffusion constant D_{L}	[µm/$\sqrt{\text{cm}}$]	221
Transverse diffusion constant D_{T}	[µm/$\sqrt{\text{cm}}$]	209
Oxygen content	[ppm]	20
Ratio of anode signal and total pads signal		1
System noise (RMS)	[e^-]	∼600
Dynamic range		2 V; 10 bits
Conversion gain	[mV/fC]	12
Preamp shaper normalization		1
Sampling frequency	[MHz]	20
Zero suppression threshold	[ADC counts]	2

As the electron efficiency decreases for reduced gains, an improved *IB* can only be achieved at the expense of an affected energy resolution - the well-known anti-correlation between *IB* and energy resolution. In order to mimic this effect in the TPC simulation, the electron efficiency of the readout system is degraded. Therefore, before the electrons reach the amplification stage, i.e. before the charge is multiplied by the gain, $(1-n)\cdot 100\,\%$ of the electrons are randomly removed, where $n = 1, 0.9, 0.8, ..., 0.2, 0.1$. As this reduces the charge contained in the avalanche such that it eventually may no longer exceed the threshold of the readout electronics, the gain is scaled accordingly by the inverse of n to account for that.

Simulation of an ^{55}Fe source

In general, a specific HV setting is characterized by its performance in terms of *IB* and the local energy resolution at the ^{55}Fe peak - and not by the electron efficiency. In order to be able to correlate the impact of the scaling of the latter to the performance of a specific HV configuration, a simulation of a ^{55}Fe source is conducted, based on tracks with a fixed step length and energy deposit. In the center of the respective pad rows exactly 158 e^- are created, given by the energy deposit of a ^{55}Fe photon in Ne-CO_2-N_2 (90-10-5). As the digitization, clustering and tracking procedures may introduce further, unknown effects, the ^{55}Fe 'tracks' are filtered through the same analysis chain as the actual data and simulations as described above, respectively.

The energy resolution is then extracted by fitting a Gaussian function to the distribution of the total cluster charge Q_{tot}. The degradation of the energy resolution for different values of $(1-n)\cdot 100\,\%$ is shown in Fig. 6.2.

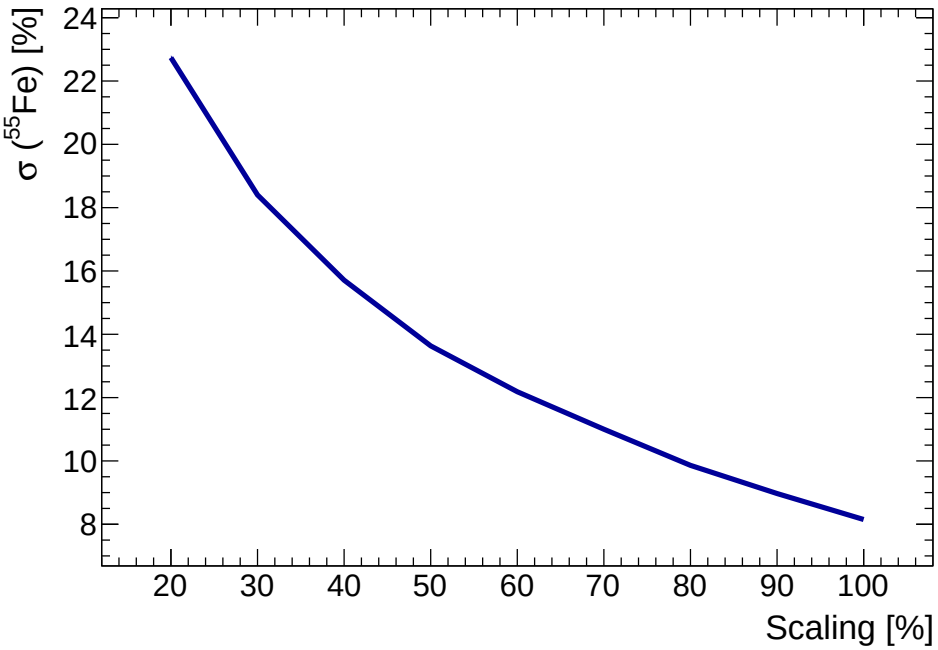

Figure 6.2: Impact of the degradation of the electron efficiency of the readout system on the local energy resolution measured at the ^{55}Fe peak.

7 Results and discussion

The typical track geometry and the performance of the reconstruction algorithms is discussed with an exemplary run. For the extraction of the dE/dx signal, the technique of the truncated mean is used and the such obtained results are extrapolated to the full TPC. As detector effects have a significant impact on the dE/dx resolution, a comparison of simulation and testbeam data is conducted to assure all effects are treated accordingly. Finally, the impact of a degraded energy resolution at the ^{55}Fe peak on the dE/dx resolution and the corresponding separation power is studied for different HV configurations.

7.1 Track reconstruction

In order to characterize typical events of the testbeam and to benchmark the performance of the tracking procedure, the exemplary run 1528 with TF3 = 1 kV/cm is discussed in the following.

The first step is to identify regions of the detector with decreased efficiency. Therefore, the occupancy, defined as the ratio of the number of clusters found on each pad and the number of all clusters and shown in Fig. 7.1a, is monitored. The reduced efficiency of the electron amplification caused by the spacer grid of the frame overlapping with some of the pad rows can be observed. Additionally, the reduced gain in the last sector also affects the efficiency. This effect can be observed in particular in the last pad row of the chamber. As clusters located in the mentioned areas are not considered for the dE/dx computation, these effects are not expected to affect the dE/dx performance of the detector. The number of clusters found per event, shown in Fig. 7.1b, peaks, as expected, around multiples of the 63 available pad rows. The small spike around 30

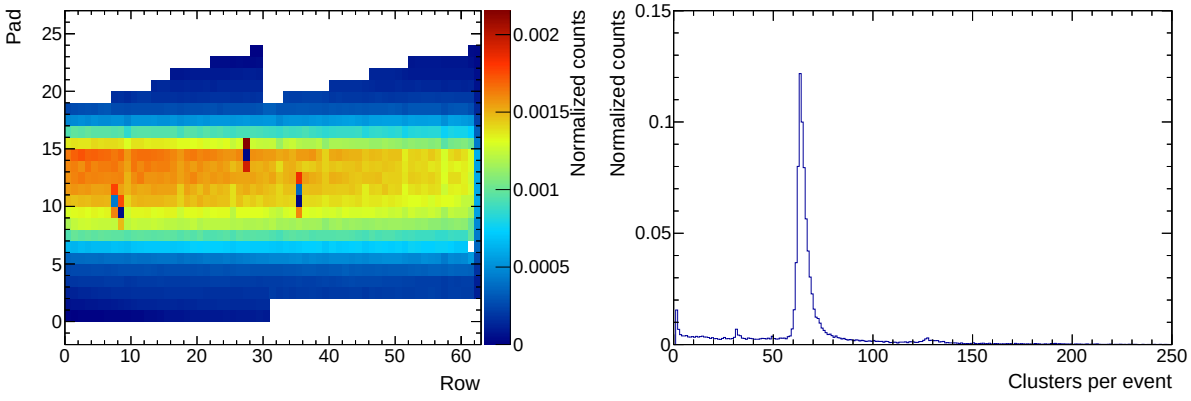

Figure 7.1: Occupancy map (a) and number of clusters found per event (b).

clusters per event is due to tracks that leave the acceptance of the readout at the middle of the chamber; an effect caused by the peculiar shape of the readout area (compare Fig. 5.13b).

The corresponding size of the clusters is determined by counting bins above threshold in the central axes of the pad-time matrix used during clustering. Due to the short drift length, the impact of diffusion is negligible and therefore, the distribution of the cluster size in terms of pads shown in Fig. 7.2a peaks for one pad clusters. Due to the smaller size of the time bins, the typical size of the clusters in z is larger, as visible in Fig. 7.2b.

The number of tracks found by the track reconstruction is shown in Fig. 7.3. As desired, most of the events contain only one track, which allows for using the reference PID provided by the Cherenkov counter. The relatively large number of empty events is in line with considerations of the overall system efficiency, including the triggers. The number of clusters assigned to a track candidate during the seeding procedure is shown in Fig. 7.4a, where the small spike around 30 clusters per event is again due to the acceptance cut off for certain tracks. The final track fitting results in a slightly enhanced number of clusters assigned per track, as visible in Fig. 7.4b.

The figure of merit concerning the quality of the track fit is the reduced χ^2 value, which is defined as the ratio of the χ^2 and the numbers of degrees of freedom of the fit. Ideally, if the estimation of the uncertainties has been conducted properly, the distribution is expected to peak at 1. In this case, the χ^2 value is given by the sum of the uncertainties of each cluster, while the relevant degrees of freedom are the number of clusters per track times the two spatial degrees of freedom in y and z of each cluster.

Therefore, the reduced χ^2 value of a track is directly related to the parametrization of the cluster uncertainties as discussed in Sec. 5.2.1.1. The reduced χ^2 value for the parametrization of the cluster uncertainty for the MWPC is shown in Fig. 7.5a. It is obvious, that the uncertainties are not estimated properly as the distribution peaks around 2. By taking into account the properly extracted uncertainties for a GEM-based readout, the distribution, shown in Fig. 7.5b, peaks around 1, indicating that the uncertainties are estimated properly. Moreover, as the reduced χ^2 value is used as a quality criteria throughout the tracking procedure, by using the proper parametrization of the uncertainties a larger number of tracks is found and in general more clusters are assigned to a track.

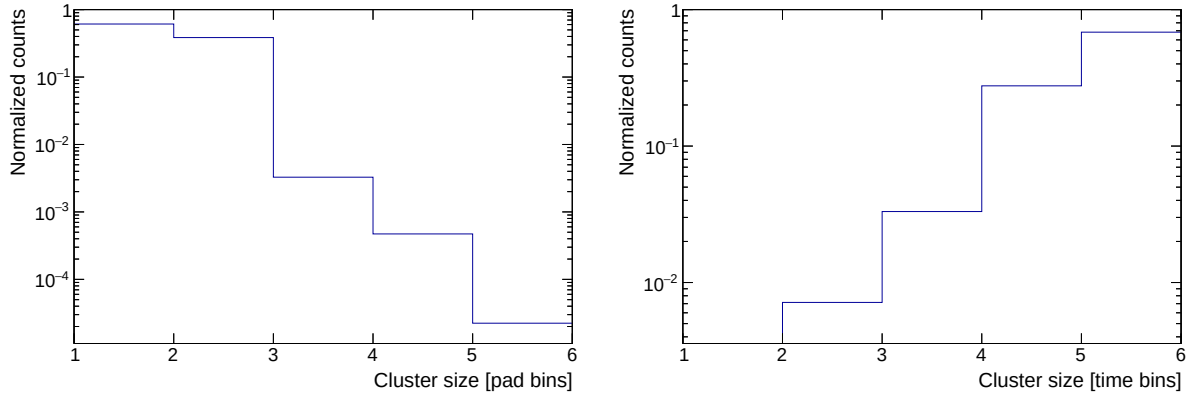

(a) **(b)**

Figure 7.2: Cluster size in terms of pad bins (a) and time bins (b).

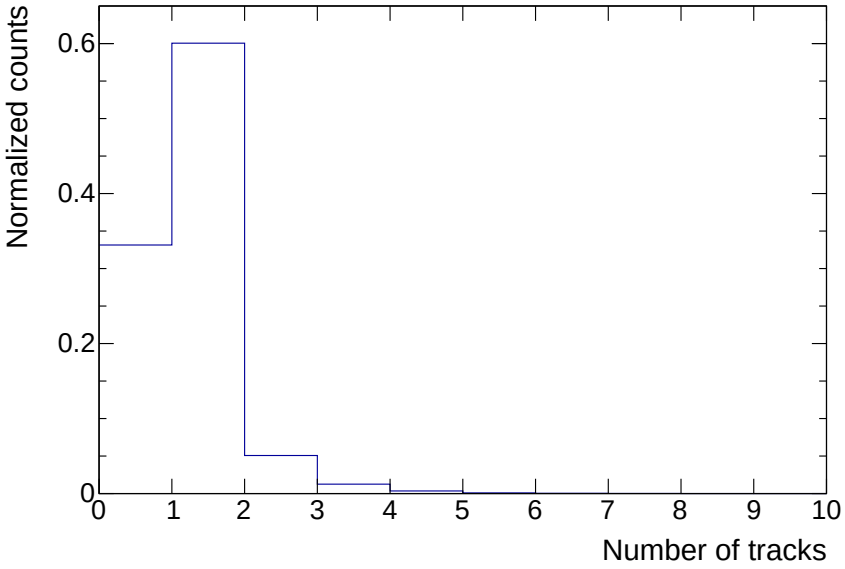

Figure 7.3: Number of tracks found per event.

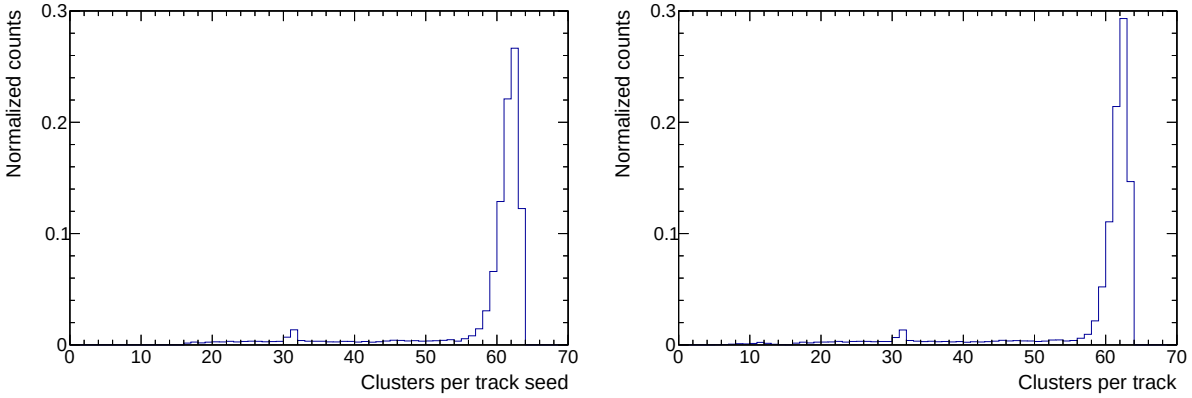

(a) **(b)**

Figure 7.4: Number of clusters assigned per track seed (a) and track (b).

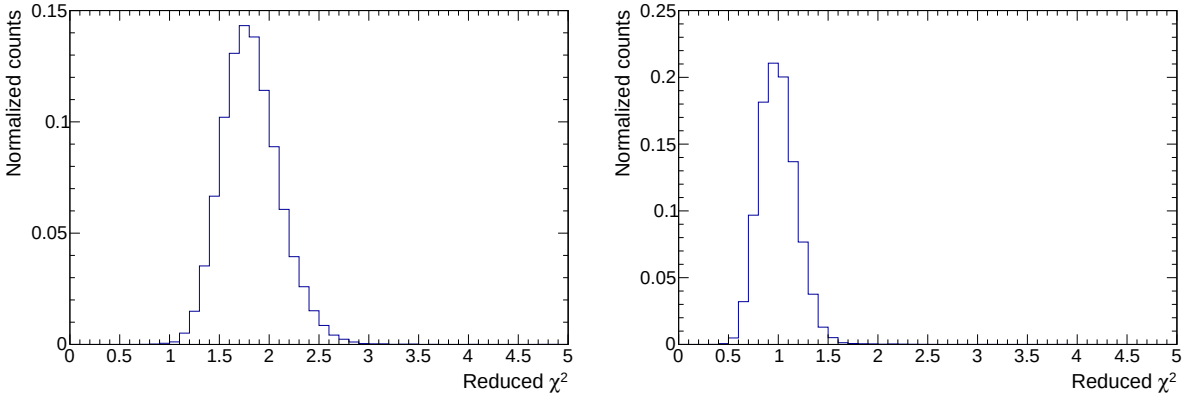

(a) **(b)**

Figure 7.5: Reduced χ^2 distribution before (a) and after the determination of the parametrization of the uncertainty on the cluster position (compare Sec. 5.2.1.1) (b).

Another criteria of the quality of the track fits are the track residuals, which are defined as the distance between each cluster and the crossing point of the track fit with the corresponding pad row. In order not to introduce any bias, the regions affected by the distortions of the drift field and deviations from the nominal gain are not considered for the extraction of the pad and time residuals. The spike at zero for the pad residuals, shown in Fig. 7.6a stems from straight tracks that traverse the chamber along one pad column, while the corresponding size of the clusters extends mainly over one pad per row. This results in a residual close to zero. The time residuals are displayed in Fig. 7.6b. For the extraction of the spatial resolution of the IROC prototype, the respective residual distributions are fitted with the sum of three (y) and two (z) Gaussian functions. The spatial resolution is then given by the amplitude-weighted mean of the width σ of the respective Gaussian functions. For the case of the pad residuals, the contribution of the narrow peak Gaussian is not considered, as it does not describe the shape of the residuals but the effect of straight tracks with mainly one pad clusters traversing the chamber along one pad column.

The resulting spatial resolution is 499.5±2.0 µm in y and 231.4±0.9 µm in z. For a comparable drift length, the spatial resolution of the ALICE TPC has been determined with tracks stemming from cosmic rays to about 370 µm in both y and z [38]. The slight deterioration in y is caused by the smaller cluster size and the accordingly reduced precision with which the space points can be determined, while the slight improvement in z can be contributed to the enhanced sampling frequency compared to the current ALICE TPC and the faster electron signal provided by the GEM amplification stage.

The distribution of the start position of the tracks at the short parallel side of the IROC is shown in Fig. 7.7a for the y-coordinate and in Fig. 7.7b for the z-coordinate, respectively. The distinctive spikes in the y-distribution are due to straight tracks that contain only one pad cluster and extend only over one pad column, while the asymmetric shape is due to the peculiar geometry of the readout (compare Fig. 5.13b).

Figure 7.8a shows the distribution of the ϕ angle, which is defined as the angle between the track and the x-axis. The spike at 0° is due to straight tracks, while the shoulder structure is due to a convolution of the shape of the beam and the effects of the peculiar shape of the readout geometry. The distribution of the inclination angle θ of the track with respect to the z-axis is shown in Fig. 7.8b.

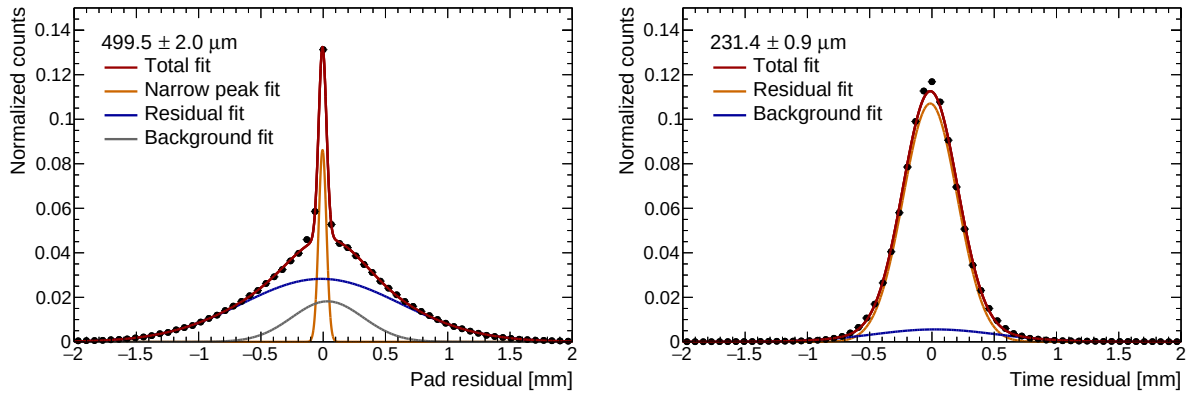

(a) **(b)**

Figure 7.6: Residual distribution in y (a) and z (b).

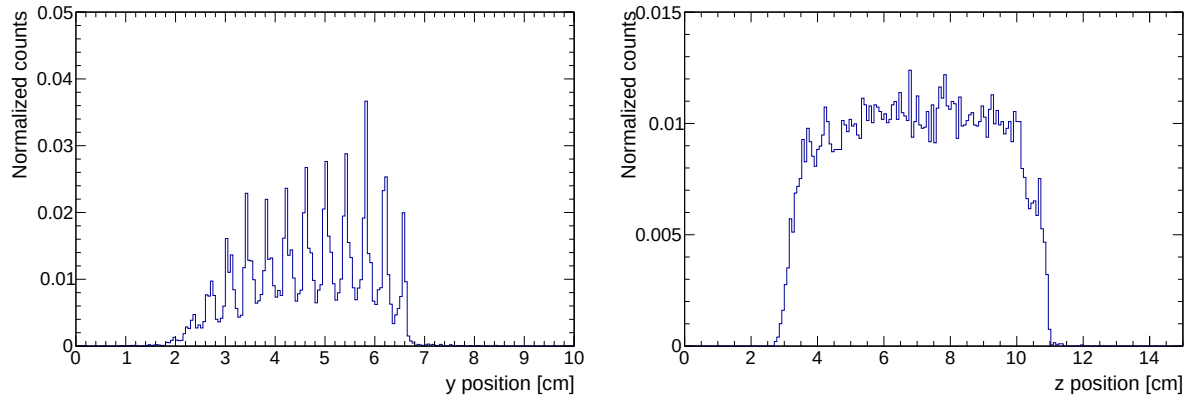

(a) (b)

Figure 7.7: Track start position in y (a) and z (b).

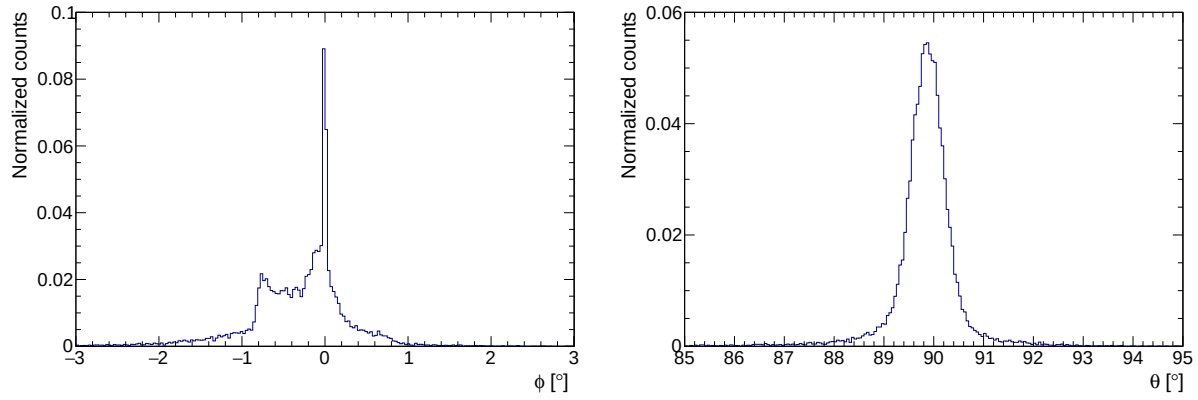

(a) (b)

Figure 7.8: ϕ (a) and θ (b) distribution of the tracks.

7.2 Discussion of the specific energy loss

The specific energy loss $\mathrm{d}E/\mathrm{d}x$ is extracted from the tracks by the technique of the truncated mean as described in Sec. 2.3. In order to find an appropriate set of truncations, the corresponding lower and upper bounds are systematically varied. By convention, a truncation of [5, 75] means that 5 % of the lowest and 25 % of the highest cluster charges contained in a track are discarded. The outcome of this study, applied to the exemplary run 1528, is shown in Fig. 7.9a for the $\mathrm{d}E/\mathrm{d}x$ resolution for electrons and pions respectively and in Fig. 7.9b for the separation power. Even though the differences are fairly small within the errors, a slight preference towards the truncations [0, 70] can be observed. Therefore, these truncations have been chosen, also in order to comply with the TDR analysis.

The resulting $\mathrm{d}E/\mathrm{d}x$ spectra are shown in Fig. 7.10a for the total cluster charge Q_{tot} and in Fig. 7.10b for the maximal cluster charge Q_{max}. The $\mathrm{d}E/\mathrm{d}x$ resolution is extracted by fitting a Gaussian function to the two peaks in the spectrum corresponding to electrons and pions respectively and applying Eqs. 2.19 and 2.20. In general, the *TDR analysis* yields results which are about 9 % better than the results presented in this work. The reason for this difference is still

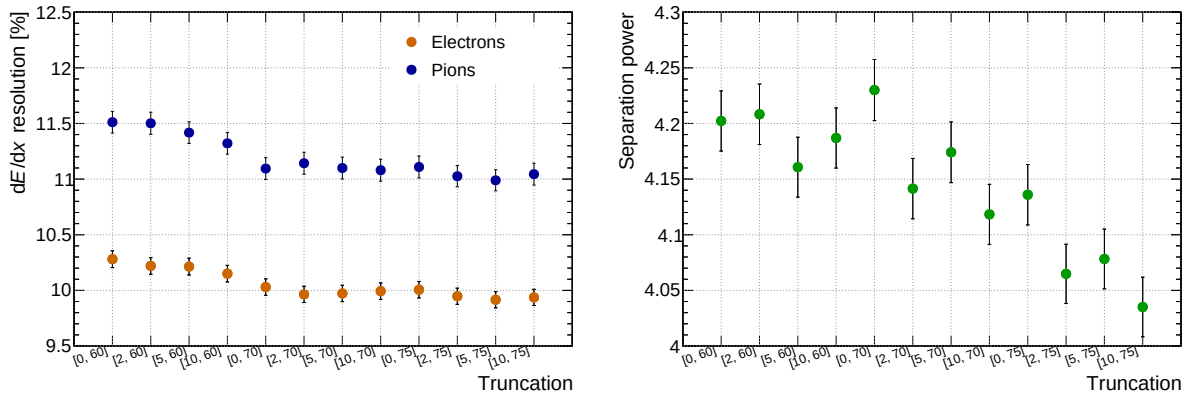

(a) **(b)**

Figure 7.9: Energy resolution (a) and separation power as a function of different truncations.

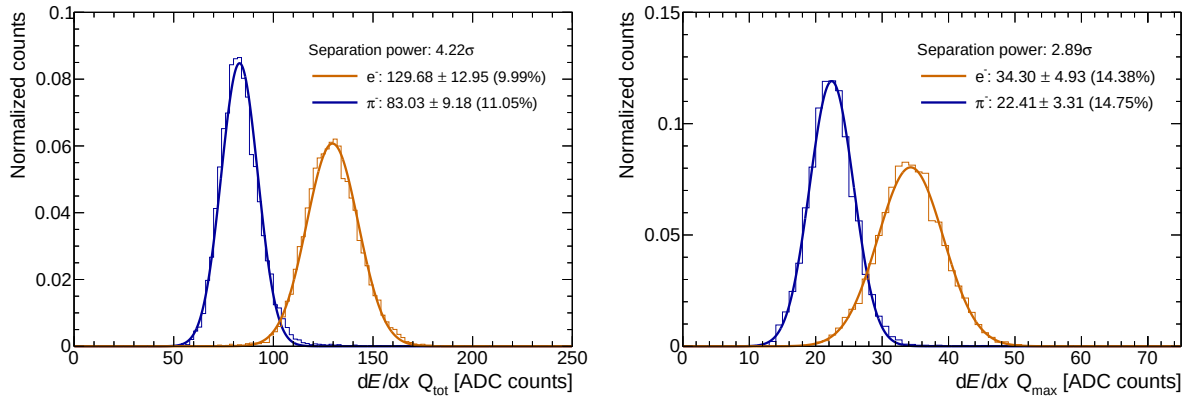

(a) **(b)**

Figure 7.10: $\mathrm{d}E/\mathrm{d}x$ distribution of Q_{tot} (a) and Q_{max} (b).

under investigation, but most probably related to the very complicated and for the purposes of this study not optimized track reconstruction scheme of AliRoot.

In order to predict the performance of the ALICE TPC fully equipped with a GEM-based readout, the $\mathrm{d}E/\mathrm{d}x$ performance of the IROC prototype is extrapolated. Therefore, long tracks with up to 160 clusters are artificially build up from clusters stemming from pad rows that are not affected by gain variations or field distortions. One shortcoming of this approach is however, that by combining clusters from different tracks or separated regions, possible correlations between neighbouring clusters are not considered. These correlations can be caused by the charge spread due to diffusion or effects of the PRF and reduce the generic information on the track as the measurement of ideally independent clusters becomes correlated. Consequently, this potential loss of information results in a deteriorated $\mathrm{d}E/\mathrm{d}x$ resolution.

Therefore, in order to prove the validity of this approach, the actual result from the testbeam is overlain to the result of the extrapolation shown in Fig. 7.11. Instead of the number of all available pad rows in the IROC, the mean number of clusters used to compute the $\langle \mathrm{d}E/\mathrm{d}x \rangle_{\mathrm{tr}}$ is shown. The respective $\mathrm{d}E/\mathrm{d}x$ resolutions are found to be compatible within the errors, as no correlations are expected due to the narrow PRF of GEMs and the negligible diffusion.

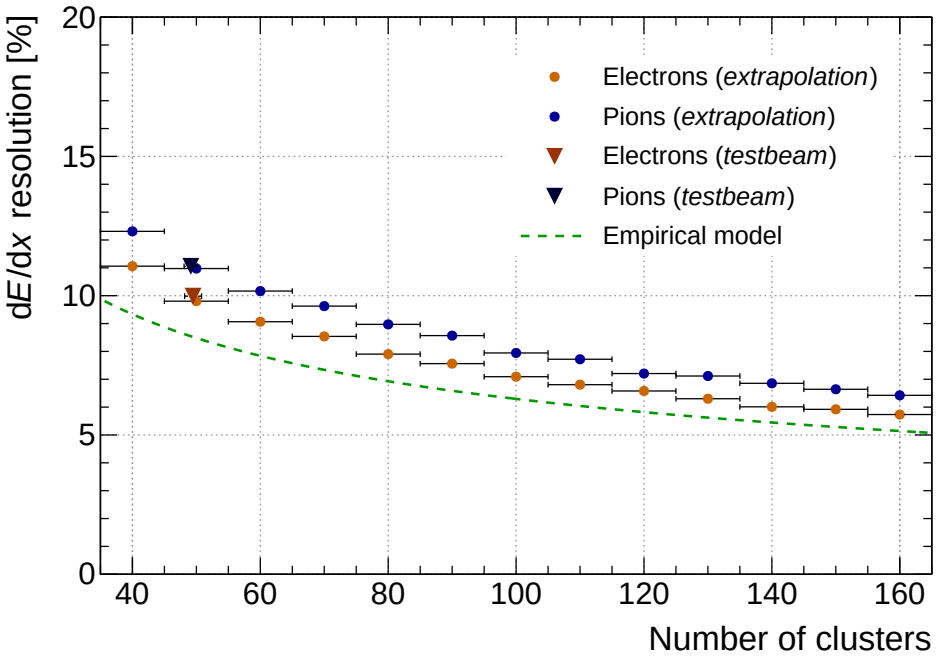

Figure 7.11: $\mathrm{d}E/\mathrm{d}x$ resolution of electrons and pions as a function of varying cluster numbers per track (extrapolation) together with the prediction of an empirical model introduced in Eq. 2.21.

A direct comparison of the such obtained result to the performance of the currently used MWPCs installed in the ALICE TPC is difficult, as data for such short drift lengths are not available. The $\mathrm{d}E/\mathrm{d}x$ resolution of the ALICE TPC, integrated over all momenta, inclination angles and particle species, is about 5.2 % [5].

Additionally, the prediction of the empirical model as introduced in Eq. 2.21 is shown. Even though the model slightly over-predicts the $\mathrm{d}E/\mathrm{d}x$ resolution, the trend of the data is well reproduced.

7.3 ALICE TPC simulation

Detector effects, such as diffusion, gain variations and the pad response, have been shown to significantly impact the $\mathrm{d}E/\mathrm{d}x$ resolution [72]. Therefore, a comparison of the corresponding figures of merit of simulation and testbeam data is mandatory to conclusively obtain a thorough understanding of the detector response. This is in particular important as the full simulation code has been optimized for long drift distances of $\mathcal{O}(\mathrm{m})$ and a MWPC-based readout.

To this end, the exemplary run introduced in the last section is compared to the results of simulations at similar values of gain and energy resolution $\sigma(^{55}\mathrm{Fe})$. The simulations have been conducted such, that the track geometry described in the last section is well reproduced. In a first step, the straggling functions for both Q_{tot} and Q_{max} are compared as shown in Fig. 7.12a and 7.12b respectively for pions. The agreement between data and simulation is reasonable and similar in the case of the electrons, which is not shown here.

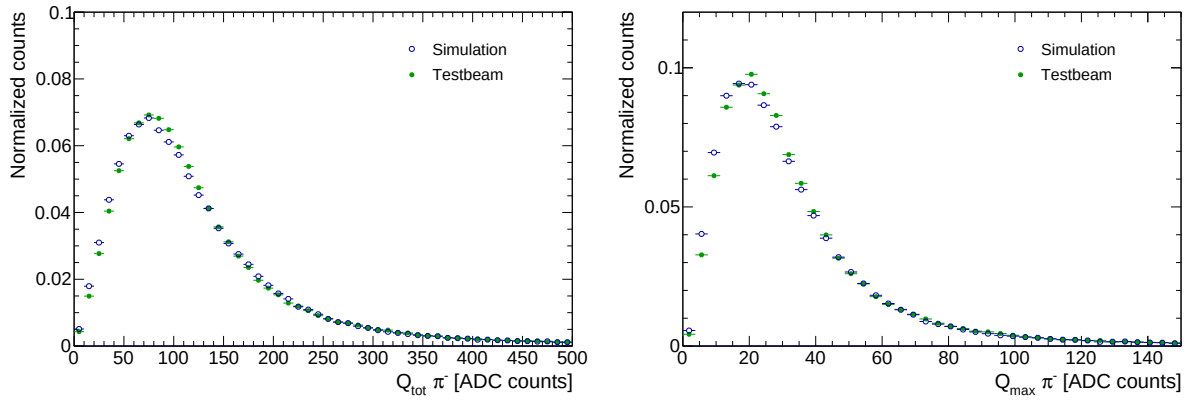

(a) **(b)**

Figure 7.12: Straggling function of pions. The total charge Q_{tot} is shown in panel (a) and the maximum charge Q_{max} in panel (b).

In order to monitor whether the correlations between neighbouring clusters are reproduced in the simulation, the charge measured in one row is monitored as a function of the mean charge of all clusters in the neighbouring pad row. In case the charges are uncorrelated, the distributions shown in Fig. 7.13a for pions and in Fig. 7.13b for electrons are expected to be flat.

As anticipated due to the narrow PRF of GEMs and the short drift length, the experimental data shows almost no correlations. This is fairly well reproduced by the simulation, even though the slope is slightly flatter. However, the difference can be neglected, as it is not supposed to have any impact on the $\mathrm{d}E/\mathrm{d}x$ resolution. This is well justified, as the random assignment of clusters to the extrapolated artificial tracks for Fig. 7.11, which removes any correlations, did not either.

The corresponding size of the clusters is determined as mentioned in the previous section. For the size in terms of pad bins, shown in Fig. 7.14a, the number of one- and two pad clusters is well described, while the agreement for larger cluster sizes is only poor. In order to prove, that this discrepancy is not introduced by threshold effects of the readout, the thresholds are randomly reduced by maximally 20 %. As this procedure does not change the distributions, such effects can be ruled out as as the source of this inconsistency. Therefore, the occurrence of this effect can be

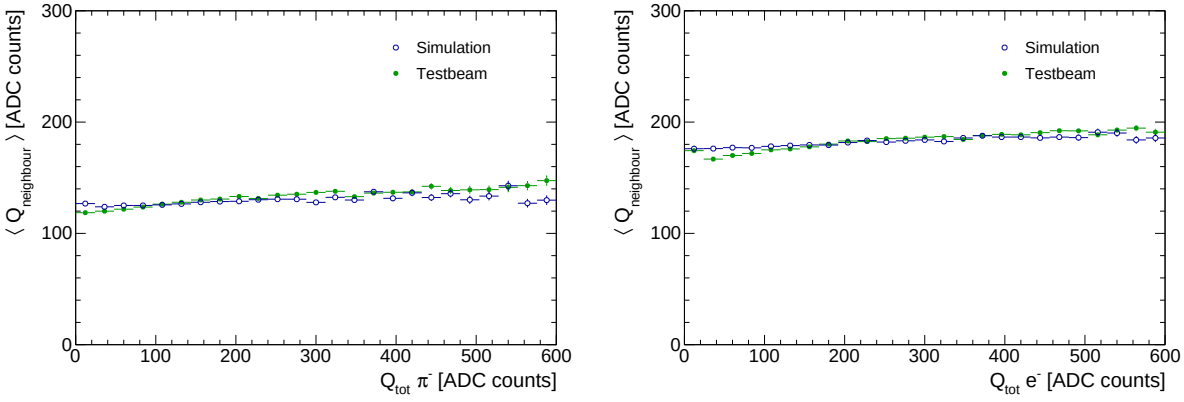

(a) **(b)**

Figure 7.13: Row couplings for pions (a) and electrons (b).

attributed to either problems of the simulation code treating the diffusion for such short drift lengths or a contribution of non-projective effects to the PRF in the data.

Concerning the cluster size in terms of time bins, shown in Fig. 7.14b, a systematic shift towards smaller cluster sizes can be observed. Also in this case, threshold effects can be excluded as the source of this shift. However, the reason for this discrepancy can be attributed to the fact, that the time response of the simulation code requires further optimization to exactly match the situation of the testbeam.

Correspondingly, the shape of the pad and time residuals, shown in Fig. 7.15a and 7.15b respectively, is not exactly reproduced. Due to the suppression of larger cluster sizes in terms of pad bins, the computation of the COG of a cluster is less reliable and therefore, the distribution is slightly broader. The shape of the time residuals is slightly too narrow, which can be contributed to the response of the readout and the accordingly reduced cluster size, as mentioned above.

The resulting $\mathrm{d}E/\mathrm{d}x$ spectra are shown in Fig. 7.16a for the total cluster charge Q_{tot} and in Fig. 7.16b for the maximal cluster charge Q_{max} together with the resulting $\mathrm{d}E/\mathrm{d}x$ resolutions.

The agreement of data and simulation is reasonable for both spectra and notably also the tail towards higher energy deposits is well reproduced. Yet, the simulation over-predicts the resulting $\mathrm{d}E/\mathrm{d}x$ resolution by about 10 %. This difference can be most probably attributed to the mentioned discrepancy of the presented analysis of the testbeam data with the *TDR analysis*. Other possibilities could be problems of the simulation code treating the diffusion for such short drift length or a contribution of non-projective effects to the PRF in the data. Therefore, further investigations are necessary in order to fully understand the detector response in the simulation.

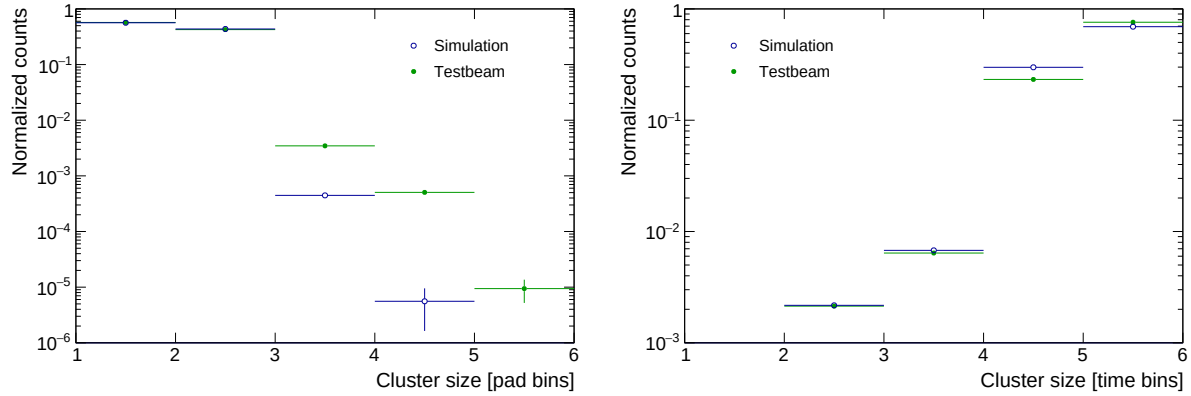

(a) **(b)**

Figure 7.14: Cluster size in terms of pad bins (a) and time bins (b).

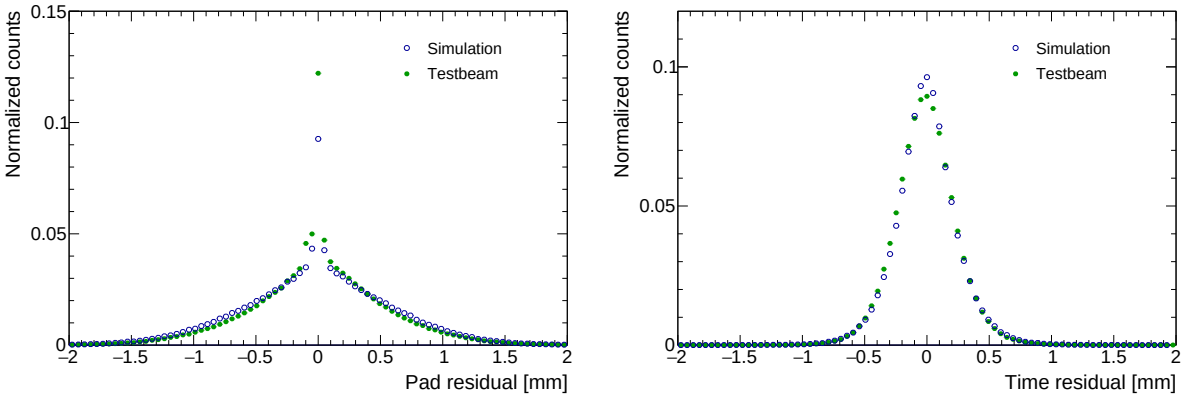

(a) **(b)**

Figure 7.15: Residual distribution in y (a) and z (b).

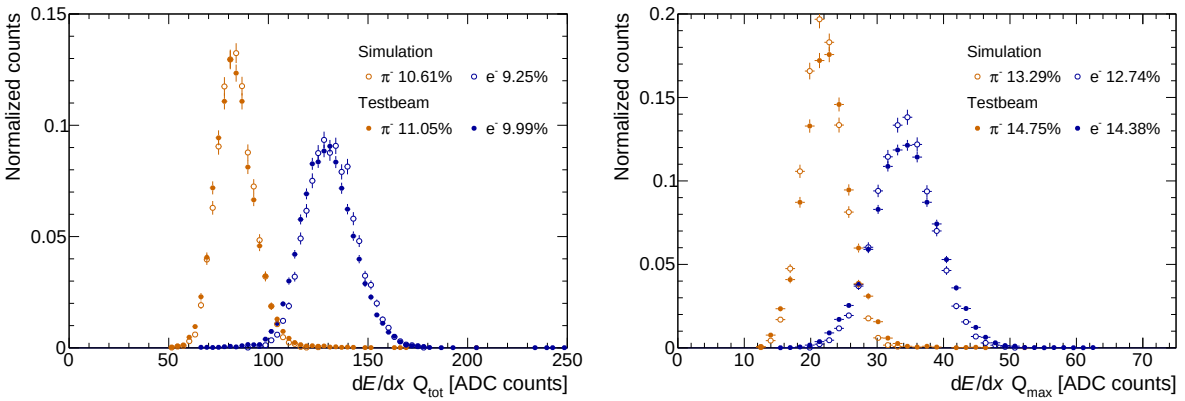

(a) **(b)**

Figure 7.16: $\mathrm{d}E/\mathrm{d}x$ distribution for Q_{tot} (a) and Q_{max} (b). The corresponding $\mathrm{d}E/\mathrm{d}x$ resolutions are quoted.

7.4 Testbeam results

In order to study the impact of the local energy resolution at the ^{55}Fe peak on the dE/dx resolution, a systematic study of different HV configurations corresponding to different values of *IB* and $\sigma(^{55}\text{Fe})$ is conducted. The respective HV settings are summarized in Tab. 3.1. The results of runs employing the same HV configuration are merged by taking into account variations of the gain due to changes in the ambient conditions. Therefore, a parametrized correction factor based on the interpolation of the variable in question (e.g. the separation power or the dE/dx resolution) to a gain of 2000 is employed, before averaging the accordingly corrected results.

A gain scan is performed with the TF3 = 1 kV/cm setting. The variation of the gain, ranging from about 1000 to 4000, is obtained by scaling up and down the HV applied to the resistor chain. The resulting separation power is shown in Fig. 7.17. A notable improvement can be observed only for gains between 1000 and 2000, while the curve significantly flattens for larger gains. In this light, the choice of a gain of 2000 is well justified.

The impact of the energy resolution at the ^{55}Fe peak on the dE/dx resolution is studied by systematically scanning the different HV configurations, which correspond to specific values of *IB* and energy resolution at a gain of 2000. The results of this study are shown in Fig. 7.18a for pions and in Fig. 7.18b for electrons respectively. As expected, the dE/dx resolution decreases as the energy resolution degrades.

In order to compare the such obtained results to the outcome of the simulation, the gain used in the simulation is scaled to fit the mean position of the truncated mean of the electrons $\mu_{\langle \mathrm{d}E/\mathrm{d}x\rangle_{\mathrm{tr}_{e^-}}}$ for the non-scaled case $n = 1$. The electron efficiency of the readout system is degraded as described in Chap. 6, while the gain is kept at the above determined value. The electron efficiency

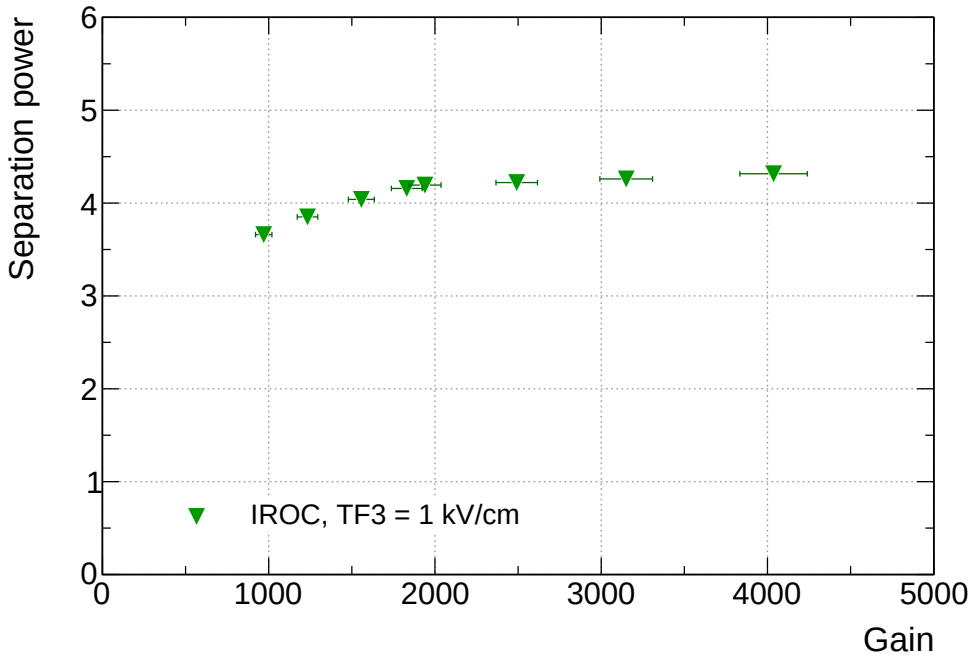

Figure 7.17: Separation power of pions and electrons at 1 GeV/c as a function of the gain at an *IB* of 0.63 %.

is correlated to the energy resolution via the ^{55}Fe simulation, where it is decreased correspondingly. Consistently with the outcome of the previous Section, the simulation over-predicts the dE/dx resolution by about 10 %. In particular, the pions are slightly better reproduced than the electrons, which is a known issue of the TPC simulation. Apart from that, for low values of $\sigma(^{55}\text{Fe})$, the trend of the data is very well reproduced. With increasing $\sigma(^{55}\text{Fe})$ however, the simulation fails to describe the onset of saturation of the dE/dx resolution. This can be attributed to the fact, that the charge amplification mechanisms in a stack of four GEMs are much more complicated than just a linear one-parameter scaling. In this light, this simple model, where the electron efficiency of a one-stage amplification structure is scaled, works remarkably well.

The corresponding separation power is shown in Fig. 7.19 as a function of the ^{55}Fe energy resolution. Also the separation power decreases as the ^{55}Fe resolution is degraded, even though the dependence is rather modest. In contrast to the individual dE/dx resolutions, the simulation describes both the trend and the absolute values of the separation power very well. The GEM-based IROC prototype achieves a dE/dx performance with a HV configuration that implies an energy resolution of 14 % at the ^{55}Fe peak at an *IB* below 0.5 %, which fully complies with the requirements for the ALICE TPC upgrade. This is depicted in Fig. 7.20, which shows the dependence of the separation power on the *IB*.

Therefore, the conclusion of the testbeam campaign is, that the demanding requirements of the ALICE upgrade physics programme can be fulfilled. The dedicated simulations partially describe the trend of the dE/dx resolution as the electron efficiency of the readout is degraded, while the absolute values differ by about 10 %. This discrepancy is however rather due to problems with the reconstructed data than to an over-prediction by the simulation. The agreement between simulation and data concerning the separation power is remarkably good.

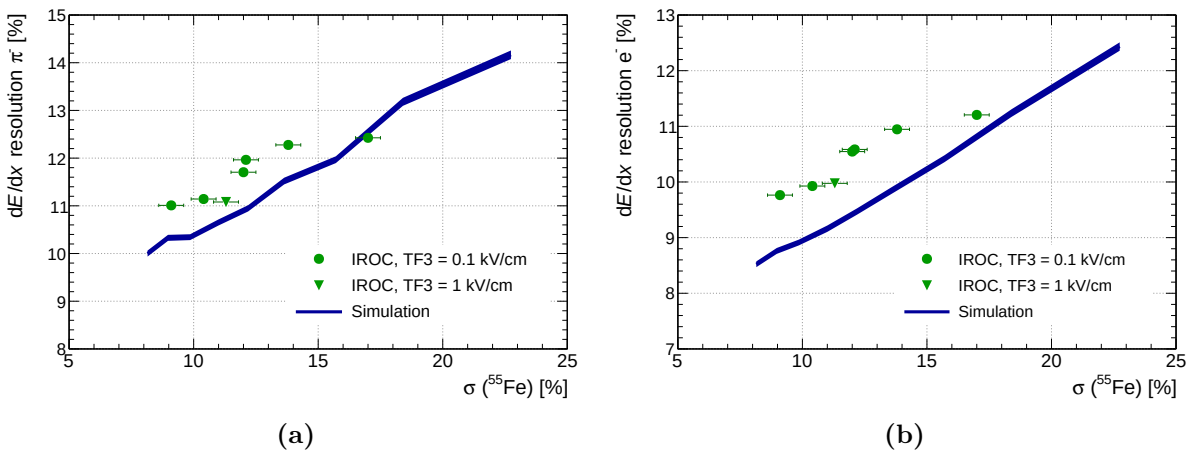

(a) **(b)**

Figure 7.18: dE/dx resolution as a function of $\sigma(^{55}\text{Fe})$ for pions (a) and electrons (b). The blue curve shows the result of the simulation.

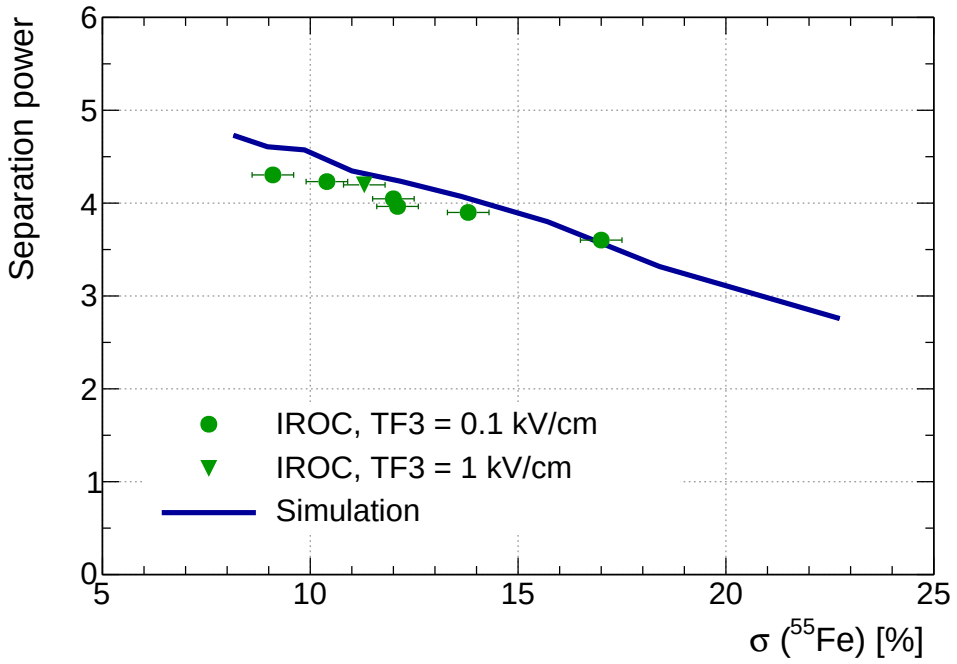

Figure 7.19: Separation power of pions and electrons at 1 GeV/c as a function of the $\sigma(^{55}\mathrm{Fe})$ resolution. The blue curve shows the result of the simulation.

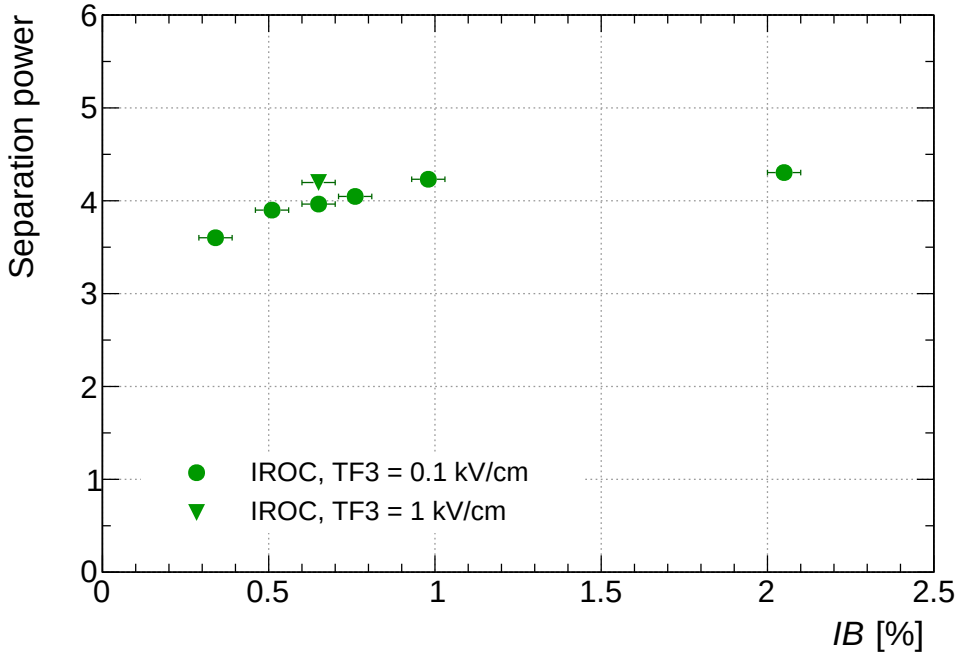

Figure 7.20: Separation power of pions and electrons at 1 GeV/c as a function of the *IB*.

8 Conclusions and Outlook

This work presents the result of a comprehensive dE/dx resolution study conducted with a GEM-based large-size prototype for the ALICE TPC.

The increased LHC luminosity envisaged for the RUN3 beyond 2020 implies significant upgrades of the ALICE TPC, as the gating grid of the current MWPC-based readout chambers imposes by then unacceptable rate limitations. The proposed solution for the upgrade is a readout comprised out of a stack of four large-size GEM foils, containing both Standard (S, 140 µm pitch) and Large Pitch (LP, 280 µm pitch) GEMs arranged in the order S-LP-LP-S.

In the course of this work, a first prototype of the ALICE Outer Readout Chamber (OROC) has been successfully assembled and equipped with such a stack, which demonstrated the feasibility of GEM integration on readout chambers of so far unprecedented size. Moreover, the corresponding quality assurance and production procedures could be defined, validated and improved. Studies of the foil sag towards the pad plane due to electrostatic attraction conducted with this prototype yielded, that an additional cross introduced to the frame can sufficiently compensate for this effect.

The dE/dx resolution is a crucial detector parameter for the particle identification (PID) via measurement of the specific energy loss. As the ALICE TPC is the main device for PID in ALICE, it is therefore of particular importance that its excellent capabilities are retained after the upgrade. This work provides proof, that the dE/dx resolution of a GEM-based prototype of the ALICE Inner Readout Chamber (IROC) conforms with the requirements of the ALICE upgrade physics programme. To this end, a comprehensive study of different HV configurations, each characterized by the specific performance in terms of *Ion Backflow* (*IB*) and energy resolution at the ^{55}Fe peak, has been conducted with this prototype at the CERN Proton Synchrotron. The AliRoot framework was used to reconstruct the particle tracks from the measured digits. Several modifications of the reconstruction algorithms were necessary due to the replacement of the MWPCs with a GEM-based readout. Moreover, a parametrization of the uncertainty on the position measurement of the ionization clusters taking into account track parameters has been extracted and applied. The spread of local variations of the electron amplification in the GEM-stack has been quantified with tracks from the testbeam to about 10 %.

Using the technique of the truncated mean, the dE/dx signal has been finally extracted. With a HV configuration implying a local energy resolution of 14 % at the ^{55}Fe peak and an *IB* below 0.5 %, the GEM-based IROC prototype achieves the performance required to retain the current PID capabilities of the ALICE TPC. The results are compared to the outcome of a full-scale simulation, where the local energy resolution is degraded by decreasing the electron efficiency of the readout system. A discrepancy of about 10 % is found in the dE/dx performance of the simulation with respect to the results measured with the IROC prototype, while the trend of the data is in large part described. The separation power is fully reproduced.

Further investigations of the time response of the readout and the treatment of diffusion processes in the simulation code are mandatory to improve the results and tune the simulation code for the upcoming LHC RUN3. In this light, also tests of a large-size prototype with a drift length comparable to the ALICE TPC are necessary to study the $\mathrm{d}E/\mathrm{d}x$ performance in a more realistic environment. In order to find a more sophisticated model of the degradation of the energy resolution, a detailed study of the amplification process in a stack of four GEMs should be conducted, accompanied by Garfield/Magboltz simulations of the relevant processes.

The excellent performance of the GEM-based IROC prototype provides a final proof of the feasibility of the upgrade of the ALICE TPC. Therefore, the project is now proceeding to the phase of mass production: Starting from 2016, 40 Inner and 40 Outer Readout Chambers are to be built, tested and commissioned within the next years. The replacement, installation of new electronics and commissioning of the TPC will take place during the Long Shutdown 2 of the LHC starting in 2019.

A List of runs

Run	Beam [GeV/c]	IB [%]	SF [%]	TF3 V/cm	G3/G4	$\sigma(^{55}\text{Fe})$ [%]	Gain
1378	-1	0.63	99	1000	0.8	11.3	2000
1379	-1	0.63	99	1000	0.8	11.3	2000
1380	-1	0.63	99	1000	0.8	11.3	2000
1381	-1	0.63	99	1000	0.8	11.3	2000
1382	-1	0.63	99	1000	0.8	11.3	2000
1383	-1	0.63	99	1000	0.8	11.3	2000
1384	-1	0.63	99	1000	0.8	11.3	2000
1387	-1	0.63	99	1000	0.8	11.3	2000
1388	-1	0.63	99	1000	0.8	11.3	2000
1395	-1	0.63	99	1000	0.8	11.3	2000
1396	-1	0.63	99	1000	0.8	11.3	2000
1397	-1	0.63	99	1000	0.8	11.3	2000
1399	-1	0.63	99	1000	0.8	11.3	2000
1400	-1	0.63	99	1000	0.8	11.3	2000
1401	-2	0.63	99	1000	0.8	11.3	2000
1407	-2	0.63	99	1000	0.8	11.3	2000
1408	-2	0.63	99	1000	0.8	11.3	2000
1409	-2	0.63	99	1000	0.8	11.3	2000
1410	-2	0.63	99	1000	0.8	11.3	2000
1411	-2	0.63	99	1000	0.8	11.3	2000
1412	-2	0.63	99	1000	0.8	11.3	2000
1414	-2	0.63	99	1000	0.8	11.3	2000
1415	-2	0.63	99	1000	0.8	11.3	2000
1417	-2	0.63	99	1000	0.8	11.3	2000
1418	-2	0.63	99	1000	0.8	11.3	2000
1419	-2	0.63	99	1000	0.8	11.3	2000
1420	-2	0.63	99	1000	0.8	11.3	2000
1425	-2	0.63	99	1000	0.8	11.3	2000
1434	-3	0.63	99	1000	0.8	11.3	2000
1435	-3	0.63	99	1000	0.8	11.3	2000
1437	-3	0.63	99	1000	0.8	11.3	2000
1438	-3	0.63	99	1000	0.8	11.3	2000
1439	-3	0.63	99	1000	0.8	11.3	2000
1440	-3	0.63	99	1000	0.8	11.3	2000
1441	-3	0.63	99	1000	0.8	11.3	2000
1442	-3	0.63	99	1000	0.8	11.3	2000
1443	-3	0.63	99	1000	0.8	11.3	2000
1444	-3	0.63	99	1000	0.8	11.3	2000

Run	Beam [GeV/c]	IB [%]	SF [%]	TF3 V/cm	G3/G4	$\sigma(^{55}Fe)$ [%]	Gain
1447	-3	0.63	99	1000	0.8	11.3	2000
1448	-3	0.63	99	1000	0.8	11.3	2000
1450	-3	0.63	99	1000	0.8	11.3	2000
1456	-3	0.63	99	1000	0.8	11.3	2000
1460	-3	0.63	99	1000	0.8	11.3	2000
1461	-1	0.63	96	1000	0.8	11.3	1000
1462	-1	0.63	96	1000	0.8	11.3	1000
1463	-1	0.63	96	1000	0.8	11.3	1000
1464	-1	0.63	96	1000	0.8	11.3	1000
1465	-1	0.63	96	1000	0.8	11.3	1000
1466	-1	0.63	96	1000	0.8	11.3	1000
1467	-1	0.63	96	1000	0.8	11.3	1000
1468	-1	0.63	96	1000	0.8	11.3	1000
1469	-1	0.63	96	1000	0.8	11.3	1000
1470	-1	0.63	96	1000	0.8	11.3	1000
1471	-1	0.63	96	1000	0.8	11.3	1000
1472	-1	0.63	96	1000	0.8	11.3	1000
1475	-1	0.63	96	1000	0.8	11.3	1000
1476	-1	0.63	96	1000	0.8	11.3	1000
1477	-1	0.63	96	1000	0.8	11.3	1000
1478	-1	0.63	99	1000	0.8	11.3	2000
1479	-1	0.63	101	1000	0.8	11.3	3500
1480	-1	0.63	101	1000	0.8	11.3	3500
1482	-1	0.63	101	1000	0.8	11.3	3500
1485	-1	2.05	99	100	0.8	9.1	1800
1486	-1	2.05	99	100	0.8	9.1	1800
1487	-1	2.05	99	100	0.8	9.1	1800
1490	-1	2.05	100	100	0.8	9.1	2100
1491	-1	2.05	100	100	0.8	9.1	2100
1492	-1	2.05	100	100	0.8	9.1	2100
1493	-1	0.98	100	100	0.8	10.4	2500
1494	-1	0.98	100	100	0.8	10.4	2500
1495	-1	0.98	99	100	0.8	10.4	2000
1496	-1	0.98	99	100	0.8	10.4	2000
1499	-1	0.98	99	100	0.8	10.4	2000
1502	-1	0.34	100	100	0.8	17.0	2500
1504	-1	0.34	99	100	0.8	17.0	2000
1510	-1	0.34	99	100	0.8	17.0	2000
1513	-1	0.34	99	100	0.8	17.0	2000
1514	-1	0.34	99	100	0.8	17.0	2000
1516	-1	0.34	99	100	0.8	17.0	2000
1520	-1	0.63	102	1000	0.8	11.3	4000
1521	-1	0.63	102	1000	0.8	11.3	4000
1524	-1	0.63	102	1000	0.8	11.3	4000
1528	-1	0.63	100	1000	0.8	11.3	2000
1529	-1	0.63	100	1000	0.8	11.3	2000

Run	Beam [GeV/c]	IB [%]	SF [%]	TF3 V/cm	G3/G4	$\sigma(^{55}Fe)$ [%]	Gain
1530	-1	0.63	97	1000	0.8	11.3	1000
1531	-1	0.63	97	1000	0.8	11.3	1000
1532	-1	0.63	98	1000	0.8	11.3	1000
1533	-1	0.63	98	1000	0.8	11.3	1000
1535	-1	0.65	100	100	0.8	12.1	2000
1536	-1	0.65	100	100	0.8	12.1	2000
1538	-1	0.65	100	100	0.8	12.1	2000
1540	-1	0.65	100	100	0.8	12.1	2000
1541	-1	0.51	100	100	0.8	13.8	2000
1542	-1	0.51	100	100	0.8	13.8	2000
1544	-1	0.51	100	100	0.8	13.8	2000
1545	-1	0.51	99	100	0.8	13.8	2000
1549	-1	0.51	99	100	0.8	13.8	2000
1551	-1	0.51	99	100	0.8	13.8	2000
1553	-1	0.51	99	100	0.8	13.8	2000
1554	-1	0.51	99	100	0.8	13.8	2000
1555	-1	0.76	99	100	0.95	12.0	2000
1557	-1	0.76	99	100	0.95	12.0	2000
1558	-1	0.76	99	100	0.95	12.0	2000
1560	-1	0.76	99	100	0.95	12.0	2000
1585	-1	0.63	99	1000	0.8	11.3	2000
1586	-1	0.63	99	1000	0.8	11.3	2000
1587	-1	0.63	98	1000	0.8	11.3	2000
1588	-1	0.63	98	1000	0.8	11.3	2000
1589	-1	0.63	97	1000	0.8	11.3	2000
1592	-1	0.63	97	1000	0.8	11.3	2000
1593	-1	0.63	100	1000	0.8	11.3	2000
1594	-1	0.63	100	1000	0.8	11.3	2000
1595	-1	0.63	100	1000	0.8	11.3	2000
1596	-1	0.63	101	1000	0.8	11.3	2000
1597	-1	0.63	101	1000	0.8	11.3	2000
1598	-1	0.63	102	1000	0.8	11.3	2000
1601	-1	0.63	102	1000	0.8	11.3	2000
1602	-1	0.63	102	1000	0.8	11.3	2000
1604	-1	0.63	102	1000	0.8	11.3	2000
1605	-1	0.63	102	1000	0.8	11.3	2000
1607	-1	0.63	96	1000	0.8	11.3	2000
1608	-1	0.34	99	100	0.8	17.0	2000
1609	-1	0.98	99	100	0.8	10.4	2000
1610	-1	2.05	100	100	0.8	9.1	2000
1611	-1	2.05	99	100	0.8	9.1	2000
1612	-1	0.63	99	1000	0.8	11.3	2000
1614	-1	0.63	99	1000	0.8	11.3	2000
1618	-1	0.63	99	1000	0.8	11.3	2000
1620	-1	0.63	99	1000	0.8	11.3	2000
1621	-1	0.63	99	1000	0.8	11.3	2000

Run	**Beam** [**GeV/c**]	**IB** [%]	**SF** [%]	**TF3** **V/cm**	**G3/G4**	$\sigma(^{55}$**Fe**) [%]	**Gain**
1622	-1	0.63	99	1000	0.8	11.3	2000
1631	-1	0.63	99	1000	0.8	11.3	2000
1632	-1	0.63	99	1000	0.8	11.3	2000
1635	-1	0.63	99	1000	0.8	11.3	2000
1636	-1	0.63	99	1000	0.8	11.3	2000
1638	-1	0.63	99	1000	0.8	11.3	2000
1639	-1	0.63	99	1000	0.8	11.3	2000
1640	-1	0.63	99	1000	0.8	11.3	2000
1641	-1	0.63	99	1000	0.8	11.3	2000
1642	-1	0.63	99	1000	0.8	11.3	2000
1645	-1	0.63	99	1000	0.8	11.3	2000
1646	-1	0.63	99	1000	0.8	11.3	2000

Bibliography

[1] **Particle Data Group** Collaboration, K. A. Olive *et al.*, "Review of Particle Physics," *Chin. Phys.* **C38** (2014) 090001.

[2] **HotQCD** Collaboration, T. Bhattacharya *et al.*, "QCD Phase Transition with Chiral Quarks and Physical Quark Masses," *Phys. Rev. Lett.* **113** (2014) 082001.

[3] P. Braun-Munzinger and J. Wambach, "The Phase Diagram of Strongly-Interacting Matter," *Rev. Mod. Phys.* **81** (2009) 1031.

[4] **ALICE** Collaboration, "The ALICE experiment at the CERN LHC," *JINST* **3** (2008) S08002. http://stacks.iop.org/1748-0221/3/i=08/a=S08002.

[5] **ALICE** Collaboration, "Performance of the ALICE experiment at the CERN LHC," *International Journal of Modern Physics A* **29** (2014) 1430044.

[6] B. Adeva *et al.*, "The construction of the L3 experiment," *NIM A* **289** (1990) 35.

[7] C. Lippmann, "Particle identification," *NIM A* **666** (2012) 148.

[8] R. Rapp, J. Wambach, and H. van Hees, "The Chiral Restoration Transition of QCD and Low Mass Dileptons," *Landolt-Bornstein* **23** (2010) 134.

[9] **ALICE** Collaboration, "ALICE: Physics Performance Report, Volume II," *Journal of Physics G: Nuclear and Particle Physics* **32** (2006) 1295. http://stacks.iop.org/0954-3899/32/i=10/a=001.

[10] **ALICE** Collaboration, "Technical Design Report of the Inner Tracking System," Tech. Rep. CERN-LHCC-1999-12, 1999. http://cds.cern.ch/record/391175.

[11] **ALICE** Collaboration, "Technical Design Report of the Time Projection Chamber," Tech. Rep. CERN-LHCC-2000-001, 2000. https://cds.cern.ch/record/451098.

[12] **ALICE** Collaboration, "Technical Design Report of the Transition Radiation Detector," Tech. Rep. CERN-LHCC-2001-021, 2001. https://cds.cern.ch/record/519145.

[13] **ALICE** Collaboration, "Technical Design Report of the Time of Flight System," Tech. Rep. CERN-LHCC-2000-012, 2000. https://cds.cern.ch/record/430132.

[14] AliRoot - ALICE Offline, Dec, 2015. http://aliweb.cern.ch/Offline/AliRoot/Manual.html.

[15] **ALICE** Collaboration, "ALICE: Physics Performance Report, Volume I," *Journal of Physics G: Nuclear and Particle Physics* **30** (2004) 1517. http://stacks.iop.org/0954-3899/30/i=11/a=001.

[16] R. Brun and F. Rademakers, "ROOT — An object oriented data analysis framework," *NIM A* **389** (1997) 81.

[17] I. Hřivnáčová *et al.*, "The Virtual MonteCarlo," in *Proc. of Computing in High Energy and Nuclear Physics*. 2003.

[18] R. Brun, F. Bruyant, M. M. A. McPherson, and P. Zanarini, "GEANT3 user's guide," Tech. Rep. CERN DD/EE/84-1, 1985.

[19] S. Agostinelli *et al.*, "Geant4 — a simulation toolkit," *NIM A* **506** (2003) 250.

[20] T. Böhlen *et al.*, "The FLUKA Code: Developments and Challenges for High Energy and Medical Applications," *Nuclear Data Sheets* **120** (2014) 211.

[21] L. Betev and P. Chochula, "Definition of the ALICE Coordinate System and basic rules for Sub-Detector Components numbering," Tech. Rep. ALICE-INT-2003-038, 2003. `https://edms.cern.ch/document/406391/2`.

[22] J. Wiechula, *Commissioning and Calibration of the ALICE-TPC*. PhD thesis, Goethe-Universität, Frankfurt am Main, 2008.

[23] **ALICE** Collaboration, "Upgrade of the ALICE Experiment: Letter of Intent," Tech. Rep. CERN-LHCC-2012-012, 2012. `http://cds.cern.ch/record/1475243`.

[24] **ALICE** Collaboration, "Upgrade of the ALICE Time Projection Chamber," Tech. Rep. CERN-LHCC-2013-020, 2013. `https://cds.cern.ch/record/1622286`.

[25] **ALICE** Collaboration, "Addendum to the Technical Design Report for the Upgrade of the ALICE Time Projection Chamber," Tech. Rep. CERN-LHCC-2015-002, 2015. `https://cds.cern.ch/record/1984329`.

[26] D. Nygren *PEP Internal Report* **198** (1975) .

[27] $\bar{\text{P}}$**ANDA** Collaboration, "Technical Progress Report for $\bar{\text{P}}$ANDA - Strong Interaction Studies with Antiprotons," tech. rep., 2005. `https://panda.gsi.de/oldwww/archive/public/panda_tpr.pdf`.

[28] G. Charpak, R. Bouclier, T. Bressani, J. Favier, and Č. Zupančič, "The use of multiwire proportional counters to select and localize charged particles," *NIM* **62** (1968) 262.

[29] L. Rolandi, W. Riegler, and W. Blum, *Particle Detection with Drift Chambers*. Springer Berlin Heidelberg, 2nd ed., 2008.

[30] W. H. Barkas, J. N. Dyer, and H. H. Heckman, "Resolution of the Σ^--Mass Anomaly," *Phys. Rev. Lett.* **11** (1963) 26.

[31] H. Bichsel, "A method to improve tracking and particle identification in TPCs and silicon detectors," *NIM A* **562** (2006) 154.

[32] W. W. M. Allison and J. H. Cobb, "Relativistic Charged Particle Identification by Energy Loss," *Annual Review of Nuclear and Particle Science* **30** (1980) 253.

[33] H. Bichsel and R. P. Saxon, "Comparison of calculational methods for straggling in thin absorbers," *Phys. Rev. A* **11** (1975) 1286.

[34] L. Landau, "On the energy loss of fast particles by ionization," *J. Phys.(USSR)* **8** (1944) 201.

[35] S. Ramo, "Currents induced by electron motion," *Proceedings of the IRE* **27** (1939) 584.

[36] A. Walenta, J. Fischer, H. Okuno, and C. Wang, "Measurement of the ionization loss in the region of relativistic rise for noble and molecular gases," *NIM* **161** (1979) 45.

[37] E. Nappi, "Advances in charged particle identification techniques," *NIM A* **628** (2011) 1. Vienna Conference on Instrumentation 2010.

[38] J. Alme *et al.*, "The ALICE TPC, a large 3-dimensional tracking device with fast readout for ultra-high multiplicity events," *NIM A* **622** (2010) 316.

[39] J. Alme *et al.*, "RCU2 — The ALICE TPC readout electronics consolidation for RUN2," *JINST* **8** (2013) C12032. `http://stacks.iop.org/1748-0221/8/i=12/a=C12032`.

[40] A. Breskin, G. Charpak, F. Sauli, M. Atkinson, and G. Schultz, "Recent observations and measurements with high-accuracy drift chambers," *NIM* **124** (1975) 189.

[41] A. Oed, "Position-sensitive detector with microstrip anode for electron multiplication with gases," *NIM A* **263** (1988) 351.

[42] Y. Bagaturia *et al.*, "Studies of aging and HV break down problems during development and operation of MSGC and GEM detectors for the inner tracking system of HERA-B," *NIM A* **490** (2002) 223.

[43] F. Sauli and A. Sharma, "Micropattern gaseous detectors," *Annual Review of Nuclear and Particle Science* **49** (1999) 341.

[44] F. Sauli, "GEM: A new concept for electron amplification in gas detectors," *NIM A* **386** (1997) 531.

[45] Y. Giomataris, P. Rebourgeard, J. Robert, and G. Charpak, "MICROMEGAS: a high-granularity position-sensitive gaseous detector for high particle-flux environments," *NIM A* **376** (1996) 29.

[46] C. Altunbas *et al.*, "Construction, test and commissioning of the triple-GEM tracking detector for COMPASS," *NIM A* **490** (2002) 177.

[47] G. Bencivenni *et al.*, "A triple GEM detector with pad readout for high rate charged particle triggering," *NIM A* **488** (2002) 493.

[48] Z. Fraenkel *et al.*, "A hadron blind detector for the PHENIX experiment at RHIC," *NIM A* **546** (2005) 466.

[49] M. Bagliesi *et al.*, "The TOTEM T2 telescope based on triple-GEM chambers," *NIM A* **617** (2010) 134. 11th Pisa Meeting on Advanced Detectors.

[50] D. Abbaneo *et al.*, "The status of the GEM project for CMS high-η muon system," *NIM A* **732** (2013) 203. Vienna Conference on Instrumentation 2013.

[51] S. Bachmann *et al.*, "Discharge studies and prevention in the gas electron multiplier (GEM)," *NIM A* **479** (2002) 294.

[52] F. Böhmer *et al.*, "Simulation of space-charge effects in an ungated GEM-based TPC," *NIM A* **719** (2013) 101.

[53] R. Veenhof, *Garfield - a drift chamber simulation program.* CERN Programm Library, 1998.

[54] H. Raether, *Electron avalanches and breakdown in gases.* Butterworths, 1964.

[55] A. Bressan, J. Labbé, P. Pagano, L. Ropelewski, and F. Sauli, "Beam tests of the gas electron multiplier," *NIM A* **425** (1999) 262.

[56] L. Fabbietti *et al.*, "The P̄ANDA GEM-based TPC prototype," *NIM A* **628** (2011) 204. Vienna Conference on Instrumentation 2010.

[57] M. Berger, *Development, Commissioning and Spatial Resolution Studies of a new GEM based TPC*. PhD thesis, Technische Universität München, 2015.

[58] F. Böhmer *et al.*, "First measurement of $\mathrm{d}E/\mathrm{d}x$ with a GEM-based TPC," *NIM A* **737** (2014) 214.

[59] M. Villa *et al.*, "Progress on large area GEMs," *NIM A* **628** (2011) 182. Vienna Conference on Instrumentation 2010.

[60] T. Hildén *et al.*, "Optical quality assurance of GEM foils," *NIM A* **770** (2015) 113.

[61] Huntsman Advanced Materials (Schweiz) GmbH, Klybeckstrasse 200, 4057 Basel, Switzerland. `http://www.huntsman.com/advanced_materials`.

[62] A. Deisting, "Private communication.".

[63] F. Paschen, "Über die zum Funkenübergang in Luft, Wasserstoff und Kohlensäure bei verschiedenen Drücken erforderliche Potentialdifferenz," *Annalen der Physik* **273** (1889) 69.

[64] D. Simon *et al.*, "Secondary beams for tests in the PS East experimental area," Tech. Rep. CERN PS-PA-EP-Note-88-26, 1988. `http://cds.cern.ch/record/1665434`.

[65] P. Gasik, "Development of GEM-based Read-Out Chambers for the upgrade of the ALICE TPC," *JINST* **9** (2014) C04035. `http://stacks.iop.org/1748-0221/9/i=04/a=C04035`.

[66] A. Kaukher, O. Schäfer, H. Schröder, and R. Wurth, "Status of TPC-electronics with Time-to-Digit Converters," Tech. Rep. EUDET-Memo-2009-08, 2009.

[67] R. Bosch, A. de Parga, B. Mota, and L. Musa, "The ALTRO chip: a 16-channel A/D converter and digital processor for gas detectors," *IEEE Transactions on Nuclear Science* **50** (2003) 2460.

[68] M. I. I. Belikov and K. Šafařík Tech. Rep. ALICE-INT-2005-036, 2005.

[69] P. Billoir, "Track fitting with multiple scattering: A new method," *NIM* **225** (1984) 352.

[70] R. Frühwirth, "Application of Kalman filtering to track and vertex fitting," *NIM A* **262** (1987) 444.

[71] M. Ivanov, I. Belikov, P. Hristov, and K. Šafařík, "Track reconstruction in high density environment," *NIM A* **566** (2006) 70. 1st Workshop on Tracking in High Multiplicity Environments 2005.

[72] D. Antończyk *et al.*, "Performance studies with an ALICE TPC prototype," *NIM A* **565** (2006) 551.

Acknowledgements

The last year has been a fantastic adventure and I am deeply grateful to everyone involved.

First of all, I would like to express my gratitude to Prof. Laura Fabbietti for giving me this incredible opportunity, for her confidence and her continuous support in many fields. I am deeply indebted to my supervisor Dr. Piotr Gasik, for his fantastic advise, for many excellent ideas and fruitful discussions. I want to thank him for all his commitment, encouragement and constant support. The brilliant input from Dr. Jens Wiechula has been invaluable to me and especially without his vast knowledge about AliRoot, I still would be lost somewhere in the code.

The time with my office mates Dr. Martin Berger and Dr. Robert Münzer has been a true pleasure and I am grateful for all the inspiration, encouragement and intelligent advice. In particular, I would like to thank Martin for all his help and for proofreading parts of this thesis. Many thanks also to all members of the group for the fantastic atmosphere and all the rest, it is a pleasure to work together with you!

I would like to thank everyone involved in the testbeam, especially Dr. Chilo Garabatos and Alexander Deisting for the excellent organization, as it has been a true pleasure taking part in it. A lot of thanks to Dr. Peter Christiansen and Prof. Harald Appelshäuser for their helpful input to this work. It is a true pleasure to work for the ALICE TPC collaboration and I'm very much looking forward what's to come!

Special recognition goes out to my parents, for all their constant support, advice and belief.

But above all, I want to thank my wonderful fiancée Steffi for her incredible support in uncountable ways, her patience and her love.